MASTER'S THESIS

Improving Data Assimilation for MJO Prediction based on Experiments with the Skeleton Model for Tropical Intraseasonal Variability

Meteorological Institute
Faculty of Physics
Ludwig-Maximilians-Universität München

SUBMITTED BY
Tabea Gleiter
Munich, 27 January 2021

SUPERVISOR: PD DR. TIJANA JANJIĆ PFANDER
COURSE OF STUDIES: M.SC. PHYSICS

MASTERARBEIT

Verbesserung der Datenassimilation für MJO Vorhersagen auf Basis von Experimenten mit dem Skeleton-Modell für tropische intrasaisonale Variabilität

Meteorologisches Institut
Fakultät für Physik
Ludwig-Maximilians-Universität München

VORGELEGT VON
Tabea Gleiter
München, 27. Januar 2021

BETREUERIN: PD DR. TIJANA JANJIĆ PFANDER
STUDIENGANG: M.SC. PHYSIK

Abstract

The Madden-Julian Oscillation (MJO) is the most pronounced component of atmospheric variability on intraseasonal timescales in the tropics and strongly interconnected with other weather and climate phenomena, even in the extratropics. Its predictability is thus a key issue for modern numerical weather prediction. However, the accuracy of MJO forecasts is still deficient, not only due to model imperfections caused by an incomplete understanding of the underlying multi-scale physical mechanisms, but also due to suboptimal Data Assimilation (DA) systems. The latter problem is addressed in this thesis, in which possible improvements in DA for MJO prediction are investigated.

Since running a full-blown general circulation model on the intraseasonal timescale is computationally very expensive, the approach taken in this work are simplified experiments in a toy model setting. For this, the 'Skeleton Model for Tropical Intraseasonal Variability' was used in its meridionally and vertically highly truncated nonlinear deterministic version as in Majda and Stechmann (2011). This model is based on the consideration of the MJO as neutrally stable oscillation at planetary scale, that is evoked by convective instabilities at sub-planetary scale. It couples a nonlinear oscillator relationship between moisture and the planetary scale envelope of synoptic scale convective activity to the well-known Matsuno-Gill model for tropical large scale dynamics. With these simple equations, which are solvable at small computational cost, the Skeleton model was shown to capture the main observed large scale characteristics of the MJO, including its typical phase speed, dispersion relation, and wind structure. As an efficient toy model for the MJO it is thus particularly suitable for the purpose of this work.

The investigation of possible DA improvements is done with identical twin experiments and based on a stochastic Ensemble Kalman Filter (EnKF). With this approach, any imperfections in the system with respect to perfect sequential Bayesian filtering are reduced to unavoidable sampling errors and the EnKF's neglect of non-Gaussian moments in the ensemble's distribution. Due to the nonlinearity in the Skeleton model, the latter can however be strong, especially in the strictly positive variable of convective activity. While a variety of techniques exists to address non-Gaussianity in an EnKF, this thesis focuses on the EnKF's extension by analysis constraints, then called Quadratic Programming Ensemble (QPEns), as recently suggested by Janjić et al. (2014). The QPEns appears specifically promising in this work's setup as the Skeleton model's underlying physical equations incorporate two energy conservation principles. Besides a detailed investigation of the EnKF with special regard to localization and the effects of observing different variables, this thesis shows how in particular the constraint of the analysis ensemble members to the truth's total energy improves the filter's result and can mitigate negative effects of neglected or only rudimentarily treated non-Gaussianity. Special attention is thereby paid to the filtering skill for the tropical wave types that are present in the Skeleton model, most importantly amongst them the MJO.

Contents

1 Introduction

The forecast skill that is achieved by present-day operational numerical weather prediction (NWP) systems is largely limited by model errors and uncertainties in the initial and boundary conditions. Those inhibit it from reaching its intrinsic limit as given by the weather regime dependent chaotic growth of infinitesimal atmospheric disturbances. Much of the research effort in the atmospheric sciences is therefore put into model improvements, better observational networks, and advances in Data Assimilation (DA) algorithms. However, the amount of discrepancy between the practical and theoretical predictability is subject to regional variations and particularly high in low latitudes. Some main causes for this are persistent model errors due to the complicated multiscale interactions between convectively coupled waves, a sparser network of weather stations caused by a smaller land coverage together with a higher percentage of developing countries, specific difficulties with satellite measurements, and moreover suboptimal DA systems that are often tailored for the dominance of geostrophic balance in the extratropics. Yet, as a consequence of the multiple interdependencies in the continuous atmosphere, any progress in tropical forecasting has the potential to yield benefits for a wider than only the equatorial area. It is for these reasons that the improvement of tropical weather prediction constitutes a particularly crucial issue. [Žagar et al., 2016; Bechtold, 2019; Laing and Evans, 2011, Chapter 9]

Amongst the many efforts that deal with the above challenges is the project B6 of the Transregional Collaborative Research Center "Waves to Weather" (2nd phase of W2W, SFB/TRR165, 2019-2023), in which "new data assimilation approaches to better predict tropical convection" are developed. This project is aimed at reducing errors in the initial conditions for NWP in the tropics, and especially those connected to tropical waves and convection as they can easily amplify during the subsequent forecast. The main approach chosen to reach this objective are ensemble DA experiments based on tropical aquaplanet channel simulations with the full-blown, i.e. highly resolved, ICOsahedral Non-hydrostatic (ICON) model of the German Weather Service (DWD). However, due to their high computational demand, such experiments are only possible on time scales up to approximately 40 days. Consequently, the development of DA techniques that are beneficial for the prediction of circulations on intraseasonal to seasonal timescales can not be covered by them. Of special concern in this regard is the Madden-Julian Oscillation (MJO) as it is the most pronounced component of intraseasonal variablity in the tropics. The MJO furthermore has large impacts on many other tropical weather and climate phenomena, such as monsoon and El Niño-Southern Oscillation (ENSO) development, and even interacts with the extratropics (Khouider et al., 2013). In fact, its deficient representation in tropical forecasts is already for some time known to be a key component for the lack of predictability on subseasonal time scales, not only in the equatorial area (Vitart and Molteni, 2010). Although a prominent obstacle is its still incomplete physical understanding and thus poor representation in general circulation models (GCMs), the MJO's large scale structure is nowadays well known. Progress can therefore also be expected from more suitable DA algorithms to reduce the initial uncertainty in those (Chen and Majda, 2016).

This is where this work comes in. Embedded in the above mentioned "Waves to Weather" project as a supplement to the high-resolution experiments, it aims to improve DA for MJO prediction. Therefore, simplified studies were conducted with a computationally inexpensive toy model, that is designed to reproduce in particular the large scale structure of the MJO but contains no sophisticated orography or extratropical influences. This model is the so called 'Skeleton Model for Tropical Intraseasonal Variability', which was first published by Majda and Stechmann (2009) in its simplest, meridionally and vertically truncated linearized form. The strikingly good accordance of the eigenmodes in this original version with the main large scale characteristics of some tropical wave types have made the

Skeleton model well known. Especially the MJO is well represented with its typical phase speed, dispersion relation, and wind structure. Therefore, the model has since been published in various extended and modified forms; see e.g. Majda and Stechmann (2011) for the nonlinear version, Thual et al. (2014) for its corresponding stochastic version, or Thual et al. (2015) and Thual and Majda (2016b) for extensions in its meridional and vertical structure, respectively. As a trade-off between complexity and accuracy, and in order to avoid model error, the focus in this work is put on the fully truncated nonlinear deterministic version as in Majda and Stechmann (2011). The MJO is therein captured with greater realism than in the original linearized model, but the model is still easy to handle due to the strong truncation. This model version can be regarded as an extension of the well-known Matsuno-Gill model for tropical large scale dynamics, to which it couples additional equations for moisture and the planetary scale envelope of synoptic scale convective activity. Those are themselves interrelated by a nonlinear oscillator relationship as the MJO is assumed to be a neutrally stable wave at planetary scale, driven by convective instabilities at sub-planetary scale.

In this work, identical twin experiments with the Skeleton model were used to locate possible improvements in DA for MJO prediction. Whereas similar research on the construction of a nonlinear filter for the Skeleton model has already been successfully conducted by Chen and Majda (2016), this thesis is confined to stochastic Ensemble Kalman Filter (EnKF) based techniques. The probability estimation for the atmospheric state is thus represented by a finite ensemble, which is updated stochastically such that the Kalman filter equations are statistically reproduced. With this setup, any error sources in the system with respect to perfect sequential Bayesian filtering are confined to unavoidable sampling errors and potential non-Gaussian moments in the ensemble's distribution, that are neglected in the EnKF. The latter is specifically crucial in the Skeleton model since the convective activity is confined to positive values and its probability distribution can be significantly skewed depending on the model's background settings. Besides a thorough investigation of beneficial localization and observations in the EnKF, this thesis is therefore in particular aimed at the mitigation of filter imperfections due to non-Gaussianity. The assessment of the general filter quality was thereby in all experiments complemented by a special focus on the predictability of the Skeleton model's tropical wave types, especially the MJO.

Diverse methods are researched to improve the probability estimation in EnKFs in the presence of non-Gaussianity. Amongst them are constraints of the analysis ensemble members to physically motivated, known or estimated properties. This transforms the update step into a numerical optimization problem and was therefore called Quadratic Programming Ensemble (QPEns) when first proposed for linear and boundary constraints by Janjić et al. (2014). The QPEns has since shown great potential for improvements with respect to an EnKF under non-Gaussian conditions and has already been successfully applied in other toy model studies (see Janjić et al., 2014; Zeng et al., 2017; Ruckstuhl and Janjić, 2018). Hence, constraints of physical quantities to the synthetic truth's value were also pursued as approach to mitigate non-Gaussianity effects in this work. This was especially motivated by two energy conservation properties, i.e. moist static and total energy, that are incorporated in the Skeleton model's underlying equations. In particular, constraining the nonlinear total energy appeared promising as it includes an automatic positivity constraint for convective activity. The effect of constraining these two model balances was thus investigated, and compared to a dry mass constraint and a simple positivity constraint for convective activity.

This thesis is further structured as follows: In Chapter 2, the theoretical background for this work is presented, which is subdivided into three separate subsections: General information on important aspects of tropical meteorology with respect to convectively coupled waves and the MJO is given in 2.1, the Skeleton model version that is used in this work is described in detail in 2.2, and relevant foundations of DA, especially the stochastic EnKF and the QPEns, are explained in 2.3. Thereafter,

in Chapter 3, the methods that were used to produce this work's results are introduced. First, the general setup of the identical twin experiments is explained in 3.1, and subsequently, the details of the DA algorithms' implementations are described in 3.2, and the diagnostics that were used for their assessment in 3.3. The results of this thesis are finally presented in Chapter 4 in three parts. Some preparatory information on climatological properties of the Skeleton model that are important for the setup and interpretation of the DA results is given in 4.1. Based on this, 4.2 contains the results for the optimal localization and the investigation of different observational setups in the EnKF, and 4.3 presents the impacts of the analysis constraints. All results are put into context, interpreted, and thereafter discussed with respect to their accordance with earlier work, further options for their verification, and their importance and applicability for NWP in Chapter 5. Lastly, a summary and outlook for possible future work is given in Chapter 6. All variables, constants and functions that are used throughout the text without repeated explanation are listed in Appendix A, sorted by the chapters of their first appearance. Furthermore, an alphabetical list of all introduced abbreviations can be found in Appendix B.

2 Theoretical background

2.1 Tropical meteorology

In this chapter, some general information on tropical meteorology that is important to understand the MJO and the Skeleton model is introduced. After the presentation of the most important aspects of the climatological mean circulation in 2.1.1, the Matsuno-Gill theory of equatorial waves is explained in 2.1.2, and the main features of observed convectively coupled waves and the MJO are described in 2.1.3.

2.1.1 Climatological background circulation

The atmosphere is a continuous system without clearly definable distinct regions such as the tropics. Nevertheless, some general characteristics of the mean atmospheric circulation and forcing in the area adjacent to the equator can be named that are substantially different from higher latitudes of the Earth. Detailed descriptions of the topical climatology, of which a summary is given in the following, can be found in many standard textbooks and lecture scripts on tropical meteorology or general atmospheric dynamics, e.g. by Smith (2015) in Chapter 1, by Laing and Evans (2011) in Chapters 1 and 3 or by Holton and Hakim (2013) in Chapter 11.

Due to the solar radiative excess in the tropics and the respective deficit in the extratropics, the mean energy transport on Earth is directed polewards. Though complemented by oceanic currents, this is in large parts brought about by atmospheric motions. Since the sun's radiation is primarily absorbed by oceans and continental areas, the surplus heating of the tropical air masses happens indirectly via mainly latent, but also sensible heat release from the surface, such that the tropical atmosphere is even characterized by net radiative cooling. The intertropical convergence zone (ITCZ), a longitudinal band of deep convection and high precipitation rates, that comes along with a large vertical extend of the troposphere and low surface pressures, is thus an important component of the tropical mean meridional circulation, the Hadley cell. Besides the ITCZ, the Hadley cell is furthermore composed of poleward motion of air with surplus moist static energy in the upper troposphere, subsidence with high surface pressures in the subtropics, and trade winds in the lower troposphere. The latter transport moisture that has been acquired from the oceans equatorwards. Since these trade winds are deflected westwards, i.e. become easterlies, due to the momentum balance at decreasing Coriolis force, they have moreover a large impact on the mean motion in zonal direction. They effectuate an increased sea surface temperature and thus enhance latent heating in the western in contrast to the eastern Pacific area. Analogous to the Hadley cell, this constitutes a zonal circulation cell with vertical extend over the Pacific, the Walker cell, which is the most prominent component of the tropical atmospheric mean flow in east-west extend, and also coupled to ocean currents. Both, the Hadley and the Walker circulation, are subject to slight seasonal variations. Additionally, there are smaller zonal circulations in the climatological as well as the seasonal means. Those are mostly driven by zonal pressure gradients due to differential diabatic heating over sea and land areas, such as e.g. monsoon events. In conclusion, in this simplified treatment, the tropics are in contrast to the midlatitudes particularly shaped by excess solar radiation with smaller seasonal variation, enhanced latent heating due to the large ocean coverage, and the vanishing Coriolis force, which in combination effectuate a characteristic large scale mean circulation.

On top of this mean circulation, there are several types of instabilities, i.e. waves and vortices, that can occur in the tropical atmosphere. Many of them are also clearly distinct from those typical for higher latitudes. For subseasonal to seasonal and synoptic to planetary temporal and spatial extends,

they are especially characterized by a weak geostrophic balance, a strong coupling to convection, and interactions across multiple scales. Some prominent examples that can be named are e.g. tropical cyclones, equatorial waves, the MJO, and ENSO.

2.1.2 Matsuno-Gill theory of tropical waves

The most basic disturbances of the mean circulation in the tropics, which lay the foundation for many weather and climate phenomena in low latitudes, are equatorial waves. These are periodic large scale fluctuations in pressure, temperature, and wind that propagate zonally and vertically and are confined to the equatorial area. Often evoked by regional weather events, such as e.g. deep convection, they can extend over long spatial scales or span the whole equator, and comprise and organize smaller scale convective elements along them (Kiladis et al., 2009). Therefore, they can spread local energy to wider regions (Wheeler and Nguyen, 2014).

A consistent theory of free dry dynamical oscillations in the equatorial atmosphere was first derived by Matsuno (1966). Its results are a number of theoretical wave types, whose dispersion relations are in very good agreement with observations (Wheeler and Kiladis, 1999). Following Matsuno (1966), the derivation of the equatorial wave types starts from the common atmospheric Navier-Stokes equations, which describe atmospheric dynamics as the motion of a stably stratified fluid on the rotating Earth's sphere. Hereafter, their variables are indicated by x, y and z for the zonal, meridional and vertical position, u and v for the respective horizontal winds, t for the time, and p for the pressure. ρ stands for the density, which can be decomposed into a constant mean, a purely height dependent, and a perturbation component as $\rho = \rho_0 + \overline{\rho}(z) + \rho'(x, y, z)$. In a first step, the following simplifications are applied to the equations:

- neglect of centrifugal force
- neglect of friction/viscosity and diabatic heating or other dynamical forcing
- linearization around an assumed resting background state, i.e. all variables are perturbations, thus neglect of advection; a non-zero background wind would simply Doppler-shift the resulting wave-frequencies
- β-plane approximation for the Coriolis force due to the proximity to the equator: assumption of an approximately constant meridional derivative β of the Coriolis parameter
- hydrostatic and Boussinesq approximations: assumption of a balance between the gravitational acceleration g and the vertical pressure gradient, and neglect of density variations if not in combination with gravity.

Furthermore, the horizontal and vertical dynamics are decoupled by the definition of vertical modes $\frac{\partial}{\partial z}\left(\frac{1}{g\frac{\partial \overline{p}}{\partial z}}\frac{\partial p}{\partial z}\right) =: \frac{1}{gH^*}\frac{p}{\rho_0}$ (2.1) with scale heights H^*. This yields the single-layer equatorial shallow water equations for the horizontal motion of each vertical mode, where H^* is in this context called equivalent depth as it replaces the mean fluid depth:

$$\begin{aligned} \frac{\partial u}{\partial t} - \beta y v &= -\frac{1}{\rho_0}\frac{\partial p}{\partial x} \\ \frac{\partial v}{\partial t} + \beta y u &= -\frac{1}{\rho_0}\frac{\partial p}{\partial y} \\ \frac{1}{\rho_0}\frac{\partial p}{\partial t} &= -gH^*\left(\frac{\partial u}{\partial x} + \frac{\partial v}{\partial y}\right). \end{aligned} \tag{2.2}$$

Next, a plane wave ansatz $u,v,p \propto e^{i(kx-\omega t)}$ (2.3) and an equatorial trapping boundary condition $\lim_{y\to\pm\infty} u,v,p = 0$ (2.4) are introduced. Solutions for the amplitudes of u, v, and p and corresponding

frequencies ω can then be calculated for any arbitrary zonal wavenumber k and equivalent depth. As a whole, they form an orthogonal basis for any distributions of u, v, and p with the given k and H^* that respect the boundary condition. Moreover, the vertical modes also form an orthogonal complete set for reasonable boundary conditions. Any tropical waves can thus be described as superpositions of the horizontal wave solutions for varying equivalent heights.

The horizontal plane wave solutions for a given H^* are typically categorized by their zonal dispersion relations and meridional structures into the following distinct types. Here, all variables have been nondimensionalized by the dimensions for horizontal lengths $[L] = \sqrt{\frac{\sqrt{gH^*}}{\beta}}$ and time $[T] = \frac{1}{gH^*\sqrt{\beta}}$ (2.5), Φ_m indicate the parabolic cylinder functions (PCFs) and m consequently the waves' meridional mode numbers.

wave type	approximate zonal dispersion relation	structure: $\begin{pmatrix} u \\ v \\ \frac{p}{\rho_0} \end{pmatrix} \propto e^{i(kx-\omega t)}$.
quasi geostrophic Rossby/equatorial Rossby (ER)	$\omega = \frac{-k}{k^2+2m+1} \,\forall\, m \in \mathbb{N}$	$\begin{pmatrix} i(\omega^2-k^2)\Phi_m(y) \\ m(k-\omega)\Phi_{m-1}(y) - \frac{1}{2}(\omega+k)\Phi_{m+1}(y) \\ -m(k-\omega)\Phi_{m-1}(y) - \frac{1}{2}(\omega+k)\Phi_{m+1}(y) \end{pmatrix}$
eastward and westward moving inertio-gravity (EIG,WIG)	$\omega = \pm\sqrt{k^2+2m+1} \,\forall\, m \in \mathbb{N}$	$\begin{pmatrix} i(\omega^2-k^2)\Phi_m(y) \\ m(k-\omega)\Phi_{m-1}(y) - \frac{1}{2}(\omega+k)\Phi_{m+1}(y) \\ -m(k-\omega)\Phi_{m-1}(y) - \frac{1}{2}(\omega+k)\Phi_{m+1}(y) \end{pmatrix}$
another eastward moving inertio-gravity (EIG)	$\omega = \frac{k}{2} + \sqrt{\left(\frac{k}{2}\right)^2 + 1}$, indicated with $m = 0$	$\begin{pmatrix} 2i(k-\omega)\Phi_0(y) \\ \Phi_1(y) \\ \Phi_1(y) \end{pmatrix}$
mixed Rossby-gravity (MRG)/Yanai	$\omega = \frac{k}{2} - \sqrt{\left(\frac{k}{2}\right)^2 + 1}$, indicated with $m = 0$	$\begin{pmatrix} 2i(k-\omega)\Phi_0(y) \\ \Phi_1(y) \\ \Phi_1(y) \end{pmatrix}$
Kelvin (similarity with coastal Kelvin waves)	$\omega = -k$, indicated with $m = -1$	$\begin{pmatrix} 0 \\ \Phi_0(y) \\ \Phi_0(y) \end{pmatrix}$

The classification of the first three wave types as Rossby or gravity waves is evident due to the rather geostrophic and ageostrophic features, respectively, although the quasi geostrophic Rossby waves show some particularities compared to those in mid-latitudes. However, there are two additional wave types, the mixed Rossby-gravity (MRG) and Kelvin waves, which show uncommon mixed geostrophic and ageostrophic properties with a decreasing predominance of the Rossby wave characteristics with increasing zonal wavenumber. There is thus – in contrast to the mid-latitudes – no clear scale separation between Rossby and gravity waves. The vertical propagation of the equatorial waves is given by the structure defined in the vertical modes.

The above theory derives fundamental free dry dynamical wave types that form basis functions for any equatorially confined zonally periodic perturbations. Based on this, Gill (1980) calculated the steady state response of the tropical atmosphere to different diabatic heating distributions. He therefore added some further assumptions to the equatorial shallow water equations, namely:

- a longwave approximation $\frac{\partial v}{\partial t} = 0$ (2.6), such that the zonal flow is in geostrophic balance with

the meridional pressure gradient; this is assumed for long zonal and temporal scales and dampens gravity and MRG waves with small amplitudes (Majda, 2003, Chapter 9)
- a constant forcing/diabatic heating term Q to the right hand side of the pressure equation
- friction in all variables by replacing $\frac{\partial}{\partial t} \rightarrow \frac{\partial}{\partial t} + \epsilon$ (2.7) with $\epsilon \geq 0$.

This reduced model was successful in deriving some of the basic characteristics of the Hadley and the Walker cell as responses to simple diabatic heating structures. It has thereupon become well known as Matsuno-Gill model and is still frequently used as a starting point to study tropical flows caused by diabatic heating, i.e. mostly convection.

2.1.3 Convectively coupled equatorial waves and MJO

The Matsuno theory of free dry dynamic equatorially trapped waves has gained recognition when Wheeler and Kiladis (1999) published an article in which they analyzed the zonal wavenumber-frequency spectrum of 18 years of outgoing longwave radiation (OLR) satellite records in the tropics. Since OLR can be regarded as a representative measure for cloudiness, the dispersion relations in the retrieved statistically significant spectral peaks reflect motions related to deep convection. Interestingly, except for smaller than expected equivalent heights, many of them still show a good agreement with the theoretical curves (cf. Figure 2.1). This finding thus implied a strong interaction between convection and dry dynamics, expressed in so called convectively coupled equatorial waves (CCEWs). Nowadays, it is known that they approximately share the dispersion relations and horizontal structures of the Matsuno wave types but exhibit more complicated vertical structures, which are also responsible for the differing equivalent heights (Kiladis et al., 2009).

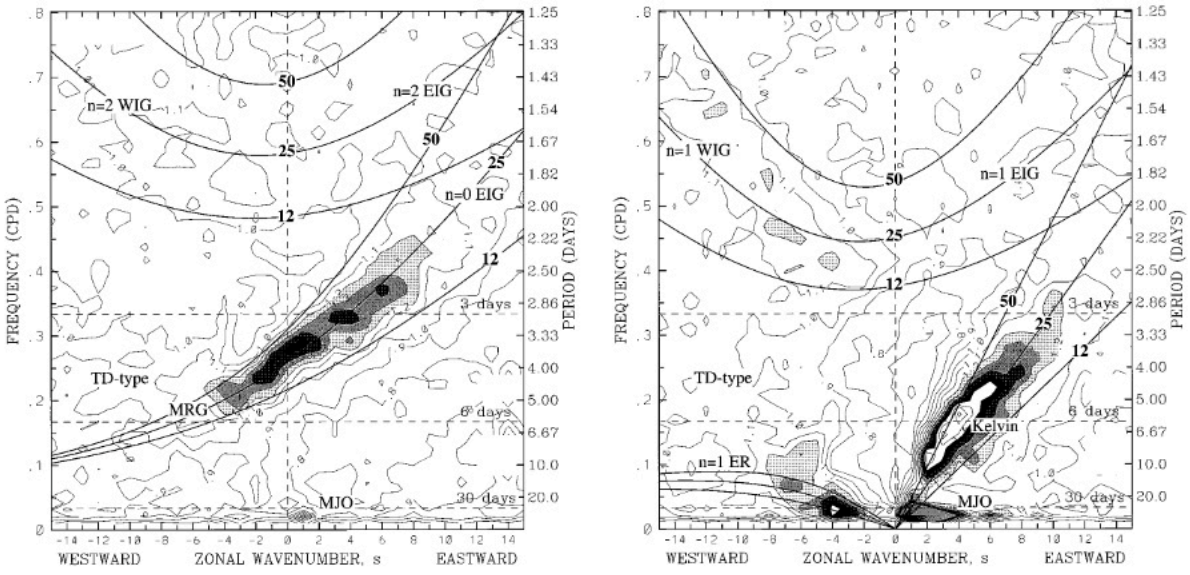

Figure 2.1: Statistically significant peaks in the zonal wavenumber-frequency spectrum of 18 years of twice daily satellite records of tropical OLR data, decomposed in antisymmetric (left) and symmetric (right) components about the equator, superimposed theoretical dispersion curves of free dry dynamic tropical waves for different indicated equivalent heights and meridional modes (in this figure indicated with n instead of m); from Wheeler and Kiladis (1999).

As apparent in the Wheeler-Kiladis diagram, CCEWs make up a large portion of the tropical variance on large scales. However, there is one additional significant spectral peak in the equatorially symmetric components that can not be classified as such. The flat dispersion relation in the intraseasonal time range and at planetary zonal scales is clearly associated with a perturbation that was first detected

by Madden and Julian (1971) and is therefore called Madden-Julian Oscillation (MJO). The MJO attracts much research interest (Zhang et al., 2013) as it is the main component of tropical intraseasonal variability, and moreover connected to extratropical intraseasonal variability and largely influencing a multitude of tropical phenomena, ranging from tropical cyclones and monsoon to ENSO (Khouider et al., 2013). By now, these interdependencies are known to be due to the fact that the MJO is the planetary scale envelope of multiple CCEWs, mostly convectively coupled ER waves of small meridional mode and Kelvin waves (Castanheira and Marques, 2020), which are themselves envelopes of multiple mesoscale convective systems. This reveals the organized nature of tropical convection across many scales, whose details are however complex and still not fully understood (Khouider et al., 2013). Nevertheless, looking primarily at the large scale, the MJO can be described by the following most important observed characteristics (Zhang, 2005):

- a deep convective center with inactive phases to the east and west, moving eastward at a phase speed of approximately 5 $\frac{\mathrm{m}}{\mathrm{s}}$ and showing a characteristic dispersion relation with constant intraseasonal oscillation periods of $30 - 90$ days for a range of small zonal wavenumbers
- a horizontal structure with positive humidity anomalies to the east of the convective center and a quadrupole wind circulation around the convective center
- a geographical confinement to warm ocean surfaces, beginning as standing wave in the Indian ocean and propagating across the western Pacific (Majda and Stechmann, 2011)
- an interannual variability with intermittent generation of MJO events, that are often organized into wavetrains (Thual et al., 2014)
- a seasonal cycle in latitudinal location and strength
- a complex westward tilted vertical structure with overturning zonal circulation
- a variability in the characteristics between individual MJO events (Majda et al., 2019).

The more large scale features of the MJO (cf. Figure 2.2) are commonly referred to as the MJO skeleton, as opposed to the MJO muscle which signifies details of the more refined structure within the MJO envelope, such as e.g. westerly wind bursts or complex convective features (Majda et al., 2019).

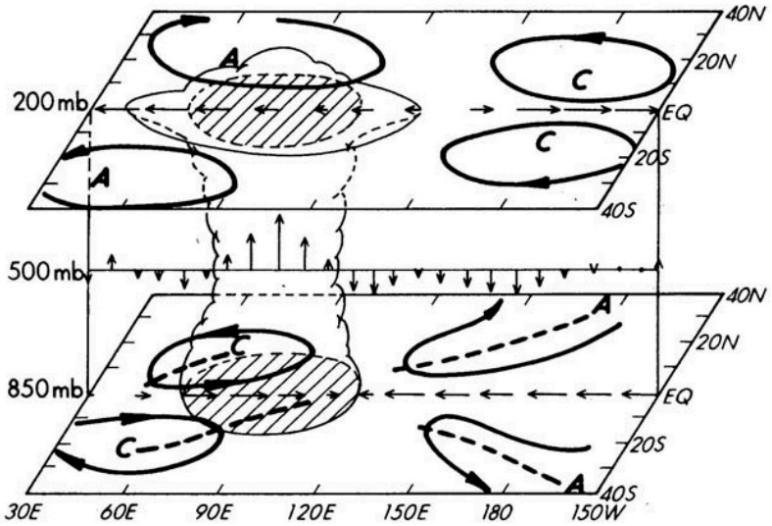

Figure 2.2: MJO skeleton (large scale) structure with a deep convective center and quadrupole wind circulation, C and A mark cyclonic and anticyclonic centers and dashed lines indicate troughs and ridges; from Zhang (2005).

Although the MJO skeleton is well known, its underlying multiscale dynamical composition is still subject to a lack of understanding, as mentioned previously, and the interactions are moreover com-

plicated to simulate. Present-day GCMs therefore still struggle with good representations of both, the skeleton and the muscle of the MJO (Stachnik et al., 2015). Since convection parameterization naturally appears to be the most critical issue in this regard, recent progress was especially expected from new and more sophisticated approaches in this field (Kim et al., 2009). Indeed, success could be achieved e.g. with multiscale models, such as the multicloud model by Boualem Khuider and Andrew Majda (Khouider and Majda, 2006, 2007), and superparameterizations (Stachnik et al., 2015). However, an interesting innovation is also the 'Skeleton Model for Tropical Intraseasonal Variability', which for the first time captures most of the large scale MJO characteristics in a computationally inexpensive toy model with an actually very simple convection parameterization (Stachnik et al., 2015).

2.2 The Skeleton model

In the following, the 'Skeleton model for Tropical Intraseasonal Variability' is presented. Starting from its underlying physical motivation and equations in 2.2.1, the algorithm of the vertically and meridionally fully truncated nonlinear deterministic model version is derived in 2.2.2. Thereafter, the eigenmodes of the linearized model version are described in 2.2.3 as they are useful to understand the expression of different tropical wave types, amongst them the MJO, in the model. The properties of the model version that is used in this work, and especially its energy balances, are introduced in 2.2.4. Lastly, in 2.2.5, the setup of an MJO index that measures the strength of the MJO based on the linearized Skeleton model's eigenmodes is explained.

2.2.1 Physical motivation

The Skeleton model is a simple and computationally inexpensive toy model for tropical atmospheric motions on intraseasonal and planetary scales, i.e. mainly the MJO. It extends the well-known Matsuno-Gill model, which is considered without dissipation at large scales except for a constant radiative cooling. Instead, the diabatic heating is coupled to an additional equation for the envelope of synoptic scale convective activity (a), which is itself connected to planetary scale lower tropospheric moisture anomalies (q) through a nonlinear oscillator relationship. This yields the following physical equations for the model's nonlinear, deterministic form, that was introduced in Majda and Stechmann (2011) and used in this work:

$$\begin{aligned}
\frac{\partial u}{\partial t} - yv - \frac{\partial \theta}{\partial x} &= 0 \\
yu - \frac{\partial \theta}{\partial y} &= 0 \\
\frac{\partial \theta}{\partial t} - \left(\frac{\partial u}{\partial x} - \frac{\partial v}{\partial y} \right) &= \overline{H} a - s^{\theta} \\
\frac{\partial q}{\partial t} + \overline{Q} \left(\frac{\partial u}{\partial x} + \frac{\partial v}{\partial y} \right) &= -\overline{H} a + s^{q} \\
\frac{\partial a}{\partial t} &= \Gamma q a.
\end{aligned} \tag{2.8}$$

All meanings and dimensions of the variables in the above equations, together with the essential physical constants, are explained in Tables 2.1 and 2.2. The underlying assumption of the Skeleton model is thus that the MJO is a neutrally stable wave at planetary scale, which is driven by convective instabilities at sub-planetary scale. The latter are condensed in their planetary scale envelope, whose evolution is described by the simple parameterization in the last equation. This was derived from a combination of observations, modelling, and theory. Since the growth rate Γ represents a strong approximation of any sub-planetary scale processes, whose details are neglected, the model's results are only meaningful at large scales (approx. $|k| \leq \frac{5}{40000\,\mathrm{km}}$, $\omega \leq \frac{1}{30\,\mathrm{days}}$). [Majda and Stechmann, 2011] Nonetheless, the Skeleton model has gained recognition (and its name) as it manages to reproduce the main large scale characteristics of the MJO. Its typical phase speed, horizontal structure, and dispersion relation are for the first time captured in such a minimal framework (Khouider et al., 2013).

Furthermore, for a complete understanding of the model, the following differences and extensions to the Matsuno-Gill model should be noted (see page R33 of Khouider et al. (2013) for the full dimensional equations):

- Potential temperature θ replaces pressure as given by the hydrostatic relationship formulated in terms of θ: $\frac{1}{\rho_0}\frac{\partial p}{\partial z} = g\frac{\theta}{\theta_0}$ (2.9) (Khouider et al., 2013; Majda and Stechmann, 2009).

- The vertical structure is defined differently than in Equation 2.1. Here, only the first baroclinic mode is regarded (Majda and Stechmann, 2009), i.e. $u \approx \sqrt{2}u_1 \cos(\frac{\pi}{H}z)$, $v \approx \sqrt{2}v_1 \cos(\frac{\pi}{H}z)$, $p \approx \sqrt{2}p_1 \cos(\frac{\pi}{H}z)$, $\theta \approx \sqrt{2}\theta_1 \sin(\frac{\pi}{H}z)$, and the vertical wind anomalies $w \approx \sqrt{2}w_1 \sin(\frac{\pi}{H}z)$ (2.10) (Khouider et al., 2013). The slight abuse of notation $u_1 \to u$, $v_1 \to v$, $w_1 \to w$, $p_1 \to p$, $\theta_1 \to \theta$ equally returns the shallow water equations for the dry dynamics as already mentioned by Gill (1980).
- q is not actually a first baroclinic mode variable (Thual and Majda, 2016a), but it can be defined as such (Majda and Tong, 2016). Since for $q = \sqrt{2}q_1 \sin(\frac{\pi}{H}z)$ (2.11) , $q = q_1$ at height $z = \frac{H}{4}$, i.e. in the lower troposphere, this definition would be consistent.
- a is not a first baroclinic mode variable but the envelope of integrated convective activity (Majda and Tong, 2016). Furthermore, it is the single variable that is not defined as a deviation from the radiative convective equilibrium (RCE), i.e. it is constrained to positive values (Majda and Stechmann, 2011). $\overline{H}$ is a freely selectable scaling constant, that is irrelevant to the dynamics (Majda and Stechmann, 2009).
- The nondimensional mean background vertical moisture gradient $\overline{Q}$ is constrained to values $0 < \overline{Q} < 1$ (2.12) to guarantee a positive total energy in the system (Majda et al., 2019).
- The background radiative cooling and latent heating, s^θ and s^q, are often chosen to be equal for reasons of simplicity. However, this setting does not allow for a Walker circulation (Ogrosky and Stechmann, 2015). Moreover, their shapes can be modelled to mimic realistic backgrounds, e.g. with a warm pool to represent the western Pacific as in Majda and Stechmann (2011).

variable	meaning	dimension	dimensionalization constant
t	time	s	$\sqrt{\frac{\pi}{NH\beta}}$
x, y	zonal, meridional position	m	$\sqrt{\frac{NH}{\pi\beta}}$
u, v	zonal, meridional velocity anomalies	$\frac{\text{m}}{\text{s}}$	$\frac{NH}{\pi}$
θ	potential temperature anomalies	K	$\frac{HN^2\theta_0}{\pi g}$
q	lower tropospheric moisture anomalies	none: $\frac{\text{mass of liquid}}{\text{mass of air}}$	$\frac{c_p}{L_v}\frac{HN^2\theta_0}{\pi g}$
s^θ, s^q, $\overline{H}a$	background radiative cooling, background latent heating, convective activity	$\frac{\text{K}}{\text{s}}$	$\sqrt{\frac{H^3N^5\theta_0^2\beta}{\pi^3 g^2}}$

Table 2.1: Meanings and dimensions of the variables in the Skeleton model (Stechmann and Majda, 2015).

constant	meaning	approximate value
β	meridional derivative of Coriolis parameter	$2.28 \cdot 10^{-11}\ \frac{1}{\text{ms}}$
H	tropopause height	16 km
N^2	Brunt-Väisälä frequency	$10^{-4}\ \frac{1}{\text{s}^2}$
g	gravitational acceleration	$9.8\ \frac{\text{m}}{\text{s}^2}$
θ_0	surface potential temperature	300 K
c_p	specific heat of dry air at constant pressure	$1006\ \frac{\text{J}}{\text{kg K}}$
L_v	latent heat of vaporization	$2.5 \cdot 10^6\ \frac{\text{J}}{\text{kg}}$

Table 2.2: Essential physical constants in the Skeleton model (Stechmann and Majda, 2015).

2.2.2 Numerical implementation

The numerical solution of the Skeleton model equations is based on an expansion and subsequent truncation of all variables in terms of the PCFs in meridional direction (cf. Figure 2.3):

$$\Phi_m(y) = \frac{H_m e^{\frac{-y^2}{2}}}{\sqrt{2^m m! \sqrt{\pi}}} \quad \text{with} \quad H_m(y) = (-1)^m e^{y^2} \frac{d^m}{dy^m} e^{-y^2}, \quad m \geq 0. \tag{2.13}$$

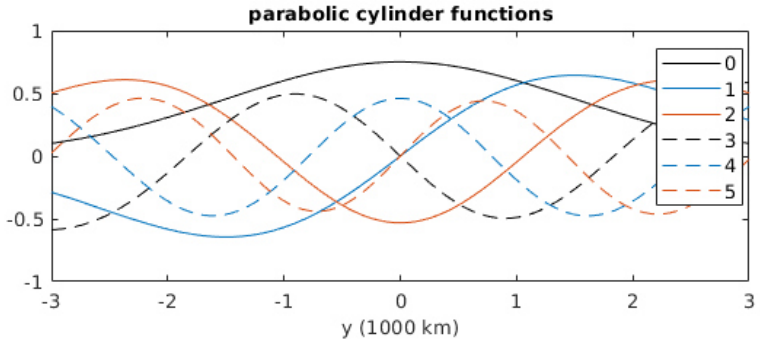

Figure 2.3: First 6 PCFs in the Skeleton model space as used for the meridional truncation.

Those are particularly applicable for modelling of tropically confined motions since $\lim_{y\to\pm\infty} \Phi_m(y) = 0$ (2.14). In order to arrive at the truncation, the dry dynamics part of the model's equations is rewritten in terms of the Riemann invariant/characteristic variables $r = \frac{u-\theta}{\sqrt{2}}$ and $l = \frac{u+\theta}{\sqrt{2}}$ (2.15), such that:

$$\begin{aligned} \frac{\partial r}{\partial t} + \frac{\partial r}{\partial x} + L_- v &= -\frac{\overline{H}a - s^\theta}{\sqrt{2}} \\ \frac{\partial l}{\partial t} - \frac{\partial l}{\partial x} - L_+ v &= \frac{\overline{H}a - s^\theta}{\sqrt{2}} \\ L_+ r - L_- l &= 0 \end{aligned} \qquad \text{with} \qquad \begin{aligned} L_- &= \frac{1}{\sqrt{2}}\left(\frac{\partial}{\partial y} - y\right) \\ L_+ &= \frac{1}{\sqrt{2}}\left(\frac{\partial}{\partial y} + y\right). \end{aligned} \tag{2.16}$$

Since the action of the operators L_- and L_+ on the PCFs is known to be simply

$$\begin{aligned} L_- \Phi_m &= -\sqrt{m+1}\Phi_{m+1} \\ L_+ \Phi_m &= \sqrt{m}\Phi_{m-1}, \end{aligned} \tag{2.17}$$

an expansion of these equations in terms of Φ_m, i.e. a decomposition $r(x,y) = \sum_{m=0}^{\infty} r_m(x)\Phi_m(y)$ and $l(x,y) = \sum_{m=0}^{\infty} l_m(x)\Phi_m(y)$ (2.18) yields:

$$\begin{aligned} \frac{\partial K}{\partial t} + \frac{\partial K}{\partial x} &= -\frac{(\overline{H}a - s^\theta)_0}{\sqrt{2}} \\ MRG &= 0 \\ \frac{\partial R_m}{\partial t} - \frac{1}{2m+1}\frac{\partial R_m}{\partial x} &= -\frac{\sqrt{2m(m+1)}}{2m+1}\left(\sqrt{m}(\overline{H}a - s^\theta)_{m+1} - \sqrt{m+1}(\overline{H}a - s^\theta)_{m-1}\right) \end{aligned} \tag{2.19}$$

with $K = r_0$, $MRG = r_1$, and $R_m = \sqrt{m+1}r_{m+1} - \sqrt{m}l_{m-1} = -2\sqrt{m}l_{m-1}, \forall\, m \in \mathbb{N}$.

This variable renaming is commonly introduced for the Skeleton model as the physical structures and propagation of the variables K, MRG (which vanishes), and R_m correspond well to the theory of unforced Kelvin, MRG, and ER waves of different meridional modes in the presence of longwave scaling

(Majda and Stechmann, 2009). By this transformation, the model's dry dynamics are reduced to a set of equations for the one-dimensional model variables K and R_m in meridional spectral space. They are of the form $\frac{\partial}{\partial t}f(x,t)+c\frac{\partial}{\partial x}f(x,t)=g(x,t)$ (2.20) , which can easily be solved in zonal Fourier space by $F(k,t+\Delta t)=F(k,t)e^{-\alpha\Delta t}+G(k,t)\frac{1-e^{-\alpha\Delta t}}{\alpha}$ with $\alpha=2\pi ikc$ (2.21). The equations for the moisture part can then subsequently be solved in physical space. (The above description of the derivation and solution of the longwave dynamics in the Skeleton model follows the internal, unpublished report in Thual and Majda (2013), but can also be understood from the explanations in Majda et al. (2019).)

The diabatic heating variables are now truncated at a meridional mode $M \geq 0$, i.e. $\overline{H}a - s^{\theta/q}(x,y) = \sum_{m=0}^{M}(\overline{H}a - s^{\theta/q})_m(x)\cdot\Phi_m(y)$ (2.22). Thereby, only certain dry dynamical wave modes, i.e. K and $R_m\,\forall\, m \in \mathbb{N} \leq M+1$, are forced and the model's complexity is reduced. [Majda and Stechmann, 2011] The truncation number M can be chosen freely, but the Skeleton model has so far most often been used in its basic version with $M=0$. An exception are studies of seasonal effects, which require a refined meridional heating structure and thus the presence of higher meridional modes, as in Thual et al. (2015). The strong truncation of the Skeleton model appears reasonable since the Kelvin wave and ER waves of lowest meridional modes are considered the most important contributions to the MJO, and an exponentially decaying meridional diabatic heating structure is a justifiable coarse approximation. Furthermore, the model shows a good representation of the MJO's large scale structure already for $M=0$ (Majda and Stechmann, 2011).

To obtain the full Skeleton model equations for $M=0$ as they are referred to in literature (Majda and Stechmann, 2011) and used in this work, R_1 is renamed to R, a_0 to A, and s_0^θ as well as s_0^q to S. q is furthermore also truncated to the first meridional mode, i.e. $q(x,y)=Q(x)\cdot\Phi_0(y)$ (2.23) , and an additional projection operator $\gamma=\int_{-\infty}^{\infty}\Phi_0(y)\Phi_0(y)\Phi_0(y)\mathrm{d}y=\sqrt{\frac{2}{3}}\pi^{-\frac{1}{4}}$ (2.24) (Majda et al., 2019; Thual et al., 2014) is introduced for the interaction between the truncated variables in the nonlinear equation:

$$\begin{aligned}
\frac{\partial K}{\partial t}+\frac{\partial K}{\partial x} &= -\frac{1}{\sqrt{2}}\left(\overline{H}A-S\right)\\
\frac{\partial R}{\partial t}-\frac{1}{3}\frac{\partial R}{\partial x} &= -\frac{2\sqrt{2}}{3}\left(\overline{H}A-S\right)\\
\frac{\partial Q}{\partial t}+\frac{\overline{Q}}{\sqrt{2}}\frac{\partial K}{\partial x}-\frac{\overline{Q}}{6\sqrt{2}}\frac{\partial R}{\partial x} &= -\left(1+\frac{\overline{Q}}{6}\right)\left(\overline{H}A-S\right)\\
\frac{\partial A}{\partial t} &= \gamma\Gamma AQ.
\end{aligned} \tag{2.25}$$

The amplitudes of the physical variables' first baroclinic modes can then be approximately recovered from the truncated model variables K, R, Q and A as (Majda and Stechmann, 2011):

$$\begin{aligned}
u(x,y) &= \left(\frac{K(x)}{\sqrt{2}}-\frac{R(x)}{2\sqrt{2}}\right)\Phi_0(y)+\frac{R(x)}{4}\Phi_2(y)\\
v(x,y) &= \left(\frac{\partial R(x)}{\partial x}-\frac{\overline{H}A(x)+S(x)}{\sqrt{2}}\right)\frac{\Phi_1(y)}{3}\\
\theta(x,y) &= \left(-\frac{K(x)}{\sqrt{2}}-\frac{R(x)}{2\sqrt{2}}\right)\Phi_0(y)-\frac{R(x)}{4}\Phi_2(y)\\
q(x,y) &= Q(x)\cdot\Phi_0(y)\\
\overline{H}a(x,y) &= \overline{H}A(x)\cdot\Phi_0(y).
\end{aligned} \tag{2.26}$$

There is thus a more complicated horizontal structure in the dry dynamic variables although the moisture variables are truncated to be $\propto \Phi_0$. Certainly, these results contain some truncation er-

ror, especially since the nonlinear interaction of Q and A could act on higher modes of a which are neglected. Nevertheless, this highly truncated model version still manages to simulate the most important large scale characteristics of the MJO (Majda and Stechmann, 2011).

The default settings for the physical and numerical discretization parameters in the Skeleton model that are commonly used in literature are arbitrary, but plausible choices. They are listed in Table 2.3. Since no spatial finite differencing is needed in the algorithm but any spatial derivatives are calculated in zonal Fourier space, it is especially the discretization in time that is critical for the model's performance.

parameter	meaning	default value (nondim.)
L	zonal length of domain	$26.\overline{6}$, i.e. 40000 km
Δx	distance between zonal gridpoints	0.4167, i.e. 625 km
n_x	number of zonal gridpoints	64
Δt	length of time steps	0.2083, i.e. 1.66h
Γ	convective activity growth rate	1.66
$\overline{Q}$	mean background vertical moisture gradient	0.9
$\overline{H}$	scaling constant for convective activity	0.22
s^θ/s^q	background diabatic cooling/heating (value at all gridpoints)	0.022

Table 2.3: Default settings for parameters in the Skeleton model (Majda and Stechmann, 2011).

2.2.3 Linearized model's eigenmodes

The most straightforward way to understand the Skeleton model's ability to represent tropical waves is to look at the plane wave eigenmodes of its linearized version (Majda and Stechmann, 2009; Majda et al., 2019). Therefore, the last equation is modified to $\frac{\partial A}{\partial t} = \gamma\Gamma\overline{A}Q$ (2.27) with $\overline{A} = S$ (2.28) and $A = \overline{A} + A'$ (2.29). This assumes small convective perturbations A' compared to the background S. With the ansatz $X(x,t) = \tilde{X}e^{i(kx-\omega t)}$ (2.30) for the state vector in model variables $X(x,t) = \begin{pmatrix} K(x,t) \\ R(x,t) \\ Q(x,t) \\ A'(x,t) \end{pmatrix}$ (2.31) and the assumption of $S(x) = \text{const.}$ (2.32), the model can then be reduced to an equation of the form $-i\omega\tilde{X} = (ikC_1 + C_2)\tilde{X}$ (2.33)with matrices $C1$ and $C2$. By this, four different eigenmodes with complex amplitudes $\tilde{X}_k^i$ and real frequencies ω_k^i are obtained for each chosen zonal wavenumber k. Moreover, for any eigenmode characterized by (k, ω_k^i, $\tilde{X}_k^i$), there exists a corresponding eigenmode characterized by ($-k$, $-\omega_k^i$, $\tilde{X}_k^{i*}$). Consequently, four purely real model states, that are propagated with phase speeds $\frac{\omega_k^i}{k}$, are given by $X_{\text{real}}(x) \propto \tilde{X}_k^i e^{ikx} + \tilde{X}_k^{i*} e^{-ikx} \propto \Re\left(\tilde{X}e^{ikx}\right)$ (2.34) for any k. Here, $\Re$ indicates taking the real part and the resulting model states can be shifted by an arbitrary phase.

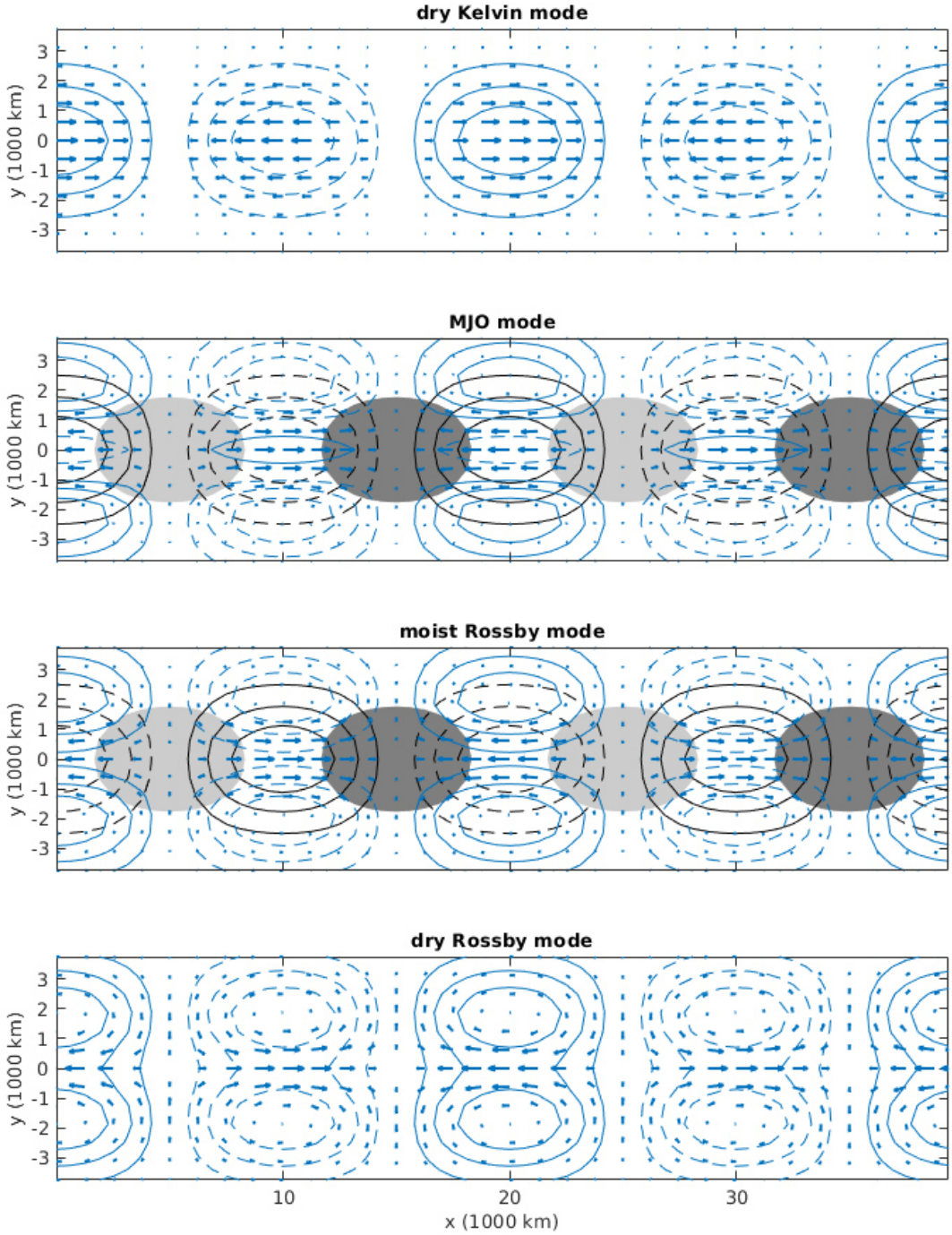

Figure 2.4: Physical structures of the eigenmodes in the linearized Skeleton model with standard parameter values for zonal wavenumber $k = \frac{2}{40000\text{ km}}$, arrows: wind field, blue lines: contours of pressure anomalies (solid=positive, dashed=negative), black lines: contours of moisture anomalies (solid=positive, dashed=negative), grey shades: convective activity anomalies (dark=positive, light=negative).

For the standard model settings and in case of small zonal wavenumbers, i.e. length scales at which the Skeleton model assumptions are justified and its results interpretable, these four basic wave modes for every k match approximately with certain theoretical or observed tropical waves. Namely, they show characteristics of dry Kelvin, MJO, moist Rossby, and dry Rossby waves. The remarkable accordance is apparent in both, their phase speeds and dispersion relations, as well as in their physical structures (cf. Figure 2.4). The latter are determined by the amount of projection on the unforced wave structures K and R, and of coupled convection Q and A. Dry Kelvin and dry Rossby modes show only little coupling to convection and typical Kelvin or Rossby like phase speeds, dispersion relations, and wind-pressure structures as in theory. Though, it should be noted, that they involve some coupling to convection and are thus distinct from the completely dry structures K and R. In contrast, moist Rossby modes are more strongly coupled to convection and share some, although incomplete, features with observed CCEWs. However, the most complete accordance with observations is present in the MJO eigenmodes of the Skeleton model. These show a strong coupling to convection with the typical pattern of an eastward moving convective center lead by moisture anomalies, and their dry dynamic structure is of mixed Kelvin and Rossby wave type with a quadrupole wind circulation that is consistent with observations of the MJO at large scales. Moreover, the phase speeds and dispersion relation of the MJO modes for small zonal wavenumbers resemble observations robustly, not only for the standard settings but over a wide range of parameter choices (Majda and Stechmann, 2009). The eigenvalues and eigenvectors for the MJO modes with $k \in \{1, 2, 3\}\ \frac{1}{40000\text{ km}}$ in the linearized Skeleton model with standard parameter values are listed in Table 2.4.

k in $\frac{1}{40000\text{ km}}$	ω in $\frac{1}{\text{days}}$	$\tilde{K}$	$\tilde{R}$	$\tilde{Q}$	$\tilde{A}'$
1	40.0	$0.3224i$	$-0.8521i$	$-0.1465i$	0.3800
2	35.4	$0.2137i$	$-0.7678i$	$-0.2472i$	0.5661
3	35.1	$0.1627i$	$-0.6728i$	$-0.2977i$	0.6771

Table 2.4: Frequencies (eigenvalues) and complex amplitudes (eigenvectors) of the plane wave MJO eigenmodes for zonal wavenumbers $k \in \{1, 2, 3\}\ \frac{1}{40000\text{ km}}$ in the linearized Skeleton model with standard parameter values.

These eigenmodes of the linearized Skeleton model version are not only interesting with respect to the representation and propagation of the associated wave types in the model but can furthermore be used for the purpose of model initialization with plausible wave activity. A realistic initialization is especially important due to the deterministic nature and conservation properties of the model version that is used in this work.

2.2.4 Properties of the highly truncated nonlinear deterministic model

The linearized version of the Skeleton model with zonally constant background diabatic cooling/heating has plane wave eigenmodes, whose major characteristics correspond well to certain tropical wave types, one of them the MJO. It thus allows for a theoretic investigation of how these basic waves are expressed in the model. However, more realistic model simulations beyond simple plane wave propagations are obtained with the nonlinear version (cf. Equations 2.25), and even more if combined with a refined background forcing. One possibility is e.g. a warm pool that mimics the warm western Pacific $S_{\text{WP}}(x) = S_{\text{const.}} \cdot \left(1 - \alpha \cos\left(\frac{2\pi x}{L}\right)\right)$ (2.35) with typically $\alpha = 0.6$ (Majda et al., 2019) and $S_{\text{const.}}$ equal to the default background. These settings allow for interactions between the basic waves, that are otherwise propagated separately in the linearized model. It was shown in Majda and Stechmann (2011) that this results in more realistic occurrences of now individual MJO events, while all important characteristics of the MJO eigenmodes, i.e. their coarse structure, phase speed, and the dispersion relation, are retained. The MJO in the nonlinear model agrees especially well with observations with regard

to its variability in strength, lifetime, and its preferential localization over the warm pool. Moreover, there are occasional realistic standing oscillations to the west of the warm pool at beginnings of MJO events.

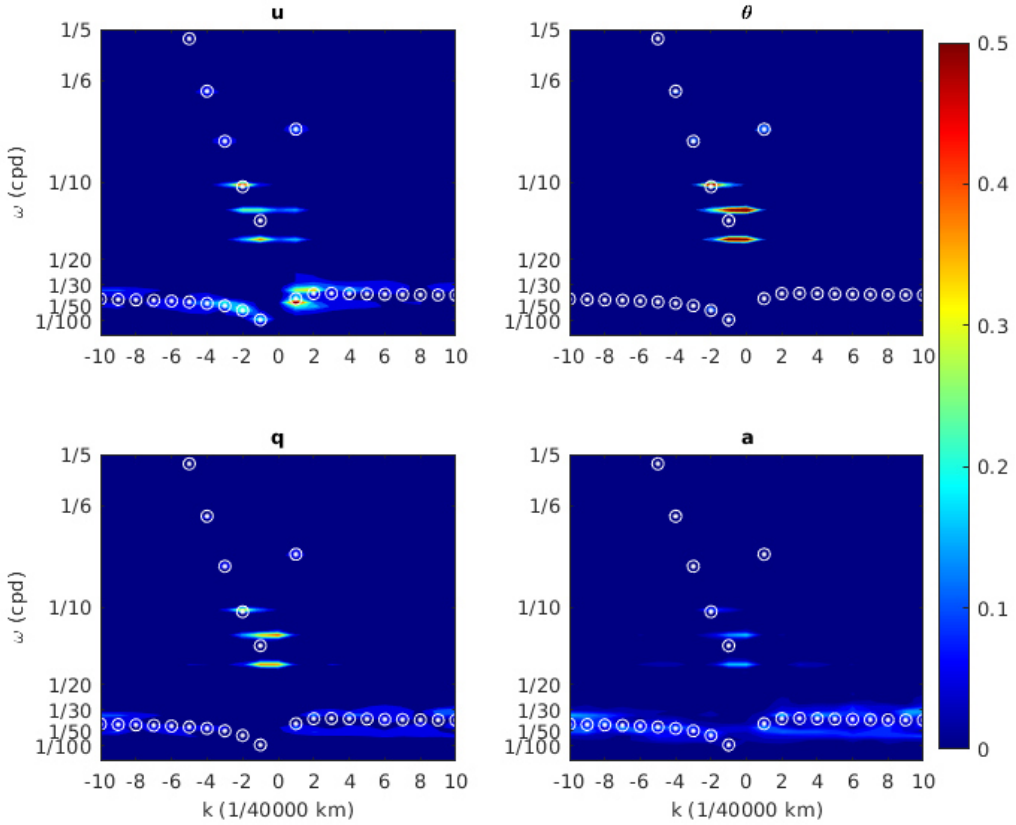

Figure 2.5: Power spectra (2D Fourier transforms in zonal space and time) of the four physical variable fields, calculated from a 1 year model run with the standard configuration, scaled by their respective climatological mean absolute deviations, superimposed dispersion curves of the linearized model's eigenmodes.

The nonlinearity and wave interactions in the Skeleton model result in a positively skewed, i.e. non-Gaussian, probability distribution for a (Majda and Stechmann, 2011). Since this is of great importance for DA, the still easy to handle nonlinear model with warm pool background is used as standard configuration throughout this work. The power spectra of all variables (cf. Figure 2.5) and Hovmöller diagram of convective activity (cf. Figure 2.6) from a model run with these settings illustrate its above mentioned features. The former shows in particular that the MJO signature is weakest on potential temperature.

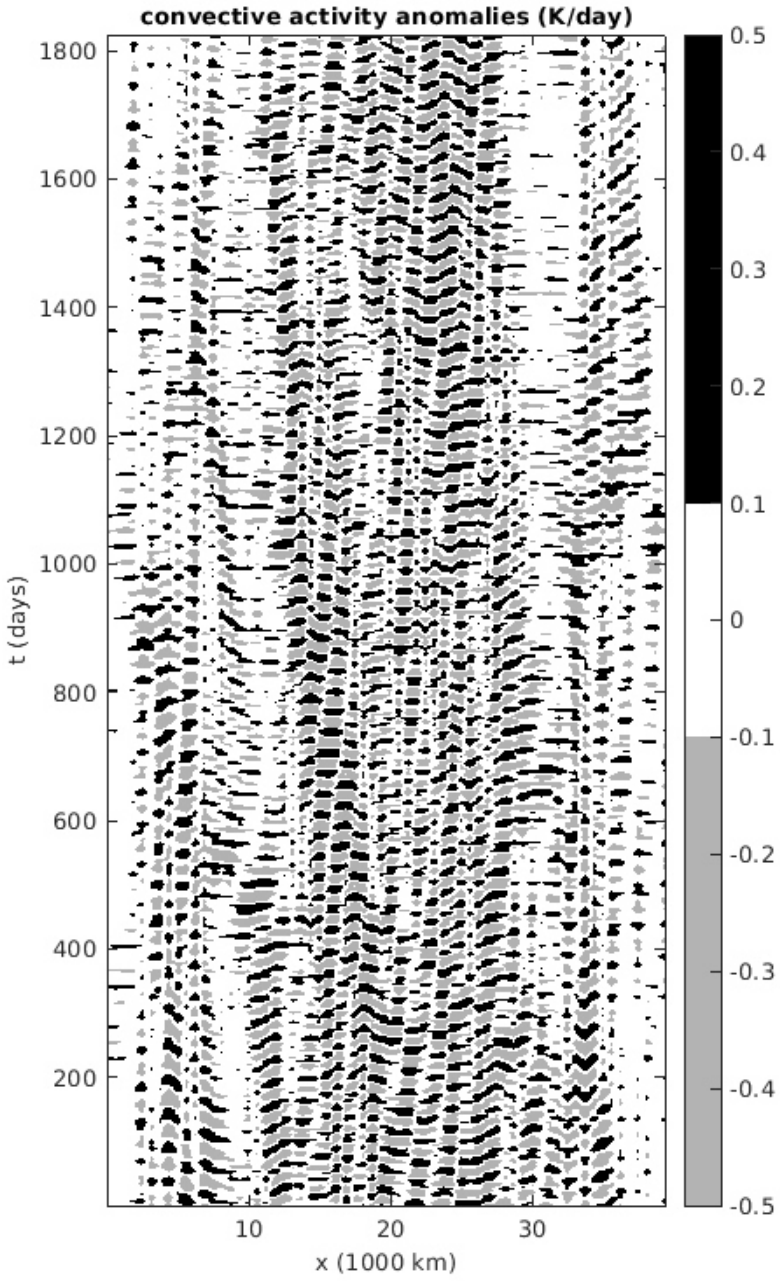

Figure 2.6: Hovmöller diagram of convective activity anomalies during a 5 year model run with the standard configuration.

Moreover interesting for DA purposes – although only approximately held in the model's meridionally truncated algorithm – are the two energy balances (Majda et al., 2019) that are incorporated in the nonlinear Skeleton model's physical equations (cf. Equations 2.8). They are valid in case of equalized background forcing $s^\theta = s^q$, as assumed by default in this work, and named according to the respective involved variables:

- moist static energy conservation: $\frac{\partial(\theta+q)}{\partial t} - \left(1-\overline{Q}\right)\left(\frac{\partial u}{\partial x}+\frac{\partial v}{\partial y}\right) = 0$ (2.36)
- total energy conservation (consisting of contributions from dry kinetic energy, potential energy, moist potential energy and convective energy):
  $\frac{\partial}{\partial t}\left(\frac{u^2}{2}+\frac{\theta^2}{2}+\frac{1}{2}\frac{\overline{Q}}{1-\overline{Q}}\left(\theta+\frac{q}{\overline{Q}}\right)^2+\frac{\overline{H}}{\Gamma\overline{Q}}a-\frac{s}{\Gamma\overline{Q}}\ln(a)\right)-\frac{\partial}{\partial x}(u\theta)-\frac{\partial}{\partial y}(v\theta)=0$ (2.37).

Because of the zonal periodicity and the tropical confinement in the Skeleton model, the domain integrated values of these energies are conserved in time.

2.2.5 Skeleton model based MJO index

Due to the bad theoretical understanding of the MJO, it is difficult to separate its pattern from data and to measure its strength. For this reason, so far mostly two different approaches have been used to set up MJO indices, that are both based on empirical MJO characteristics. Either, the data can be filtered for the typical MJO phase and group velocities at the relevant time and length scales, which can be obtained from the Wheeler-Kiladis diagram (cf. Figure 2.1). Or otherwise, the data can be projected on the most important empirical orthogonal functions (EOFs), i.e. the patterns that show the largest climatological variance on the concerned time and length scales. [Wheeler and Hendon, 2004] However, the Skeleton model provides a new option to base an MJO index on a theoretical structure without any explicit need for temporal filtering of the data, namely by projections on the eigenmodes of the linearized model version. If applied to reanalysis data, this Skeleton model based MJO index was shown to correlate highly with observed historical MJO events as well as other well-established MJO indices. [Stechmann and Majda, 2015] Moreover, it can not only be used to extract MJO patterns from real data but is also very suitable to investigate the MJO evolution within the Skeleton model itself, as necessary for this work.

To calculate the Skeleton model based MJO index as in Stechmann and Majda (2015), i.e. to extract the MJO contribution from data based on the linearized Skeleton model's MJO eigenmodes for different zonal wavenumbers k, the atmospheric state has to be expressed in terms of the zonally Fourier transformed model variables. The vectors $\tilde{X}(k)$ can then be projected on the corresponding MJO eigenvectors $e_{\mathrm{MJO}}(k)$ for a reasonably chosen range of k, e.g. $k \in \{1,2,3\}\,\frac{1}{40000\ \mathrm{km}}$. A zonal Fourier back transform subsequently yields the MJO strength distribution in physical space (called MJO Skeleton signal or index, named $MJOS(x,t)$). In order to avoid unrealistic projections of the other eigenmodes/wave types on the MJO structure, it can be helpful to use an inner product $\mathbf{M}$ with respect to which the eigenmodes $e_i(k)$ are orthogonal. Such is given by the Hessian matrix of the linearized model's total energy, that can be expressed in model variables. The projection step can thus be extended from a simple scalar product to:

$$e_{\mathrm{MJO}}(k)^\dagger \mathbf{M} \tilde{X}(k)$$
with
$$\mathbf{M} = \begin{pmatrix} 1+\frac{1}{2}\frac{\overline{Q}}{1-\overline{Q}} & \frac{1}{4}\frac{\overline{Q}}{1-\overline{Q}} & -\frac{1}{\sqrt{2}}\frac{1}{1-\overline{Q}} & 0 \\ \frac{1}{4}\frac{\overline{Q}}{1-\overline{Q}} & \frac{3}{8}+\frac{1}{8}\frac{\overline{Q}}{1-\overline{Q}} & -\frac{1}{2\sqrt{2}}\frac{1}{1-\overline{Q}} & 0 \\ -\frac{1}{\sqrt{2}}\frac{1}{1-\overline{Q}} & -\frac{1}{2\sqrt{2}}\frac{1}{1-\overline{Q}} & \frac{1}{\overline{Q}}\frac{1}{1-\overline{Q}} & 0 \\ 0 & 0 & 0 & \frac{1}{\gamma\Gamma\overline{Q}S} \end{pmatrix}. \tag{2.38}$$

2.3 Data assimilation

The subsequent section presents relevant DA foundations. After a general introduction to sequential Bayesian filtering and its particularities when applied in meteorology in 2.3.1, the stochastic EnKF is described together with the conventional tuning methods of localization and inflation in 2.3.2 and 2.3.3, respectively. The idea behind and realization of its recently proposed extension for analysis constraints is explained in 2.3.4. As those are in this work mainly used to address errors due to non-Gaussianity in the EnKF, finally, some general information on methods to measure the PDF shape of an ensemble is given in 2.3.5.

2.3.1 Sequential Bayesian state estimation

The aim of DA is to derive the best estimate for the probability density function (PDF) of the atmospheric state $\mathbf{x}_k$ at a current time t_k given observations $[\mathbf{y}_k, ..., \mathbf{y}_0]$ at times $[t_k, ..., t_0]$. Provided that the observations at different times can be assumed to be approximately independent – what could be violated e.g. due to biases or time correlated errors –, Bayes theorem yields the following relation with normalization constant C:

$$p(\mathbf{x}_k|[\mathbf{y}_k, ..., \mathbf{y}_0]) \approx C \cdot p(\mathbf{y}_k|\mathbf{x}_k)p(\mathbf{x}_k|[\mathbf{y}_{k-1}, ..., \mathbf{y}_0]). \tag{2.39}$$

Thus, if an estimate for the time evolution of the PDF $p(\mathbf{x}_{k-1}|[\mathbf{y}_{k-1}, ..., \mathbf{y}_0]) \rightarrow p(\mathbf{x}_k|[\mathbf{y}_{k-1}, ..., \mathbf{y}_0])$ is available, the current best estimate at time t_k can be derived directly from the latest estimate at time t_{k-1} once an estimation for the observation likelihood $p(\mathbf{y}_k|\mathbf{x}_k)$ has been made. Sequential DA techniques use this recursive relationship to generate initial conditions for NWP in subsequent forecast/propagation and analysis/update cycles, i.e. assimilating any observations right at the time they are taken. [Hamill, 2006]

An exact description for the PDF's time evolution in the general case of a nonlinear atmospheric model, that contains stochastic components representing its uncertainty due to model error and chaos, is given by the Fokker-Planck equation (also known as Kolmogorov forward equation) (Hamill, 2006). However, taking into account the large state spaces that are common in atmospheric applications, with dimensions up to $\propto 10^8$ in global NWP (Janjic et al., 2017), its integration, as well as the Bayesian update would have an extreme computational load (Hamill, 2006). Therefore, the exact sequential Bayesian state estimation remains a theoretical foundation in the atmospheric sciences while real world applications use several simplifications and adaptions (Hamill, 2006). The main objective of DA research is thus to find suitable algorithms that deal efficiently with the high dimensional PDF under various conditions and to mitigate errors that arise from imperfections in those.

A common first step for the simplification of the Bayesian update is to assume Gaussian PDFs $p(\mathbf{y}_k|\mathbf{x}_k)$ and $p(\mathbf{x}_k|[\mathbf{y}_{k-1}, ..., \mathbf{y}_0])$, i.e. to neglect all moments of higher order than their respective means $\mathbf{y}_k$ and $\mathbf{x}_k^b$ and covariances $\mathbf{R}_k$ and $\mathbf{B}_k$, which reduces Equation 2.39 to:

$$\begin{aligned} p(\mathbf{x}_k|[\mathbf{y}_k, ..., \mathbf{y}_0]) &\approx \frac{C}{(2\pi)^n \sqrt{\det(\mathbf{B}_k) \cdot \det(\mathbf{R}_k)}} e^{-\mathcal{J}_k} \\ \text{with } \mathcal{J}_k &= \frac{1}{2}(\mathbf{x}_k - \mathbf{x}_k^b)^T \mathbf{B}_k^{-1}(\mathbf{x}_k - \mathbf{x}_k^b) + \frac{1}{2}(\mathbf{y}_k - \mathcal{H}_k(\mathbf{x}_k))^T \mathbf{R}_k^{-1}(\mathbf{y}_k - \mathcal{H}_k(\mathbf{x}_k)). \end{aligned} \tag{2.40}$$

In the terminology common in the atmospheric sciences, $\mathbf{x}_k^b$, $\mathbf{B}_k$, $\mathbf{y}_k$, and $\mathbf{R}_k$ are called background, background error covariance, observation, and observation error covariance and $\mathcal{H}_k$ is the observation operator that projects from the n-dimensional state space into the m-dimensional space of the observations. Furthermore, the current best estimate will in the following be indicated as analysis $\mathbf{x}_k^a$.

[Janjic et al., 2017]

If the covariance matrix of the atmospheric state's PDF is estimated independently, e.g. from climatology as in the variational methods 3DVar and 4DVar, the update step is thus cut down to the minimization of the cost function $\mathcal{J}_k$ to get the PDF's mean. This best estimate can subsequently be propagated with any model in the propagation step. However, in case of persistent Gaussianity in all PDFs, the evolution of both, mean and covariance of the state estimate, can be described analytically. Starting from initial Gaussianity, this condition is fulfilled in case of a linear model $\mathbf{M}_{k,k-1}$ with additive Gaussian model error with zero mean and covariance $\mathbf{Q}_{k,k-1}$, and a linear observation operator $\mathbf{H}_k$. The set of equations for the propagation and update step is then called Kalman filter:

- forecast step:

$$\begin{aligned} \mathbf{x}_k^b &= \mathbf{M}_{k,k-1}\mathbf{x}_{k-1}^a \\ \mathbf{P}_k^b &= \mathbf{M}_{k,k-1}\mathbf{P}_{k-1}^a\mathbf{M}_{k,k-1}^T + \mathbf{Q}_{k,k-1} \end{aligned} \tag{2.41}$$

- analysis step:

$$\begin{aligned} \mathbf{x}_k^a &= \mathbf{x}_k^b + \mathbf{K}_k(\mathbf{y}_k - \mathbf{H}_k\mathbf{x}_k^b) \\ \mathbf{P}_k^a &= (\mathbf{I} - \mathbf{K}_k\mathbf{H}_k)\mathbf{P}_k^b \end{aligned} \tag{2.42}$$

  with

$$\mathbf{K}_k = \mathbf{P}_k^b\mathbf{H}_k^T(\mathbf{H}_k\mathbf{P}_k^b\mathbf{H}_k^T + \mathbf{R}_k)^{-1}. \tag{2.43}$$

Here, in conformity with the usual notation, $\mathbf{P}_k^b$ and $\mathbf{P}_k^a$ are the background and analysis error covariance matrices in the Kalman filter and $\mathbf{K}_k$ is called Kalman gain. Note furthermore, that for these equations to hold, background and observation error must be uncorrelated. The calculation of the analysis in the Kalman filter equals the result of the above cost function minimization in case of linear $\mathcal{H}$ and $\mathbf{P}_k^b = \mathbf{B}_k$. [Janjic et al., 2017]

The flow dependent error statistics in the Kalman filter are an advantage over the other aforementioned algorithms (Janjic et al., 2017). However, although the full Bayesian estimation has been largely reduced, the propagation of the error covariance matrix in the forecast step still comes at a high computational cost for large state spaces (Hamill, 2006). Evensen (1994) addressed this problem with his proposal of the Ensemble Kalman Filter (EnKF), which propagates only a Monte Carlo sample of the analysis covariance matrix and draws a sparse approximation of the background statistics in the next update step from the ensemble. This approach has moreover the benefit that a nonlinear model does not have to be linearized as the Fokker-Planck equation is approximately solved with the ensemble (Evensen, 2003). Furthermore, depending on the exact algorithm, nonlinear observation operators can also be used, which results in more exact statistics (Janjic et al., 2017).

EnKFs have become the basis for several present-day DA systems (Houtekamer and Zhang, 2016), not least also due to their simple implementation compared to 3DVar and 4DVar and the possibility to use their outcome directly for ensemble forecasts (Hamill, 2006). Yet, the ensemble approach comes with additional difficulties such as sampling errors, that make further adaptions, mostly well tuned localization and inflation, inevitable (Janjic et al., 2017). Furthermore, in the frequent case of strongly nonlinear models, the underlying requirement of persistent Gaussianity can be significantly hurt, such that methods to handle Non-Gaussianity within EnKFs have become a special research focus (Bocquet et al., 2010). This is not least due to the fact that alternative methods that can handle non-Gaussianity directly, e.g. particle filters, have so far not reached sufficient robustness and

applicability (Janjic et al., 2017; Ruckstuhl and Janjić, 2018). Additional error sources, i.e. model errors (Anderson, 2009) and certainly also missspecifications of $\mathbf{Q}_{k,k-1}$ or $\mathbf{R}_k$ (Raanes et al., 2019) are not of relevance for this work due to the identical twin experiment approach.

Another element that has to be specified in any EnKF is the initial ensemble, which should reflect the prior knowledge about the system before any current observations were taken (Evensen, 2003). Thus, in the atmospheric sciences, using climatological information to generate the initial states is a reasonable choice if no other first guess is available. However, the influence of the initial ensemble's details reduces over time in the filtering and slight missspecifications do not lead to severe differences in the filter quality (Houtekamer and Zhang, 2016). The latter is then rather determined by the observations, the forecast model, and the filter tuning and algorithm (Houtekamer and Zhang, 2016).

2.3.2 Stochastic Ensemble Kalman Filter theory

There are two fundamentally different options how to resample the ensemble with updated statistics for the next propagation step in an EnKF. One way is to generate a new ensemble deterministically by updating the mean and ensemble perturbations separately. Therefore, the background ensemble perturbations are multiplied with the square root of a matrix that is calculated such that the error covariance is updated according to the Kalman filter equations. Since the square root formulation is certainly not unique, various such filters (e.g. ETKF, EnSRF, EAKF) exist. They are contrasted by the stochastic EnKF, which employs a full Monte-Carlo approach, i.e. the ensemble members are updated individually with artificially perturbed observations whose mean is $\mathbf{y}_k$ and covariance $\mathbf{R}_k$. [Janjic et al., 2017] The fact that this procedure results in an analysis ensemble with the desired statistics can be understood from the following detailed presentation of the algorithm as in Burgers et al. (1998). Here, $\mathcal{M}_{k,k-1}$ is the now potentially nonlinear model, i the index indicating individuals of the N ensemble members, and $\mathbf{r}_k^i$ and $\mathbf{q}_{k,k-1}^i$ are random samples from the observation and model error covariance matrices, respectively, that were corrected for their sampling errors to have zero means:

- forecast step:

$$\mathbf{x}_k^{b,i} = \mathcal{M}_{k,k-1}(\mathbf{x}_{k-1}^{a,i}) + \mathbf{q}_{k,k-1}^i \tag{2.44}$$

- analysis step:

$$\mathbf{x}_k^{a,i} = \mathbf{x}_k^{b,i} + \mathbf{K}_k \left(\mathbf{y}_k + \mathbf{r}_k^i - \mathcal{H}_k(\mathbf{x}_k^{b,i}) \right) \tag{2.45}$$

  with

$$\mathbf{K}_k = \mathbf{P}_{k,n\leftarrow m}^b (\mathbf{P}_{k,m\leftarrow m}^b + \mathbf{R}_k)^{-1} \tag{2.46}$$

$$\begin{aligned}
\mathbf{P}_k^b &= \frac{1}{N-1} \sum_{i=1}^{N} \left(\mathbf{x}_k^{b,i} - \overline{\mathbf{x}_k^{b,i}} \right) \left(\mathbf{x}_k^{b,i} - \overline{\mathbf{x}_k^{b,i}} \right)^T \\
\mathbf{P}_{k,n\leftarrow m}^b &= \frac{1}{N-1} \sum_{i=1}^{N} \left(\mathbf{x}_k^{b,i} - \overline{\mathbf{x}_k^{b,i}} \right) \left(\mathcal{H}_k(\mathbf{x}_k^{b,i}) - \mathcal{H}_k(\overline{\mathbf{x}_k^{b,i}}) \right)^T = {\mathbf{P}_{k,m\leftarrow n}^b}^T \\
\mathbf{P}_{k,m\leftarrow m}^b &= \frac{1}{N-1} \sum_{i=1}^{N} \left(\mathcal{H}_k(\mathbf{x}_k^{b,i}) - \mathcal{H}_k(\overline{\mathbf{x}_k^{b,i}}) \right) \left(\mathcal{H}_k(\mathbf{x}_k^{b,i}) - \mathcal{H}_k(\overline{\mathbf{x}_k^{b,i}}) \right)^T .
\end{aligned} \tag{2.47}$$

From this follows:

$$\overline{\mathbf{x}_k^{a,i}} = \overline{\mathbf{x}_k^{b,i}} + \mathbf{K}_k \left(\mathbf{y}_k - \overline{\mathcal{H}_k(\mathbf{x}_k^{b,i})} \right)$$

and

$$\mathbf{P}_k^a = \frac{1}{N-1} \sum_{i=1}^{N} \left(\mathbf{x}_k^{a,i} - \overline{\mathbf{x}_k^{a,i}} \right) \left(\mathbf{x}_k^{a,i} - \overline{\mathbf{x}_k^{a,i}} \right)^T \tag{2.48}$$

$$\overset{\text{uncorr. back. and obs. err.}}{\approx} \mathbf{P}_k^b + \mathbf{K}_k \left(\mathbf{P}_{k,m\leftarrow m}^b + \mathbf{R}_k \right) \mathbf{K}_k^T - \mathbf{P}_{k,n\leftarrow m}^b \mathbf{K}_k^T - \mathbf{K}_k \mathbf{P}_{k,m\leftarrow n}^b = \mathbf{P}_k^b - \mathbf{K}_k \mathbf{P}_{k,m\leftarrow n}^b.$$

As the stochastic EnKF opens up easier possibilities to modify individual ensemble members, e.g. by constraints in the update, compared to square root filters, it was used as the underlying algorithm in this work although it is more prone to errors arising from spurious correlations between the background and observation ensembles (Houtekamer and Zhang, 2016).

2.3.3 Conventional tuning by localization and inflation

The single error source that is inherent to any EnKF independent of the settings are sampling errors. This is due to the fact that the atmospheric state's PDF can only be fully represented in the theoretical limit of $N \to \infty$, but the computational resources set an upper limit on the number of affordable ensemble members in practice (Houtekamer and Zhang, 2016). The impact of sampling errors on the behavior of an EnKF is not evident on first sight, but it was shown and also theoretically explained (van Leeuwen, 1999; Raanes et al., 2019) that they lead to a self enforcing decrease in ensemble spread that saturates at a level with far underestimated variance. This effect is known as filter divergence due to inbreeding. Affected are especially small ensembles as they are often found in the atmospheric sciences with typically $N \propto 10^2$ and thus $N \ll n, m$ (Houtekamer and Zhang, 2016) because the sampling error decreases $\propto \frac{1}{N}$ (Evensen, 2003). Methods to mitigate the filter divergence are therefore needed, and particularly two tuning operations, namely localization and inflation, have largely shown positive impact and have become conventional tools for EnKF tuning (Houtekamer and Zhang, 2016). Those address the root cause, i.e. wrong correlations in the background error covariance, and the effect of underestimated variances, respectively.

Localization aims to alleviate erroneous correlations in the background error covariance matrix, that is used to calculate the Kalman gain. A common approach is to assume approximate isotropy in the error covariance, meaning that long distance correlations are less trusted. In that case, the so called covariance localization, which was introduced by Houtekamer and Mitchell (2001), can be used. The background error covariance matrix is then Schur-multiplied with a positive semidefinite localization matrix $\mathcal{C}$ that smoothly dampens correlations according to their distance, i.e. $\mathbf{P}_{kL}^b = \mathcal{C} \circ \mathbf{P}_k^b$ (2.49). This yields the localized background error covariance matrix $\mathbf{P}_{kL}^b$. To calculate the amount of damping depending on the distance, frequently the following fifth order function, that was proposed by Gaspari and Cohn (1999) and is therefore called Gaspari-Cohn (GC) function, is used. It approximates a Gaussian with mean 0 and standard deviation $\frac{\sqrt{0.3}d}{2}$, but is compactly supported, such that correlations equal 0 beyond the distance d (cf. Figure 2.7):

$$GC(x,d) = \begin{cases} -8(\frac{x}{d})^5 + 8(\frac{x}{d})^4 + 5(\frac{x}{d})^3 - \frac{20}{3}(\frac{x}{d})^2 + 1, & 0 \le x \le \frac{d}{2} \\ \frac{8}{3}(\frac{x}{d})^5 - 8(\frac{x}{d})^4 + 5(\frac{x}{d})^3 + \frac{20}{3}(\frac{x}{d})^2 - 10\frac{x}{d} + 4 - \frac{1}{3}\frac{d}{x}, & \frac{d}{2} \le x \le d \\ 0, & d \le x. \end{cases} \tag{2.50}$$

However, localization can also be based on other principles than isotropy. In particular it can be meaningful to respect the climatological strength of covariances in the localization matrix. An overall

guiding principle on how to tune the localization radius for covariance localization is missing, but generally speaking, the localization radius should be chosen such that the amount of true in proportion to erroneous information is optimized, i.e. it should decrease with ensemble size. If too little information about true correlations is retained, balances can be largely affected by localization. [Houtekamer and Zhang, 2016]

Inflation, in contrast, addresses the negative influence of sampling errors by artificially increasing the underestimated error covariance, and should thus only be applied as a second measure in combination with localization. However, it can partly also account for other overlooked error sources, such as unknown model error or non-Gaussianity, and is therefore most often applied to the background ensemble before the next assimilation step (Anderson, 2009). A common approach, the so called multiplicative inflation, is to rescale the ensemble perturbations with an inflation factor β, i.e. $\mathbf{x}_k^{b,i} = \beta \cdot (\mathbf{x}_k^{b,i} - \overline{\mathbf{x}_k^{b,i}}) + \overline{\mathbf{x}_k^{b,i}}$ (2.51) . β can either be chosen as a constant slightly larger than 1, or be estimated adaptively throughout the assimilation cycles based on some self-diagnostics of the filter, for which several algorithms have been proposed. [Houtekamer and Zhang, 2016]

Besides the explained two particular examples, there exists furthermore a range of related, but nonetheless different localization and inflation options, e.g. domain localization (Janjic et al., 2017), additive inflation or relaxations to prior perturbations or spread, just to name a few (Houtekamer and Zhang, 2016). However, for the EnKF setup in the simple experiment framework in this work, the above explained methods are sufficient.

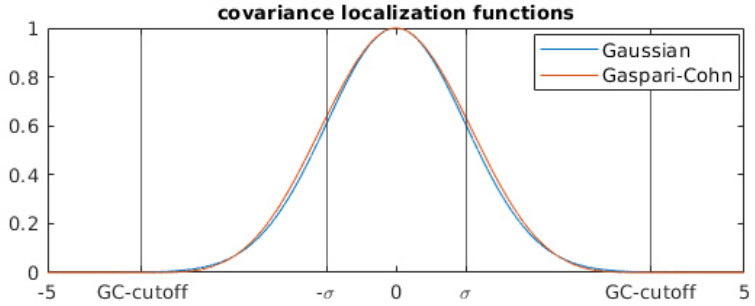

Figure 2.7: Gaussian and corresponding Gaspari-Cohn covariance localization functions with standard deviation 1, cutoff-distance d of Gaspari-Cohn function indicated.

2.3.4 Analysis constraints

In a classical EnKF algorithm as introduced above, all prior knowledge about balances between different state space locations, which is used to spread new information from observations in the update step, is provided by the estimated background error covariance. Yet, often there are additional known physical relations of the atmospheric state that are not incorporated in these correlations, either due to an erroneous background error covariance matrix, e.g. when balances are harmed by localization (Kepert, 2009), or because the system statistics can not be fully described by covariances due to non-Gaussianity (Simon, 2010). The thereby produced dynamically inconsistent states are potential significant error sources, e.g. as they can lead to artificial wave activity in following model propagations due to a readjustment to the model climate (Houtekamer and Zhang, 2016). In DA research, this issue has been addressed by its root causes in various ways, reaching from suggestions for better localization, e.g. after space transformations to more isotropic state spaces (Kepert, 2009), to algorithms that aim to better adapt EnKFs for non-Gaussian filtering (Bocquet et al., 2010). The latter also cover a wide spectrum, ranging from iterative filtering and hybrid algorithms e.g. in combination

with 3DVar, 4DVar or particle filters (Sakov et al., 2012), to the artificial generation of Gaussian conditions, e.g. by simulating the PDF with Gaussian mixtures or by Gaussian anamorphosis (Bocquet et al., 2010). However, although it is long since common practice in forecast model development, the direct incorporation of exact state constraints, such as e.g. mass, energy, or enstrophy conservation or restrictions to positivity, has only rather recently been proposed for the update algorithms of DA schemes (Janjić et al., 2014). In operational NWP, very simple adjustment mechanisms, such as truncations of undesirably negative values to zero, are still often applied (Janjić et al., 2014).

An algorithm that directly accounts for application dependent constraints in an update step and is based on the stochastic EnKF was recently developed by Janjić et al. (2014), and has shown first positive impacts when applied in toy model settings (Janjić et al., 2014; Zeng et al., 2017). The underlying idea is to generate a physically more plausible analysis ensemble and thereby a more accurate estimation for the statistics by adding the constraints to the updates of all individual ensemble members in Equation 2.45. Since the Kalman update can also be expressed as a cost function minimization (cf. Chapter 2.3.1), this yields N constrained numerical optimization problems of the general form:

$$\begin{aligned} &\min_{\mathbf{x}_k^i} \mathcal{J}_k^i \\ &\text{subject to } c_l(\mathbf{x}_k^i) = 0,\ l \in \mathcal{E} \text{ and/or } c_m(\mathbf{x}_k^i) \leq 0,\ m \in \mathcal{I} \\ &\text{with } \mathcal{J}_k^i = \frac{1}{2}(\mathbf{x}_k^i - \mathbf{x}_k^{b,i})^T {\mathbf{P}_k^b}^{-1}(\mathbf{x}_k^i - \mathbf{x}_k^{b,i}) + \frac{1}{2}(\mathbf{y}_k^i - \mathcal{H}(\mathbf{x}_k^i))^T \mathbf{R}_k^{-1}(\mathbf{y}_k^i - \mathcal{H}(\mathbf{x}_k^i)). \end{aligned} \tag{2.52}$$

An analytic formulation of such a problem is not possible independent of the exact constraints. Nevertheless, the linearity or nonlinearity of the observation operator, as well as the type of constraints, i.e. linear, convex or nonlinear-nonconvex, and equality (c_l, $l \in \mathcal{E}$) or inequality (c_m, $m \in \mathcal{I}$) as they are listed in the above equation, are important for the complexity of the numerical optimization and the guarantee of a global minimum (Janjić et al., 2014). Based on numerical optimization theory, it is useful to distinguish the following circumstances for the above equation (Optimization Toolbox™ User's Guide, R2019b, Chapter 2):

type of optimization problem	objective function requirements	constraints requirements	local minimum = global minimum	available solution algorithms
quadratic programming	quadratic, i.e. linear $\mathcal{H}$	linear equality and/or linear inequality	yes	efficient quadratic programming algorithms, e.g. active set, interior point
convex programming	quadratic, i.e. linear $\mathcal{H}$	linear equality and/or convex inequality	yes	local nonlinear programming, e.g. sequential quadratic programming
nonlinear programming	arbitrary nonlinear	arbitrary nonlinear	no	global nonlinear programming (starting local searches at many points)

In accordance with the first case, which is frequent in the atmospheric sciences since many important physical constraints are linear, the new algorithm was called Quadratic Programming Ensemble (QPEns) (Janjić et al., 2014). Certainly, it can be applied in nonlinear settings as well (Zeng et al.,

2017) with the disadvantages of higher computational demand and potential need for global minimization. However, it must be noted that the ensemble mean is not automatically constrained if nonlinear constraints are imposed on the individual ensemble members. If this mean should be used as best estimate for forecast purposes, a separate constrained calculation of the best estimate can thus become necessary. Beyond that, the QPEns could potentially also be combined with other ensemble DA methods (Janjić et al., 2014).

The algorithm used to solve the minimization problem should be chosen as optimal trade-off between efficiency, accuracy and robustness (Nocedal and Wright, 2006). In this work, the available algorithms are restricted to the several available options in the MATLAB R2019b Optimization Toolbox. The ones of relevance for this work can be assigned to the following two general categories:

- active-set methods: problem solved sequentially with reduced sets of active equality constraints; these active sets are updated after each iteration
- interior-point methods: problem solved sequentially without inequality constraints but with penalty terms in the objective function for values close to inequality constraint boundaries; the penalty terms are updated after each iteration.

While interior-point algorithms have the benefits of a smaller memory demand and higher efficiency in solving large problems, their penalty terms keep the solution away from the inequality constraint boundaries, which can lead to a slightly reduced accuracy of the result. [Optimization Toolbox™ User's Guide, R2019b, Chapter 2] A more thorough introduction to constrained optimization theory that goes beyond these coarse descriptions is not given here. Further algorithmic details are not important in this work's toy model setting as it allows for sufficiently accurate results at reasonable computational expense with any of the available algorithms. However, detailed information on the Karush-Kuhn-Tucker (KKT) optimality criteria and various solution algorithms can be found in Nocedal and Wright (2006). Moreover, for global optimization, the Global Optimization Toolbox was available.

Whereas the QPEns represents the exact solution of the stochastic EnKF equations subject to precise constraints, a more approximate, but in certain points beneficial alternative is to include equality constraints as so called soft constraints via pseudo-observations. For a constraint $\mathcal{D}(\mathbf{x}_k^i) = \mathbf{d}$ (2.53), $\mathbf{d}$ is then taken as observations, $\mathcal{D}$ replaces the observation operator $\mathcal{H}$, and furthermore nonzero constraint tolerances are specified as variances of a diagonal pseudo-observation error covariance matrix. The latter avoids a singular observation error covariance matrix that could potentially pose ill-conditioning problems. This approach requires less computational resources than the QPEns, can easily be combined with any type of filter, thus also more sophisticated filter algorithms beyond the stochastic EnKF, and allows for uncertainty in the constraints, e.g. in case the true value is not exactly known. However, constraints must be equality constraints and exactly known constraints can be violated, although the pseudo-observation variances can be chosen rather small. [Simon, 2010]

2.3.5 Measuring non-Gaussianity

If a univariate PDF is considered, the distribution's moments are scalar values and thus easily accessible measures to grasp its shape. To get a feeling for its non-Gaussianity, especially the skewness γ and kurtosis κ, that are proportional to the third and fourth order moments, are frequently used. This is due to the fact that Gaussians are fully determined by the first two moments, i.e. mean and variance, and generally have $\gamma_G = 0$ and $\kappa_G = 3$. With the excess kurtosis defined as $\kappa_e = \kappa - \kappa_G = \kappa - 3$ (2.54), an intuitive interpretation of skewness and kurtosis is given by longer tails to the right or left side for $\gamma > 0$ or $\gamma < 0$ and a sharper or broader peak for $\kappa_e > 0$ or $\kappa_e < 0$, respectively (cf. Figure

2.8). The calculation of their expectation values, i.e. unbiased estimates, from an N-member sample is straightforward (Kondo and Miyoshi, 2019; Joanes and Gill, 1998):

$$\begin{aligned} E(\gamma) &= \frac{\sqrt{N(N-1)}}{N-2}\frac{m_3}{m_2^{3/2}} \\ E(\kappa_e) &= \frac{(N-1)}{(N-2)(N-3)}\left[(N+1)\frac{m_4}{m_2^2} - 3(N-1)\right] \\ &\text{with} \\ m_r &= \frac{1}{N}\sum_{i=1}^{N}(x_i - \overline{x})^r. \end{aligned} \tag{2.55}$$

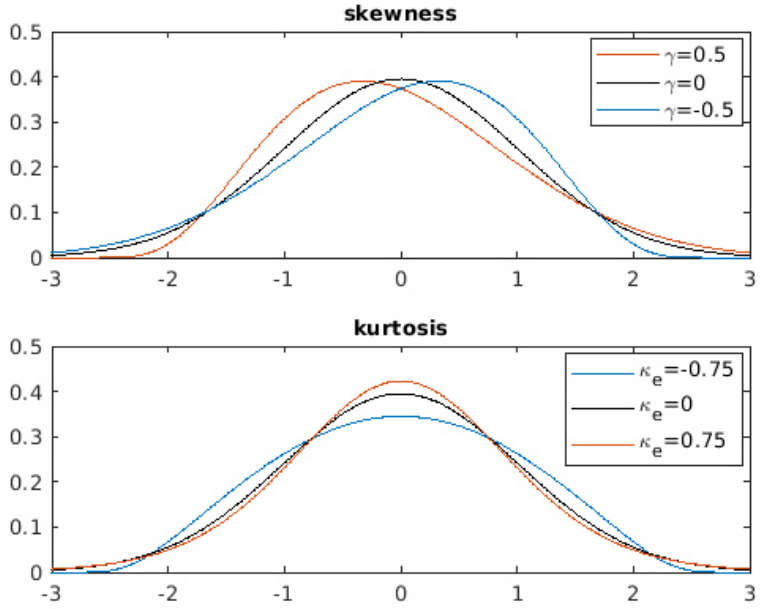

Figure 2.8: PDF shapes for different values of skewness γ and excess kurtosis κ_e generated as Pearson system distributions with mean $\mu = 0$ and standard deviation $\sigma = 1$ ($\gamma = 0$, $\kappa_e = 0$ if not indicated otherwise).

The above introduced measures of skewness and kurtosis provide insight into the accordance of some important shape characteristics with a Gaussian based on simple calculations, but they do not offer an absolute quantification of non-Gaussianity. For this, the Kullback-Leibler divergence (KL divergence or also relative entropy) can be used, which comes from signal and information theory and is defined as the information gain from a distribution q to a distribution p:

$$\mathcal{KL}(p,q) = \int p(\mathbf{x}) \ln\left[\frac{p(\mathbf{x})}{q(\mathbf{x})}\right] \mathrm{d}\mathbf{x}. \tag{2.56}$$

The KL divergence of a PDF p and its corresponding Gaussian q with equal mean and variance – the order is important since the KL divergence is not symmetric – thus quantifies the non-Gaussianity in p. [Bocquet et al., 2010] To calculate it from a sample, the sample's distribution has to be approximated e.g. via a histogram or with kernel smoothing.

Skewness, kurtosis, and KL divergence are meaningful on first sight and comparably simple to estimate in a univariate setting. However, in a multivariate case, the moments are no longer scalar and the estimation of the samples PDF p to calculate the KL divergence becomes difficult. Therefore, the aforementioned methods to measure non-Gaussianity are frequently applied to only single variables, marginal sets of the higher-dimensional statespace, or other combined measures of variables (e.g. sums) that appear reasonable. [Bocquet et al., 2010]

3 Methods

3.1 Identical twin experiments

The following chapter describes the setup of the identical twin experiments with the Skeleton model in detail. In 3.1.1, the idea behind the general approach is presented together with the model settings employed in this work and the configuration of the available state spaces for the update step. Thereafter, in 3.1.2 the initialization, i.e. the construction of the initial synthetic truth and ensemble, and the retrieval of relevant information from the model's climatology are outlined. The generation of the synthetic observations and their perturbations for the stochastic EnKF are explained in 3.1.3. All variables that are unexplained in the following sections were introduced in Chapter 2 and are listed in Appendix A.

3.1.1 General approach

This work is not aimed at the assessment of model imperfections in the Skeleton model, but at the improvement of the DA update step under the assumption that dynamics and convection coupling are well described by the Skeleton model. Therefore, an identical twin experiment approach was chosen, meaning that a synthetic 'truth' and synthetic 'observations' were generated from a nature run with exactly the same model version that was used for the ensemble propagation in the examined DA systems. For first simplified experiments, this is advantageous as the model is perfect and the observations' PDF, i.e. the distribution from which the observations were sampled, is exactly known. Model error in $\mathcal{M}_{k,k-1}$, or missspecifications of $\mathbf{Q}_{k,k-1}$ or $\mathbf{R}_k$ are thus omitted, and the error sources in the filter are reduced to unavoidable sampling imperfections and non-Gaussianity effects. Consequently, those can be addressed more easily. Furthermore, the true state is given precisely, which simplifies the assessment of the investigated DA algorithms. However, the results obtained with the identical twin experiments in this work certainly need to be verified later on in more sophisticated settings, e.g. using non-identical/fraternal twins or real observations, before finding their way into operational NWP.

The typical Skeleton model setup that was used for the identical twin experiments in this work is the fully truncated nonlinear deterministic version as in Equations 2.25 in the standard configuration with warmpool background that is described in Chapter 2.2.4. Any modifications of these settings with respect to certain parameters, such as especially the warm pool intensity, are clearly indicated throughout the following chapters.

The DA algorithms were built around the preexisting Skeleton model code in this work. Therefore, two fundamentally different options, that are suitable for different targets, were exploited. Either, the filtering was done in physical space (u, θ, q, a) with a back and forth variable transformation before and after every update step , respectively, or in model space (K, R, Q, A). The former mimics a more realistic situation with observations that are better comparable to available real data, whereas the latter allows for a more direct investigation of the importance of the dry Kelvin and Rossby waves' physical structures in DA for MJO prediction. However, it should be noted that the physical space that was used here, still assumes all variables to be the amplitudes of the first baroclinic vertical mode meridionally projected on the first PCF, which amongst others means that any meridional winds v are neglected. This is possible because any projections on higher order PCFs for u, θ, and v, that can be calculated from the model variables as in Equations 2.26, are not dynamically important, but conditional on the projections of u and θ on the first PCF. One can deduce this from the fact that the latter are sufficient to calculate the model variables in Equations 2.19. This truncated approach for the physical space is especially beneficial from a computational viewpoint because the state space

dimension is maintained at four variables with merely zonal extend throughout the transformation from model space. The experiments are therefore equally easy to handle. Yet, it should be kept in mind that artificial observations of these physical variables do not represent real observations in a full 3D physical grid, but rather combinations of observations that can be used to project on the considered vertical and meridional structures.

3.1.2 Initialization and climatology calculation

The initialization of the Skeleton model was done with the eigenmodes of the linearized model version as described in Chapter 2.2.3. Hence, the initially present waves could be chosen from dry Kelvin, MJO, moist Rossby and dry Rossby modes of different zonal wavenumbers k and amplitudes ${\alpha_X}^i_k$, i.e. $X_{\text{ini}}(x) = \sum \left[{\alpha_X}^i_k \Re \left(\tilde{X}^i_k e^{ikx} \right) \right]$ (3.1), where $\Re$ again indicates taking the real part. Since the model is deterministic and holds two energy conservation principles as explained in Chapter 2.2.4, it is apparent that the properties of a model run are highly affected by the initialization. The standard initialization used in this work was therefore chosen by analogy with the scenario WP-MJO in Majda and Stechmann (2011) as a $k = 2$ MJO mode, and the default amplitude was set to $\alpha_X = 0.05$.

After the model initialization and prior to any experiments, a spin up run of typically 10 years was conducted, during which the model climatology could build up due to nonlinearity effects and interactions with the warmpool background (see Figure 7 in Majda and Stechmann (2011) for a visualisation of the model spin up). This was followed by a longer model run, whose evolution was used to generate a climatological ensemble. From this, some important climatological information could be retrieved, e.g. about the precision with which the model balances are held (see Chapter 4.1.3), or the shape of the climatological PDF such as covariances (see Chapter 4.1.2) and the amount of non-Gaussianity in individual variables' distributions (see Chapter 4.1.4). The final state of this preparatory model run was used as the initial truth. Moreover, the initial ensemble for the filtering was also taken from this climatology as it reasonably represents the available prior information on the atmospheric state. Furthermore, thus generated initial ensemble members could be shown to have a covariance matrix of maximum possible rank and to be approximately orthogonal (see Chapter 4.1.1), i.e. to cover an as wide as possible part of the state space. These properties were considered sufficient and no further requirements were imposed on the initial ensemble due to its subordinate role for the general filter quality after its spin up.

The selection of the states for the climatological ensemble and the initial ensemble was set up such that the former reflect an equally distributed spectrum of times throughout the seasons, and the latter are all located at the same seasonal time, that was chosen as starting point for the first assimilation cycle. Although this requires an initial long model run of several years and would not have been necessary in this work since the model was used with a uniform background over time, this procedure was nevertheless implemented in preparation for future studies with potential seasonality.

3.1.3 Synthetic observations

The filtering update step was implemented in both, physical and model space. As the respective variables were mimiced to be observed directly for reasons of simplicity and clarity, i.e. not via combined or otherwise related variables, the synthetic observations were also generated in both state spaces. This had the advantage that the observation operator was always linear and had the simple shape of a rectangular matrix of size $m \times n$ with only 0 or 1 as entries. Those were determined by the arbitrary locations of the observations within the state space. Moreover, all observations were defined to be uncorrelated, such that the observation error covariance matrix was diagonal. Its diagonal en-

tries, i.e. the variances, were specified as percentages of the variables' climatological variances, where 10 % was taken as default value. Furthermore, the frequency of the observations could be chosen freely.

With these settings, the observations $\mathbf{y}_k$ were generated as a Gaussian random sample with the current truth $\mathbf{x}_k^t$ as mean and the observation error covariance matrix $\mathbf{R}_k$ as covariance. The perturbed observations $\mathbf{r}_k^i + \mathbf{y}_k$, that are required in the stochastic EnKF as explained in Chapter 2.3.2, were subsequently equally drawn as normally distributed random states from the observation error covariance matrix $\mathbf{R}_k$, but with the observations $\mathbf{y}_k$ as mean. After that, the sample $\mathbf{r}_k^i$ was additionally corrected for the sampling error in the mean $\mathbf{r}_k^i - \overline{\mathbf{r}_k^i} \rightarrow \mathbf{r}_k^i$ (3.2) to avoid unintentional changes of the observations $\mathbf{y}_k$.

For the convective activity, which is confined to positive values, the above procedure was modified in order to ensure any observations and perturbed observations of a or A to be positive. This is expected to produce better filter results as it helps to maintain physically plausible states. Therefore, the samples of $\mathbf{y}_k$ and thereafter also $\mathbf{y}_k + \mathbf{r}_k^i$ were both transformed to samples of the lognormal distribution with the same mean and variance, i.e. $\mathbf{x}_{new}^i = \mathrm{CDF}_{\mathrm{lognl}}^{-1}\mathrm{CDF}_{\mathrm{gauss}}(\mathbf{x}^i)$ (3.3) for ensemble members $\mathbf{x}^i$. Here, $\mathrm{CDF}_{\mathrm{gauss}}$ and $\mathrm{CDF}_{\mathrm{lognl}}$ are the cumulative distribution functions (CDFs) of the Gaussian distribution from which the sample $\mathbf{x}^i$ was drawn, and the lognormal distribution with equal mean and variance, respectively. Moreover, the above described sampling error correction can not be done for convective activity observations since again negative values could thereby be produced. As approximate solution, that does not erase the sampling error completely, but was found to draw the mean closer to $\mathbf{y}_k$, the above transformation was repeated in a similar way, i.e. $\mathbf{x}_{new}^i = \mathrm{CDF}_{\mathrm{lognl}}^{-1}\mathrm{CDF}_{\mathrm{curr.lognl}}(\mathbf{x}^i)$ (3.4). $\mathrm{CDF}_{\mathrm{curr.lognl}}$ is the CDF of the lognormal distribution that has the actual mean and standard deviation of the current sample. In these transformations, a lognormal distribution was chosen, instead of e.g. a Γ-distribution, since $\lim_{\mathbf{x}\rightarrow 0} \mathrm{PDF}_{\mathrm{lognl}}(\mathbf{x}) = 0$ (3.5) for any arbitrary values of mean and variance. Thereby, computational problems are avoided and a physically plausible distribution of the observations is ensured. Furthermore, the lognormal distribution approaches a Gaussian in case of sufficiently small probabilities of values close to 0.

3.2 Data assimilation algorithms

In this section, detailed information is given on the implementation of the DA systems that were tested. The tuning of the underlying stochastic EnKF by various localization and adaptive inflation options is presented in 3.2.1. Thereafter, its extension by analysis constraints to a QPEns is described in 3.2.2, where the different constraints and the applied optimization algorithms are specified. Finally, in 3.2.3, the alternative realization of any linear analysis constraints as soft constraints is explained.

3.2.1 Stochastic Ensemble Kalman Filter

As a basis for all other DA algorithms that were set up in this work, a stochastic EnKF was implemented according to the description in 2.3.2. Subsequently, it was tuned with a covariance localization and adaptive multiplicative inflation based on the methods explained in 2.3.3.

For the construction of the localization matrix, two different approaches were taken, that could also be combined. Namely, it could be derived from the covariances in the climatological ensemble or a classical distance dependent damping could be applied. The former was achieved with the following steps that return a positive semidefinite matrix whose entries $\in [0, 1]$ reflect approximately the typical strength of correlations in the climatology:

- calculation of the climatological ensemble's covariance matrix
- transforming all matrix elements to their absolute values (this produces purely positive localization values, that do not change signs when applied to covariances, but dampen according to the strengths of the respective climatological covariances)
- eigenvalue decomposition of the matrix and construction of a similar positive semidefinite matrix from all eigenvectors to eigenvalues ≥ 0
- if the matrix' minimum entry is negative, adding its absolute value to all entries (this does not affect the positive semidefiniteness, but produces localization values ≥ 0)
- scaling all entries with standard deviations of the concerned variables (this does neither affect the positive semidefiniteness, but produces localization values $\in [0, 1]$, i.e. as in a correlation matrix).

The isotropy based localization matrices, that were used complementary to or instead of the thus calculated climatological localization matrix, were constructed either with a Gaussian or with its compactly supported approximation by a Gaspari-Cohn (GC) function. Therefore, each entry was determined as the value of the respective function for the distance between the concerned gridpoints. The distance that defines the standard deviation of the Gaussian, or the corresponding Gaussian in case of a GC function, could be chosen freely. Its share of the whole domain (40000 km) is further referred to as localization radius, e.g. a localization radius of 0.5 means that covariances of variables with a distance of 20000 km are dampened by a factor $\frac{1}{e}$. The Gaussian localization option was implemented additionally to the GC function because the easy to handle toy model state space in this work did not imply any necessity to use a compactly supported function for reasons of computational expense. Therefore, the choice was taken such that the best filter quality could be achieved. Which localization technique of the above presented, and which localization radius for which ensemble size are most suitable, was investigated experimentally (see Chapter 4.2.1).

Besides the localization, an additional inflation of the background ensemble was applied in each update step to counteract the remaining variance underestimation. To compute the adaptive inflation factor, two rough assumptions were made. Firstly, due to the unclear contribution of non-Gaussianity to the ensemble spread decrease and the lack of other possibly missspecified error sources such as

model error, the filter divergence by inbreeding was considered to be caused mainly by sampling errors. And secondly, the localization was assumed to be perfect, i.e. removing any sampling errors from the covariance matrix. With these approximations, the background ensemble $\mathbf{x}_{k+1}^{b,i}$ could easily be rescaled to meet the amount of variance that was theoretically expected for the analysis ensemble of the previous update step $\mathbf{x}_k^{a,i}$. Therefore, the inflation factor β_{k+1} was calculated as the quotient between the trace of the analysis covariance matrix as given by the analytic Kalman filter update of the localized background error covariance matrix, i.e. the theoretically expected variances $tr(\mathbf{P}_{k\text{th}}^a)$, and the trace/variances of the actual ensemble derived analysis covariance matrix $tr(\mathbf{P}_{k\text{ens}}^a)$:

$$\beta_{k+1} = \sqrt{\frac{tr(\mathbf{P}_{k\text{th}}^a)}{tr(\mathbf{P}_{k\text{ens}}^a)}} = \sqrt{\frac{tr\left(\mathcal{C} \circ \mathbf{P}_k^b - [\mathcal{C} \circ \mathbf{P}_k^b]\mathbf{H}_k^T \left(\mathbf{H}_k[\mathcal{C} \circ \mathbf{P}_k^b]\mathbf{H}_k^T + \mathbf{R}_k\right)^{-1} \mathbf{H}_k[\mathcal{C} \circ \mathbf{P}_k^b]\right)}{tr\left(\mathbf{P}_k^a\right)}}. \tag{3.6}$$

Certainly, this procedure is only applicable in a toy model setting since the calculation of β_{k+1} would be unaffordable in case of higher state space dimensions and is not very robust with respect to changes in the localization technique. Yet, in most cases in this thesis, it was possible to maintain a reasonable ensemble spread with this method. Therefore, its application seemed justifiable since the aim of this work was not the algorithmic improvement of the EnKF tuning. Only in some experiments, depending on the observational setup, the adaptive inflation was not sufficient to prevent a significant decrease in the ensemble spread, probably due to additional error sources or missspecifications in the localization. It was then complemented by an additional constant inflation factor β_c, that was heuristically tuned in each case separately.

The inflation could in principle be applied alternatively to the analysis ensemble of the previous update step without any changes in the calculation of the inflation factor. However, the background inflation was chosen in order to avoid the destruction of potential nonlinear constraints, and moreover to mitigate the occurrences of negative convective activity values in the analysis ensemble. Yet, the latter could appear anyway if no constraint to positive values was used. For this reason, an additional relaxation of any negative convective activity values in the analysis ensemble to 10^{-5} was implemented. They were not set exactly to 0 since this would have completely prevented any convective activity evolution at the concerned gridpoint in the subsequent model propagation due to the nonlinear oscillator relationship in Equations 2.25.

3.2.2 Quadratic Programming Ensemble

To test the influence of certain analysis constraints on the filter quality, the stochastic EnKF has been extended to an ensemble of constrained optimization problems as described in Chapter 2.3.4. Although also nonlinear constraints have been implemented, this algorithm will in the following throughout be called Quadratic Programming Ensemble (QPEns) in analogy to Janjić et al. (2014). Since the observation operator was linear as explained in Chapter 3.1.3, the cost function was always quadratic. Its minimization could thus be reformulated into the following problem, where the quadratic structure of the objective function is clearly visible and its Hessian and gradient can be directly read off:

$$\begin{aligned} \min_{\mathbf{z}_k^i} \mathcal{J}_k^i = \frac{1}{2}{\mathbf{z}_k^i}^T \left(\mathbb{1} + (\mathbf{H}_k\mathbf{X}_{kL}^b)^T\mathbf{R}_k^{-1}\mathbf{H}_k\mathbf{X}_{kL}^b\right)\mathbf{z}_k^i + \left(\mathbf{H}_k\mathbf{x}_k^{b,i} - \mathbf{r}_k^i - \mathbf{y}_k\right)^T \mathbf{R}_k^{-1}\mathbf{H}_k\mathbf{X}_{kL}^b\mathbf{z}_k^i \\ \text{subject to } c_l(\mathbf{x}_k^{b,i} + \mathbf{X}_{kL}^b\mathbf{z}_k^i) = 0,\ l \in \mathcal{E} \text{ and/or } c_m(\mathbf{x}_k^{b,i} + \mathbf{X}_{kL}^b\mathbf{z}_k^i) \leq 0,\ m \in \mathcal{I}. \end{aligned} \tag{3.7}$$

Here, $\mathbf{X}_{kL}^b$ signifies the square root of the localized background error covariance matrix that was gained by Cholesky decomposition, i.e. $\mathbf{P}_{kL}^b = \mathbf{X}_{kL}^b{\mathbf{X}_{kL}^b}^T$ (3.8), and a variable transformation $\mathbf{x}_k^i \rightarrow \mathbf{z}_k^i$ was made with $\mathbf{x}_k^i = \mathbf{x}_k^{b,i} + \mathbf{X}_{kL}^b\mathbf{z}_k^i$ (3.9). As this transformation is linear, it does not change the respective

linear or nonlinear nature of the constraints.

In principle, any constraints could be implemented in the QPEns if the optimization problems are solved with a nonlinear programming algorithm. However, for reasons of simplicity, only certain general constraints were used independently of the state space in which the DA was performed. Additional more specific constraints, that could only be expressed in complex nonlinear functions in physical space, were made available exclusively for the filtering in model space. Divided into these two categories, all constraints that were set up in this work are listed in the following:

- General constraints
  - constraints of the domain integrated physical model balances, i.e. moist static (ME) and total (TE) energies (see Chapter 2.2.4), to the truth's values; calculated from the zonal amplitudes of the variables' projections on the first PCF in meridional direction, i.e. the physical space variables, and with nonlinear contributions assumed to project on the first PCF:
    $ME = \sum_x (\theta + q) \int_{-\infty}^{\infty} \Phi_0(y) \mathrm{d}y$ (3.10) and
    $TE = \sum_x \left(\frac{u^2}{2} + \frac{\theta^2}{2} + \frac{1}{2} \frac{\overline{Q}}{1-\overline{Q}} \left(\theta + \frac{q}{\overline{Q}} \right)^2 + \frac{\overline{H}}{\Gamma \overline{Q}} a - \frac{s^{\theta/q}}{\Gamma \overline{Q}} \ln(a) \right) \int_{-\infty}^{\infty} \Phi_0(y) \mathrm{d}y$ (3.11)
  - constraint of TE approximated as linearization around the background to the truth's total energy; calculated from the physical space variables as above
  - constraint of the domain integrated dry mass (DM) to the truth's value (since this was shown in earlier studies to play a possible important role (see e.g. Janjić et al., 2014; Ruckstuhl and Janjić, 2018), is an important balance for many NWP models, and is conserved in its long time average in the Skeleton model); calculated from the physical space variables:
    $DM = \sum_x \theta \int_{-\infty}^{\infty} \Phi_0(y) \mathrm{d}y$ (3.12)
  - constraint of convective activity to positive values.

- Constraints available for filtering in model space
  - constraints of the moist static energy, total energy, linearized total energy, and dry mass to the truth's value with taking into account additionally any available projections of variables on higher order PCF as derived from Equations 2.26.

The linearizations around the background were done according to $f(\mathbf{z}_k^i) \approx f(\mathbf{x}_k^{b,i}) + \nabla f(\mathbf{x}_k^{b,i}) \mathbf{X}_{kL}^b \mathbf{z}_k^i$ (3.13). For the more sophisticated calculations of the physical constraints, which take into account higher order meridional distributions of the variables, all contributions of zonal summations were weighted according to their meridional integration by computation of the integrals $\int_{-\infty}^{\infty} \Phi_0(y) \mathrm{d}y = 1.8828$, $\int_{-\infty}^{\infty} \Phi_2(y) \mathrm{d}y = 1.3313$, $\int_{-\infty}^{\infty} \Phi_0(y) \Phi_0(y) \mathrm{d}y = 1$, $\int_{-\infty}^{\infty} \Phi_0(y) \Phi_2(y) \mathrm{d}y = 0$ and $\int_{-\infty}^{\infty} \Phi_2(y) \Phi_2(y) \mathrm{d}y = 1$. Moreover, the last nonlinear term of the total energy equation was reformulated as follows:

$$
\begin{aligned}
&\int_{-\infty}^{\infty} [S \cdot \Phi_0(y)] \left[\ln(A \cdot \Phi_0(y)] \, \mathrm{d}y = \right. \\
&S \ln(A) \int_{-\infty}^{\infty} \Phi_0(y) \mathrm{d}y + S \int_{-\infty}^{\infty} \Phi_0(y) \ln(\Phi_0(y)) \, \mathrm{d}y = \\
&S \ln(A) \int_{-\infty}^{\infty} \Phi_0(y) \mathrm{d}y + S \int_{-\infty}^{\infty} \frac{e^{-\frac{y^2}{2}}}{\pi^{\frac{1}{4}}} \left(-\frac{y^2}{2} - \ln(\pi^{\frac{1}{4}}) \right) \mathrm{d}y = \\
&S \ln(A) \int_{-\infty}^{\infty} \Phi_0(y) \mathrm{d}y + S \int_{-\infty}^{\infty} \left(-\ln(\pi^{\frac{1}{4}}) \Phi_0(y) - \frac{-\frac{y^2}{2} e^{-\frac{y^2}{2}}}{\pi^{\frac{1}{4}}} \right) \mathrm{d}y =
\end{aligned}
\tag{3.14}
$$

$$S\ln(A)\int_{-\infty}^{\infty}\Phi_0(y)\mathrm{d}y + S\int_{-\infty}^{\infty} -\ln(\pi^{\frac{1}{4}})\Phi_0(y)\mathrm{d}y - \frac{\sqrt{\frac{\pi}{2}}}{\pi^{\frac{1}{4}}}.$$

While in case of filtering in model space these extensions of the constraints are quite straightforward and any linear constraints stay linear, they would be more complicated in case of filtering in physical space.

The algorithm for the constrained optimizations in the QPEns could be chosen from the MATLAB functions 'quadprog' and 'fmincon', that are most suitable for smooth quadratic and nonlinear programming, respectively. They come with several solvers, of which those that are applicable for this work can be assigned to the two general algorithmic categories of interior-point (solvers: 'interior-point-convex' for 'quadprog'; 'interior-point' for 'fmincon') or active-set (solvers: 'active-set' for 'quadprog'; 'sqp', 'sqp-legacy', 'active-set' for 'fmincon') methods. The underlying mechanisms, as well as benefits and drawbacks of these two classes are described in Chapter 2.3.4. In principle, all of these solvers lead to sufficiently accurate solutions for the purposes of this work, and efficient optimization is not of great importance in the toy model setting and not in the focus of this work. Therefore, any of them could be selected without influencing this thesis' results. Yet, in the following, the interior point algorithms were used in favor of their slight advantage in speed. Furthermore, it is in this specific setting even beneficial if solutions at the bound of the only potential inequality constraint, i.e. the positivity of convective activity, are inhibited by a penalty function. As stated earlier, values of convective activity equal to zero prevent any dynamics in convective activity at the concerned grid-point. Besides this choice of the algorithm and some parallelizations when possible, no further effort was made regarding computational efficiency. Moreover, all experiments in this work were conducted with only local optimization even in presence of nonlinear constraints, since the thus found minima seemed sufficient to test the relevant effects on the DA quality. However, optional global minimization with the MATLAB function 'GlobalSearch', that runs local minimizations from a number (default: 1000) of automatically generated starting points, was additionally implemented with 'fmincon' as local solver. Yet, its success depends on whether one of the starting points is located in the basin of attraction of a global minimum, such that the returned optimum can not be guaranteed to be global.

Many of the algorithms' details are described in Optimization Toolbox™ User's Guide (R2019b) and the following links are furthermore provided for their comprehension:

- general description of quadprog with a list of all settings:
  https://www.mathworks.com/help/optim/ug/quadprog.html
- details of quadprog solvers' algorithms:
  https://de.mathworks.com/help/optim/ug/quadratic-programming-algorithms.html
- general description of fmincon with a list of all settings:
  https://www.mathworks.com/help/optim/ug/fmincon.html
- details of fmincon solvers' algorithms:
  https://de.mathworks.com/help/optim/ug/constrained-nonlinear-optimization-algorithms.html
- general description of GlobalSearch with a list of all settings:
  https://www.mathworks.com/help/gads/globalsearch.html
- details of the GlobalSearch algorithm:
  https://www.mathworks.com/help/gads/how-globalsearch-and-multistart-work.html.

The default settings of the algorithms were not changed except for specifications of any gradients and Hessians of the objective function and constraints, which yields faster and more reliable results. Furthermore, for any nonlinear minimizations, the background ensemble states were provided as starting points. Most important for the solutions' accuracy though are the tolerance on constraint violations and the values of the stopping criteria. The latter are the lower bounds on the first order optimality

measure according to the KKT-conditions, on the step size, and on the change of the objective functions value, as well as the maximum numbers of iterations and of function evaluations. However, those can not simply be chosen as small as computationally affordable since smaller values do not always result in higher accuracy, but can also prevent a solver from recognizing a minimum and force continued useless iterations. It is for this reason, that the default settings were considered to be sufficiently well chosen and not modified.

3.2.3 Soft constraints

Additionally to the exact constraints in the QPEns, optional soft constraints, i.e. pseudo-observations, as described in Chapter 2.3.4 were implemented for any linear constraints of the above listed. By restricting this approach to only linear relationships, the extended observation operator was maintained linear, which simplified the computations. An exemplary linear constraint $\mathbf{D}\mathbf{x}_k^i = \mathbf{d}$ (3.15) that was implemented as soft constraint with a nonzero constraint tolerance $\mathbf{R}^c$, i.e. pseudo-observation variance, introduced the following changes to the observations, observation operator and observation error covariance matrix:

$$\begin{aligned} \mathbf{H}_{k,new} = \begin{bmatrix} \mathbf{H}_k & 0 \\ 0 & \mathbf{D} \end{bmatrix}, \mathbf{R}_{k,new} = \begin{bmatrix} \mathbf{R}_k & 0 \\ 0 & \mathbf{R}^c \end{bmatrix}, \\ \text{and} \quad \mathbf{y}_{k,new} = \begin{pmatrix} \mathbf{y}_k \\ \mathbf{d} \end{pmatrix}. \end{aligned} \tag{3.16}$$

In case of linearized, originally nonlinear constraints, $\mathbf{D}$ and $\mathbf{d}$ were specific to the point around which the linearization was made, thus mostly a different background state for every individual ensemble member. In that case, the soft constraints required separate calculations of $\mathbf{H}_{k,new}$ and $\mathbf{y}_{k,new}$ for the updates of the ensemble members. $\mathbf{R}^c$ was by default chosen as 1 % of the concerned conservation property's climatological variance.

3.3 Diagnostics

In the following, the diagnostics that were used to assess the DA systems are described. Starting with some general verification metrics for the accuracy of a state estimate with respect to the truth and for the ensemble spread in 3.3.1, a more specific evaluation of the filter quality, that regards the individual tropical wave types in the Skeleton model, is presented in 3.3.2. Moreover, the influences of DA on conservation properties and the ensemble's PDF shape can be observed as explained in 3.3.3 and 3.3.4, respectively. Lastly, the computation of zonal wavenumber-frequency power spectra, that can be used to visualize the MJO signal comparable to the Wheeler-Kiladis diagram (cf. Figure 2.1), is outlined in 3.3.5.

3.3.1 General verification metrics

For a basic assessment of any DA system with the identical twin experiments some general verification metrics were set up. These are not specifically tailored for this work's purposes, e.g. to examine the representation of non-Gaussian statistics or the MJO, but give a feeling for the overall filter quality in knowledge of the truth. Therefore, the standard measures of root mean square error (RMSE) and pattern correlation/Pearson correlation coefficient (PCC), that can be found in many meteorological publications, were adopted for the evaluation of the current best estimate, i.e. here ensemble mean. They were complemented by a measure for the relative ensemble spread (RES), that puts the ensemble spread in relation to the error of the best estimate. Their detailed calculations and specifications are explained in the following, where $\boldsymbol{\mu}_c$ and $\boldsymbol{\sigma}_c$ are the n-dimensional vectors of the climatological mean and standard deviation, respectively. ./ signifies a pointwise division, and a differentiation is made between the best estimate/analysis $\mathbf{x}_k^a$ and the ensemble mean $\overline{\mathbf{x}_k^{a,i}}$, such that these measures could also be applied in case of a separate calculation of the best estimate in future work. Although stated here for the whole n-dimensional state space, any of these verification metrics could certainly be equally calculated for only a subset, e.g. a specific variable, of the state space:

- Root mean square error (RMSE) of the best estimate with respect to the truth; standard deviation of the errors in the best estimate scaled by the climatological standard deviations; possible values are $\in [0, \infty]$:

$$RMSE = \sqrt{\frac{1}{n} \left[\left(\mathbf{x}_k^a - \mathbf{x}_k^t\right) ./ \boldsymbol{\sigma}_c\right]^T \left[\left(\mathbf{x}_k^a - \mathbf{x}_k^t\right) ./ \boldsymbol{\sigma}_c\right]}. \tag{3.17}$$

- Pearson correlation coefficient (PCC), often also referred to as pattern correlation, between the best estimate and the truth; measure for the correlation between the spatial patterns in the best estimate and the truth; possible values are $\in [-1, 1]$:

$$PCC = \frac{\left(\mathbf{x}_k^t - \boldsymbol{\mu}_c\right)^T \left(\mathbf{x}_k^a - \boldsymbol{\mu}_c\right)}{\sqrt{\left(\mathbf{x}_k^t - \boldsymbol{\mu}_c\right)^T \left(\mathbf{x}_k^t - \boldsymbol{\mu}_c\right)} \sqrt{\left(\mathbf{x}_k^a - \boldsymbol{\mu}_c\right)^T \left(\mathbf{x}_k^a - \boldsymbol{\mu}_c\right)}}. \tag{3.18}$$

- Relative ensemble spread (RES); ratio between the mean absolute deviation of the ensemble members from their mean and the mean absolute deviation of the best estimate from the truth; all contributions scaled by the respective climatological standard deviations; possible values are $\in [0, \infty]$, but should be around 1 throughout the whole filtering process if the ensemble statistics are a good representation of the insecurity in the analysis:

$$RES = \frac{\sum_n \left[\overline{\left|\mathbf{x}_k^{a,i} - \overline{\mathbf{x}_k^{a,i}}\right|} ./ \boldsymbol{\sigma}_c\right]}{\sum_n \left[\left|\mathbf{x}_k^a - \mathbf{x}_k^t\right| ./ \boldsymbol{\sigma}_c\right]}. \tag{3.19}$$

3.3.2 Wave indices

For the assessment of the DA algorithms' ability to filter the distinct wave types that are present in the Skeleton model, i.e. dry Kelvin, MJO, moist Rossby and dry Rossby waves, indices analogue to the MJO index, which is described in Chapter 2.2.5, were set up for all four of them. They all use the same inner product $\mathbf{M}$. Since most power in the Skeleton model is expressed in the zonal wavenumbers $k \in \{1, 2, 3\}\, \frac{1}{40000\ \mathrm{km}}$, as visible in the nature run's power spectrum (cf. Figure 2.5), only their corresponding eigenvectors were taken into account for the projections. Moreover, for the MJO index, an optional preceding filtering of the model output for the typical MJO frequency band of $\frac{1}{90\,\mathrm{days}} \leq \omega_{\mathrm{MJO}} \leq \frac{1}{30\,\mathrm{days}}$ (3.20) was implemented to make the extraction of MJO structures more robust. However, this is only mentioned as theoretical option, but turned out to be not necessary for a sufficient separation of the MJO from the other waves and was thus not applied in the further experiments. The patterns in the time evolution of the wave indices were investigated in a nature run and found to show clearly distinct properties that can be associated with the propagation of the different wave types (see Chapter 4.1.5).

The calculated signals represent the spatial, thus in this truncated model version zonal, distribution of the waves' strengths. Therefore, the pattern correlation and RMSE of the best estimate's indices compared to the truth's corresponding indices were calculated as a straightforward measure for the filtering skill with respect to the waves. This was done analogous to Equations 3.17 and 3.18, where the indices replace the respective state vectors and $\boldsymbol{\sigma}_c$ and $\boldsymbol{\mu}_c$ are the climatological mean and standard deviations of the indices.

3.3.3 Conservation properties

To see how balances in the Skeleton model are affected by the filtering, and furthermore to verify the implemented analysis constraints, some properties of the best estimate and the ensemble members could be calculated at all time steps throughout the experiments. These include, analogue to the implemented constraints as described in Chapter 3.2.2, the physical conservation properties and dry mass calculated from the variables projections on the first meridional PCF as well as from all available meridional components. Furthermore, the following three conservation properties that are exactly held in the model's truncated algorithm were assessed:

- $C1 = \sum_x -\frac{4K}{3} + R$ (3.21)
- $C2 = \sum_x \sqrt{2}K + \frac{1}{\overline{Q}-1}\left(Q - \overline{Q}(\frac{K}{\sqrt{2}} + \frac{R}{2\sqrt{2}})\right)$ (3.22)
- $C3 = \sum_x \frac{K^2}{2} + \frac{3\sqrt{2}R^2}{32} + \frac{\overline{Q}}{2(1-\overline{Q})}(\frac{Q}{\overline{Q}} - \frac{K}{\sqrt{2}} - \frac{R}{2\sqrt{2}})^2 + \frac{\overline{H}A}{\gamma\Gamma\overline{Q}} - \frac{S}{\gamma\Gamma\overline{Q}}\ln(A)$ (3.23).

3.3.4 PDF shape diagnostics

In order to measure the non-Gaussianity present in the model's climatology or in the filter's ensemble, the computations of skewness, excess kurtosis and KL-divergence from a sample as explained in Chapter 2.3.5 were used. They were only applied univariately to single state space positions. This approach kept the calculations simple and was considered sufficient due to the strong non-Gaussianity that is already present in convective activity, the variable with the strongest non-Gaussianity, at single gridpoints.

To determine the KL-divergence of a sample, its PDF shape had to be approximated. This was done by distributing all sample elements in bins and subsequent scaling of all values in the bins such that their integration equals 1, i.e. the construction of a probability density scaled histogram. Thereby,

a stepwise PDF p was gained, that could thereafter optionally be smoothed by the calculation of moving averages. Critical for the shape of p and thus the accuracy of the KL-divergence measure are therefore mostly the freely selectable number of bins and the smoothing width. An alternative to this procedure would have been to use kernel smoothing for the estimation of the PDF, but this was found to be much more prone to errors due to unsuitable choices of the kernel, especially for highly skewed distributions. For the final calculation of the KL-divergence, the values of the corresponding Gaussian PDF q with the same mean and standard deviation were computed at the centers of the bins. The integration was subsequently carried out numerically. If p contained any 0 values, e.g. if any bins were empty by chance and no smoothing was applied, the contributions of these bins to the KL-divergence were directly set to 0, since the MATLAB computation of $p(\mathbf{x}) \ln \left[\frac{p(\mathbf{x})}{q(\mathbf{x})}\right] = 0 \cdot (-\infty)$ (3.24) would otherwise result in NaN as output for the whole integral, although $p \ln \frac{p}{q} \to 0$ for $p \to 0$.

3.3.5 Power spectra

Besides the above diagnostics that all look at certain properties of the best estimate or ensemble at a certain time, the zonal wavenumber-frequency power spectra of the best estimate and the truth could be calculated during filtering and forecast. Therefore, a two-dimensional Fourier transform in zonal space and time was applied to the model data. Although the power spectra do not yield any information about the accuracy of the filter's result at a given time, they could however provide insight into the potential emergence of new artificial wave types or the attenuation of model inherent wave types due to DA. Nevertheless, in this work, they were only used for the visualization of the model properties (cf. Figure 2.5).

4 Results

4.1 Relevant climatological properties of the Skeleton model

In this chapter, the climatological properties of the Skeleton model in the version and standard settings used in this work are described and visualized. The focus is thereby put on characteristics that are relevant for DA and its assessment. Typical atmospheric states are shown in 4.1.1 and analyzed with respect to their orthogonality in the state space. Subsequently, the model's climatology is investigated regarding the variables' covariances in physical and model space in 4.1.2, the accuracy of the physical and algorithmic balances in 4.1.3, and the amount of non-Gaussianity in the variables in 4.1.4. Finally, in 4.1.5, the expression of the four wave types in the Skeleton model is visualized by the application of the wave indices to a nature run.

4.1.1 Typical atmospheric states

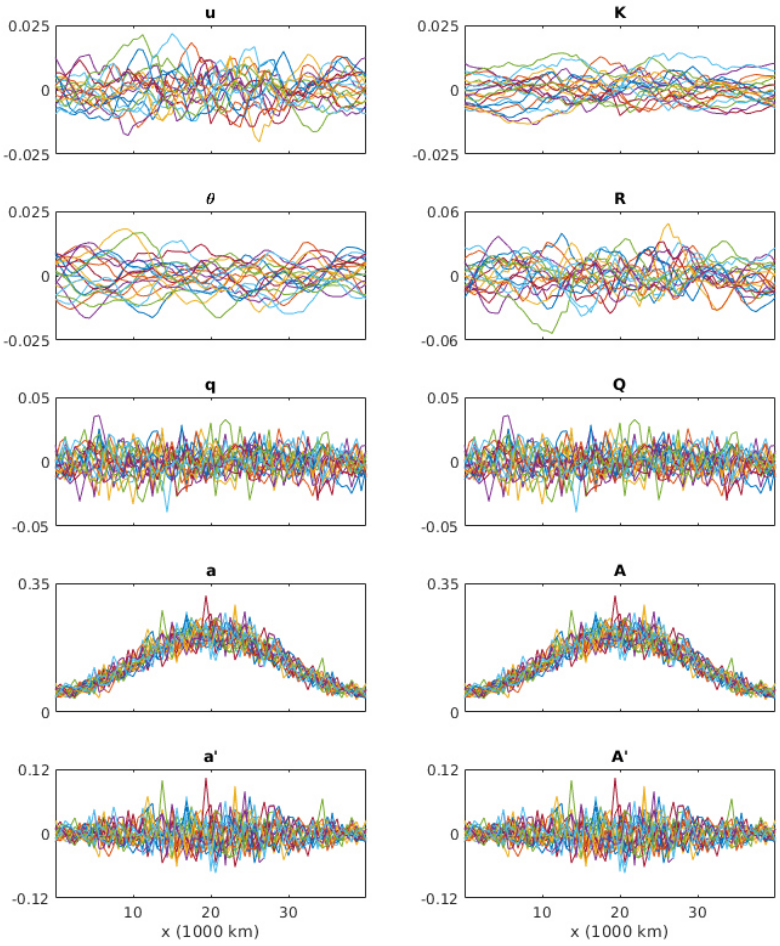

Figure 4.1: 20 initial ensemble members in physical (left) and model (right) space, i.e. yearly climatological states collected from 20 years of model simulation.

A look at a 20-member initial ensemble (cf. Figure 4.1), that was retrieved in physical as well as model space from climatology, shows the typical dimensions and patterns of the non-dimensional variables in the Skeleton model. It should be noted that the variables q or Q, a or A and consequently a' or A' are identical in both state spaces. Moreover, all variables are approximately of the same order of magnitude and about orthogonal (cf. Figure 4.2). The states covariance matrix has the maximum possible rank of 19 in both spaces.

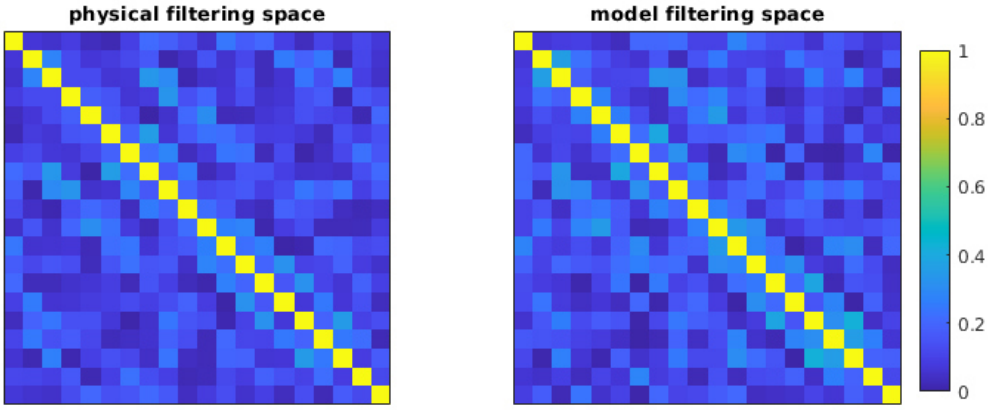

Figure 4.2: Orthogonality measures of the above 20 initial ensemble members in physical (left) and model (right) space, calculated by the scalar products scaled by the square roots of the corresponding vector lengths: $o_{i,j} = \frac{\mathbf{x}_i \circ \mathbf{x}_j}{\sqrt{|\mathbf{x}_i||\mathbf{x}_i|}}$.

4.1.2 Covariances

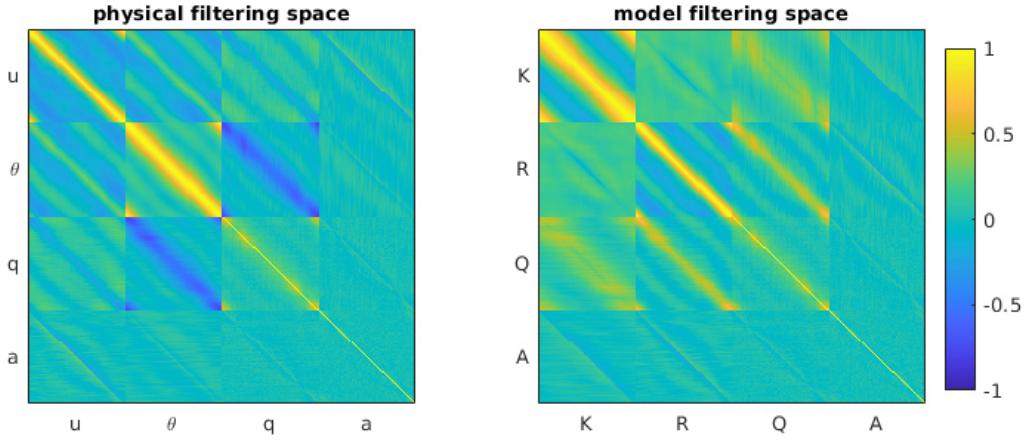

Figure 4.3: Correlation matrices (i.e. covariances scaled by the products of the corresponding variables' standard deviations) of a 1000-member climatological ensemble in physical (left) and model (right) space.

The typical covariances in the Skeleton model were derived from a large, 1000-member climatological ensemble (cf. Figure 4.3). Most noticeable is that the convective activity is only weakly coupled to the other variables within a narrow spatial correlation length, and moreover any intravariable covariances between convective activity values at different gridpoints have negligible magnitudes. The latter is

approximately true also for the moisture variable q or Q, which is however more strongly linked to the dry dynamics. All covariances show a strong distance dependence, whose length scale differs depending on the concerned variables and gridpoints. It is largest for the intravariable correlations of potential temperature or the structure of the dry Kelvin wave in the physical or model space, respectively. Furthermore, there are several off-diagonal covariance peaks which indicate a dominance of structures with zonal wavenumber 2.

4.1.3 Balances

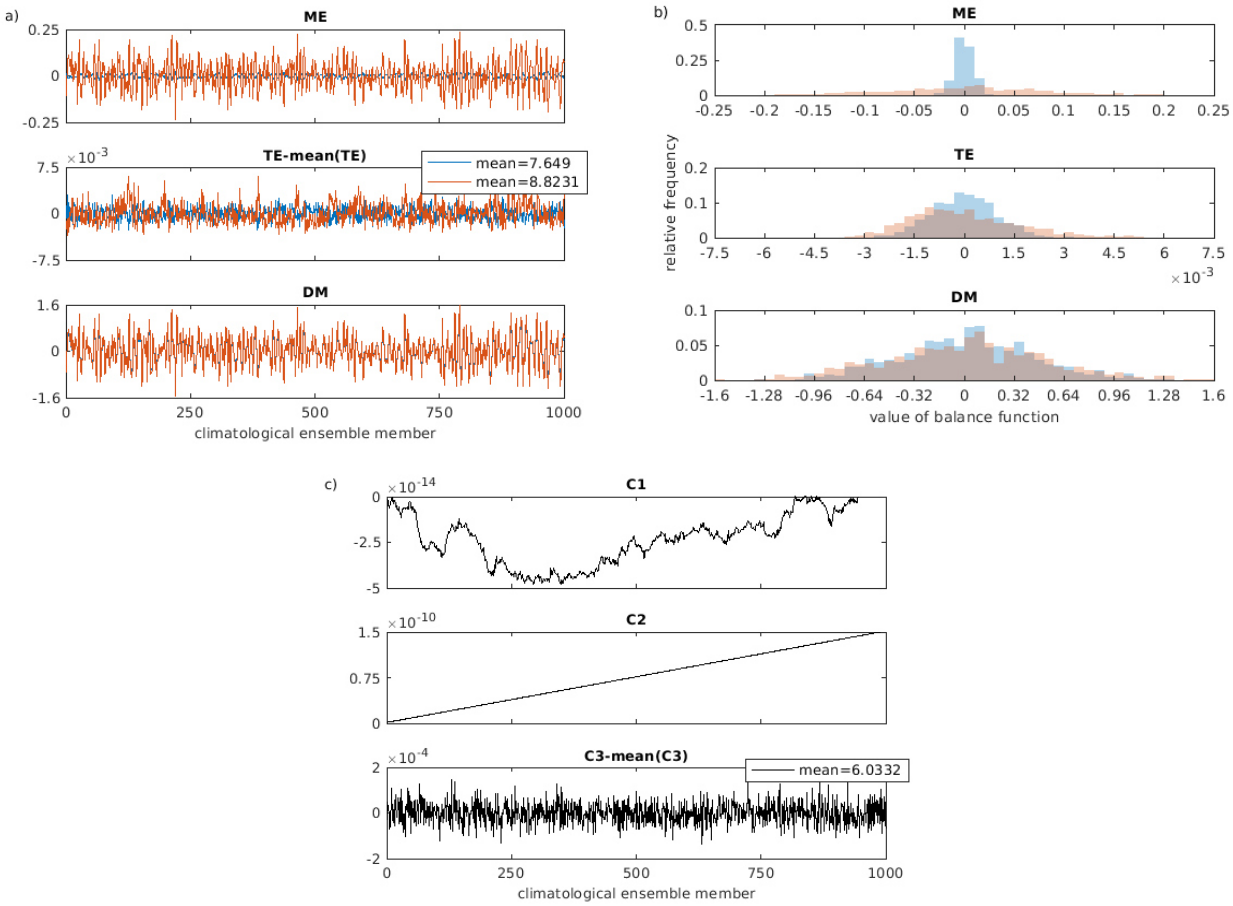

Figure 4.4: a) values of physical balances in a 1000-member climatological ensemble (blue: calculated from physical space variables, i.e. projections only on the first PCF, red: calculated taking into account any available contributions from projections on higher order PCFs), b) corresponding histograms scaled to represent relative frequencies, c) values of algorithmic conservation properties in the same ensemble.

The 1000-member climatological ensemble was furthermore used to investigate how accurate the physical balances and algorithmic conservation properties, that are described in Chapters 3.2.2 and 3.3.3, are fulfilled in the model (cf. Figure 4.4). In general, all quantities were found to be approximately conserved over time with different amounts of oscillation around the true value. As expected, the latter is largest for the dry mass, which is not actually conservative in the underlying equations, but only conserved in its long time average. Smaller oscillations that are only due to truncation and numerical errors are present in the physical model balances, i.e. moist static energy and total energy. It is especially noticeable that those are better held if calculated only from the variables' projections

on the first PCF, thus neglecting any higher order contributions. For this reason, only those were used as constraints and diagnostics throughout all presented experiments, and any further mentions of ME, TE, or DM refer to them. Finally, subject to exclusively numerical errors are the algorithmic conservation properties, which are thus very well conserved with only slight deviations, i.e. minimal drifts in $C1$ and $C2$ and somewhat larger, but still small oscillations in $C3$. The properties $C1$, $C2$, ME and the long time average of DM have a theoretical value of 0 due to their linearity in combination with all involved variables being deviations from a background mean state. In contrast, $C3$ and TE are nonzero due to nonlinear terms and the involvement of absolute convective activity.

4.1.4 Non-Gaussianity

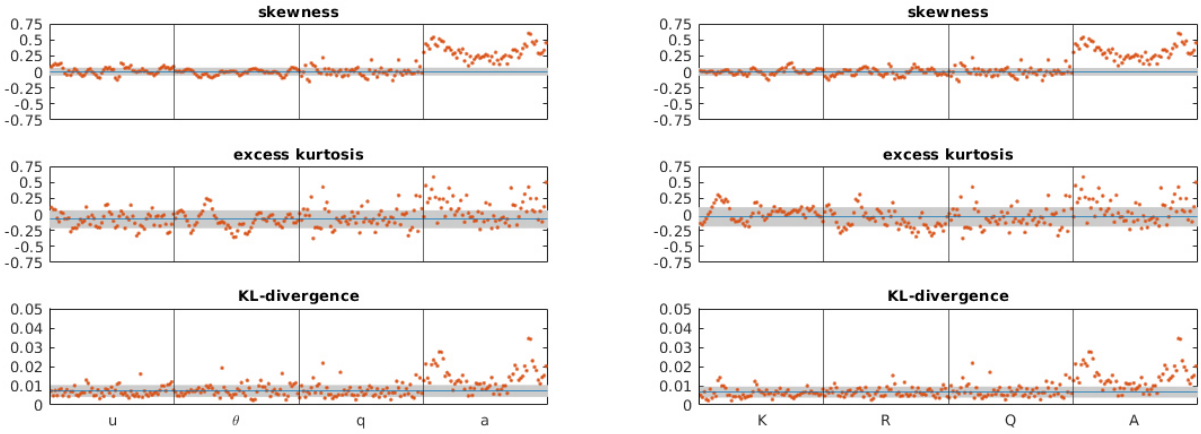

Figure 4.5: Skewness, excess kurtosis and KL-divergence in a 1000-member climatological ensemble in physical (left) and model (right) space, horizontal blue line and grey shading: mean and standard deviation in the dry dynamic variables and moisture, KL-divergence calculated with 50 histogram bins and a moving average smoothing over 10 bins.

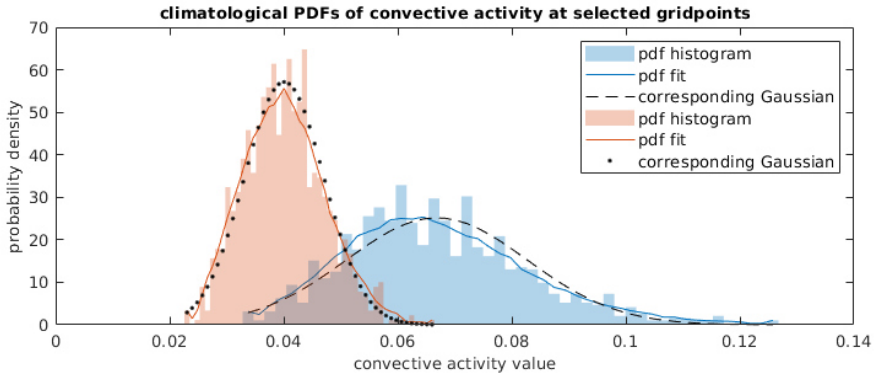

Figure 4.6: Probability density scaled histograms of convective activity at the gridpoints with highest KL-divergence (blue) and smallest background forcing (red), superimposed PDF fits and Gaussian functions with same means and standard deviations as used for the KL-divergence calculation.

The non-Gaussianity in the model was examined by the calculation of the univariate diagnostics skewness, excess kurtosis, and KL-divergence as described in Chapter 3.3.4 from the 1000-member climatological ensemble (cf. Figure 4.5). While the dry dynamic variables and moisture are approx-

imately Gaussian distributed with on average only slightly positive skewness and negative kurtosis, there is significant non-Gaussianity in the convective activity. This is especially pronounced in regions of small background forcing, i.e. outside of the warmpool. However, it is important to note that the enhanced skewness of convective activity in this area is not simply due to an accumulation of values very close to 0 as one could expect at positions with small mean convective activity from the variable's strict positivity constraint. In fact, with the model version and settings used here, even at the gridpoints with the highest skewness or with the smallest background forcing, the convective activity distribution is positioned with a clear gap above 0 (cf. Figure 4.6). Moreover, the result that the PDF shapes of the other variables appear rather unaffected by the amount of non-Gaussianity in the convective activity distribution can be explained by the weak coupling via covariances between those two variable groups as seen in Chapter 4.1.2.

4.1.5 Wave types expression

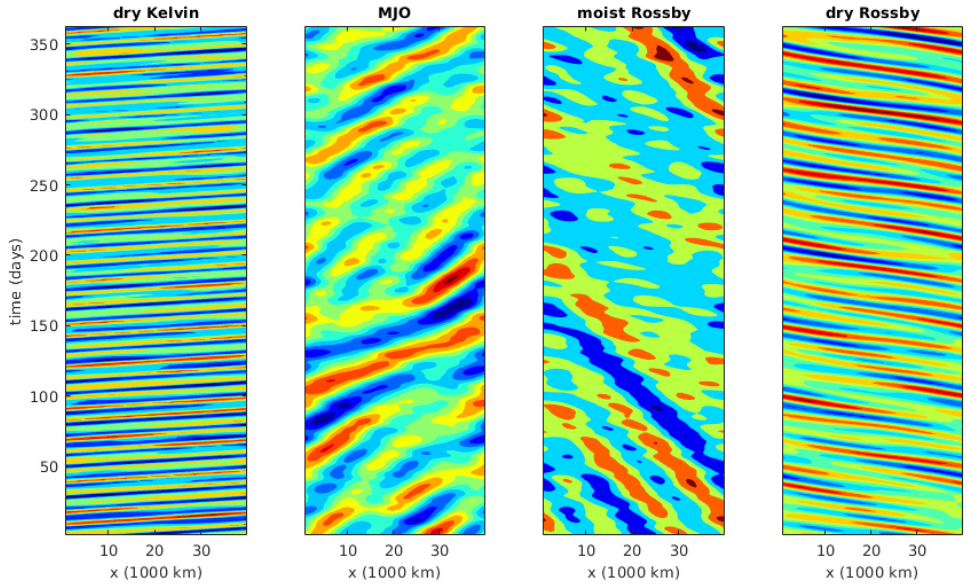

Figure 4.7: Hovmöller diagrams of the four wave indices during a 1 year nature run after the model's spin-up.

A nature run of one year after sufficient model spin-up was analyzed for the behavior of the four different wave types in the Skeleton model by calculation of the wave indices as explained in Chapter 3.3.2. Their Hovmöller diagrams (cf. Figure 4.7) show the expected typical propagation directions and phase speeds. Moreover, some variability in their strength over time can be observed with a clear correlation between the moist modes, i.e. the moist Rossby waves and the MJO. It should be noted that these results were achieved without any previous filtering for certain frequencies. This is in accordance with the good performance of the Skeleton model based MJO index for real time filtering as stated in Stechmann and Majda (2015).

4.2 Stochastic Ensemble Kalman Filter results

In the following, the results for the filtering with the stochastic EnKF are presented in two separate parts. Firstly, the derivation of the optimal localization from all available methods in physical as well as in model space, and for different ensemble sizes is presented in 4.2.1. Secondly, the different influences of observations of the different variables in the EnKF are systematically assessed in 4.2.2. Therefore, their impacts on the general filter quality and the predictability of the four wave types, as well on the conservation properties and the ensemble statistics are regarded.

4.2.1 Localization tuning

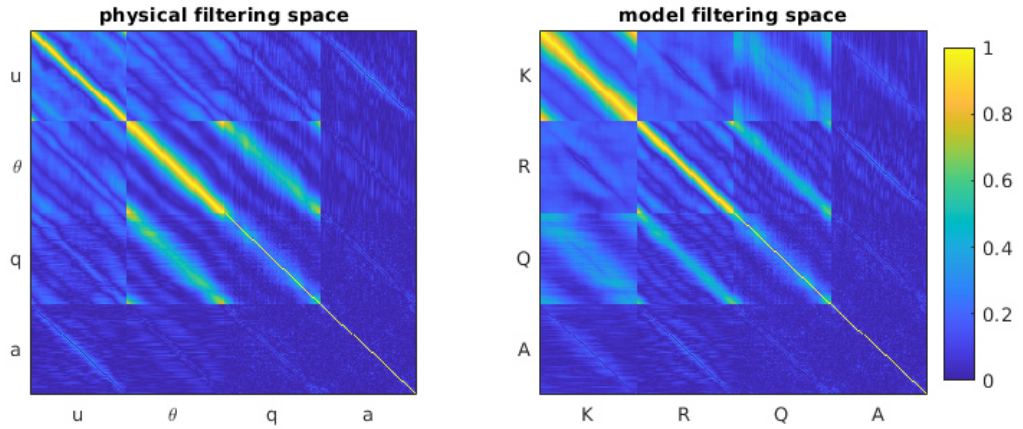

Figure 4.8: Climatology based localization matrices calculated from a 1000-member climatological ensemble in physical (left) and model (right) space.

The best localization for the stochastic EnKF was investigated experimentally from all available options that are described in Chapter 3.2.1. Therefore, first, the climatology based localization matrices in physical and model space were calculated from the covariances in the 1000-member climatological ensemble (cf. Figure 4.8). Subsequently, the different localization techniques, i.e. climatology based and/or distance dependent according to a Gaussian or Gaspari-Cohn (GC) function with variable localization radius r, were assessed. Since the localization should primarily mitigate sampling errors in the covariance estimation, this was done for a range of ensemble sizes N by repetition of the following steps for each localization option, again using the climatological 1000-member ensemble:

- selection of 100 permutations with N members from the 1000 climatological states
- calculation of the correlation matrices (scaled covariance matrices as in Figure 4.3) for each of the permutations
- localization of the correlation matrices
- computation of the relative covariance pattern errors by pointwise division of the differences between the permutations' correlation matrices from the 1000-member correlation matrix by the 1000-member correlation matrix
- averaging the absolute values of the relative covariance pattern errors over all permutations
- taking the mean of the thus gained error matrix as final error measure.

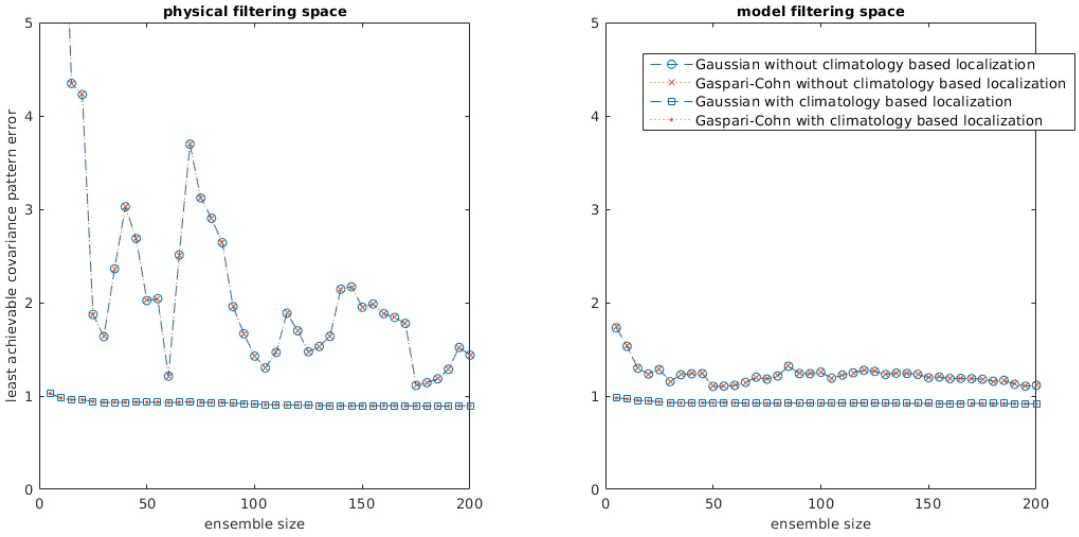

Figure 4.9: Least achievable (i.e. for the best localization radius) covariance pattern error for a range of ensemble sizes in physical (left) and model (right) space, four lines for the available localization techniques: distance dependent localization by a Gaussian or Gaspari-Cohn function with optional additional climatology based localization.

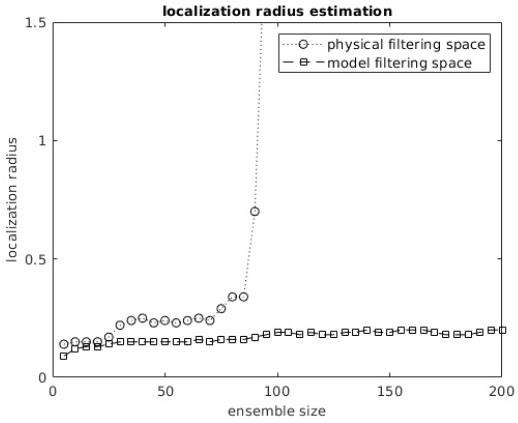

Figure 4.10: Localization radii with the smallest covariance pattern errors as function of the ensemble size, for distance dependent localization by a Gaspari-Cohn function plus climatology based localization, two lines for physical and model space.

The outcome of this procedure were scalar measures for the remaining covariance pattern errors after localization with the different techniques and for different ensemble sizes. To evaluate whether the climatology based localization should be applied, and whether it makes a difference if a Gaussian or a GC function is used for the distance dependent damping, the smallest achieved error values for these options, i.e. those for the optimal localization radii, were plotted as functions of the ensemble size (cf. Figure 4.9). The results indicate that independent of the ensemble size and both, in physical as well as in model space, the climatology based localization is useful and there is no significant difference between the localization by a Gaussian or GC function. It was therefore decided to use the combined climatology based and GC localization for the further experiments in this work. With this technique, the quality of the covariance estimation can be kept approximately constant also for small ensembles by adaption of the localization radius, and is moreover similar for the filtering in both state spaces. In

a second step, the thus selected localization was examined for the optimal localization radius, i.e. the one with smallest error value, subject to the ensemble size (cf. Figure 4.10). The graph reveals a quite different behavior depending on the state space: In physical space, the localization radius is strongly increasing with the ensemble size and there is no need for a GC localization for $N > 100$. In contrast, in model space, a tight localization with only weakly increasing localization radius with ensemble size should be applied. These findings are in good agreement with the experienced differences in filter quality of the EnKF with diverse localization radii and ensemble sizes. The localization radius in all following experiments was selected based on these results, where the standard ensemble size was chosen to be 50 members.

4.2.2 Assessment of different observational setups

The observations of different variables can vary largely in their impacts on the EnKF's quality due to their different interdependencies with other variables and gridpoints. To assess which observations are particularly helpful for the filtering of the Skeleton model and especially the MJO prediction, six experiments were run with the standard setup as described in Chapters 3.1.1, 3.1.2, 3.1.3 and 3.2.1. In each of those, only one variable, either u, θ, q, a, K or R, was observed at every fourth gridpoint and time step, i.e. with distances in space and time of approx. 2500 km and 6.64 h. In the first four experiments, the update step was performed in physical space, in the latter two in model space. An ensemble size of 50 members was chosen and the localization radius was selected according to the suggestion in Chapter 4.2.1 as 0.24 or 0.15. Additional constant inflation factors β_c were tuned for each experiment separately as 1.0004, 1.0010, 1.0005, 1 i.e. none, 1.0001 and 1.0001, respectively. The DA was run for 5 years in the model simulation, followed by 5 years of free forecast, where the underlying truth is the same in all experiments.

The results of the experiments are presented in Figure 4.11 for the RMSE and pattern correlation evolutions of the different physical and model variables and in Figure 4.12 of the wave types in the ensemble mean. For a better overview, the main interesting outcomes are listed in the following:

- If only potential temperature is observed, the filter quality is specifically bad for all other physical variables and the MJO. This is in good correspondence with the finding that the MJO signal is least expressed in the power spectrum of potential temperature (cf. Figure 2.5).
- DA with observations of zonal wind or moisture shows the best overall results and is beneficial throughout all variables and wave modes, also the MJO.
- Observations of convective activity are beneficial for the filtering of moisture, but not sufficient to prevent the EnKF's divergence in the dry dynamic variables. This can be explained by the small covariances between convective activity and the other variables. However, it is possible to filter all wave types, also the MJO, with only convective activity observations, which nonetheless stresses their importance.
- The filtering skill that is achieved for the moisture and convective activity is often worse than for the dry dynamic variables. This can be explained by their smaller scale structure, and for convective activity also by its non-Gaussianity.
- The dry waves can in general be better filtered than the moist waves. However, they are in most cases not predictable over long time, presumably due to their fast propagation.
- Observations of K are not beneficial for filtering the physical variables and lead to a small predictability of the moist wave types. It is more useful to observe R. A probable reason for this is the very fast oscillation of the Kelvin wave.
- Observations of K are correlated with a good filtering skill for dry Kelvin waves and observations of R with a good filtering skill for especially dry, but also moist Rossby waves. This shows the importance of their corresponding unforced structures for these wave types.

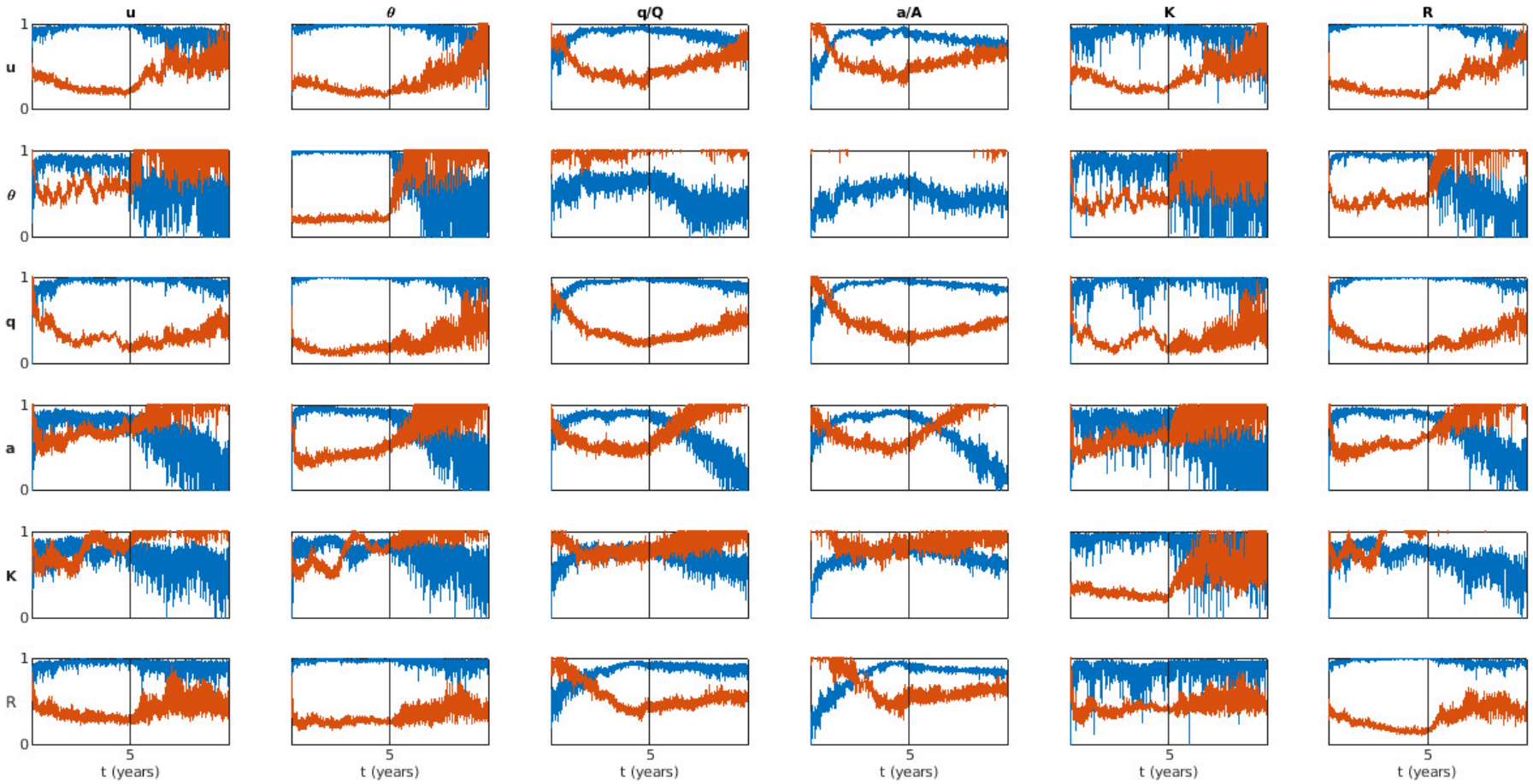

Figure 4.11: Six experiments with observations of different variables as indicated in the separate rows, DA at every fourth gridpoint and time step, 5 years of filtering, subsequently 5 years of free forecast, the columns show for the different physical and model variables in the Skeleton model the RMSEs (red) and pattern correlations (blue).

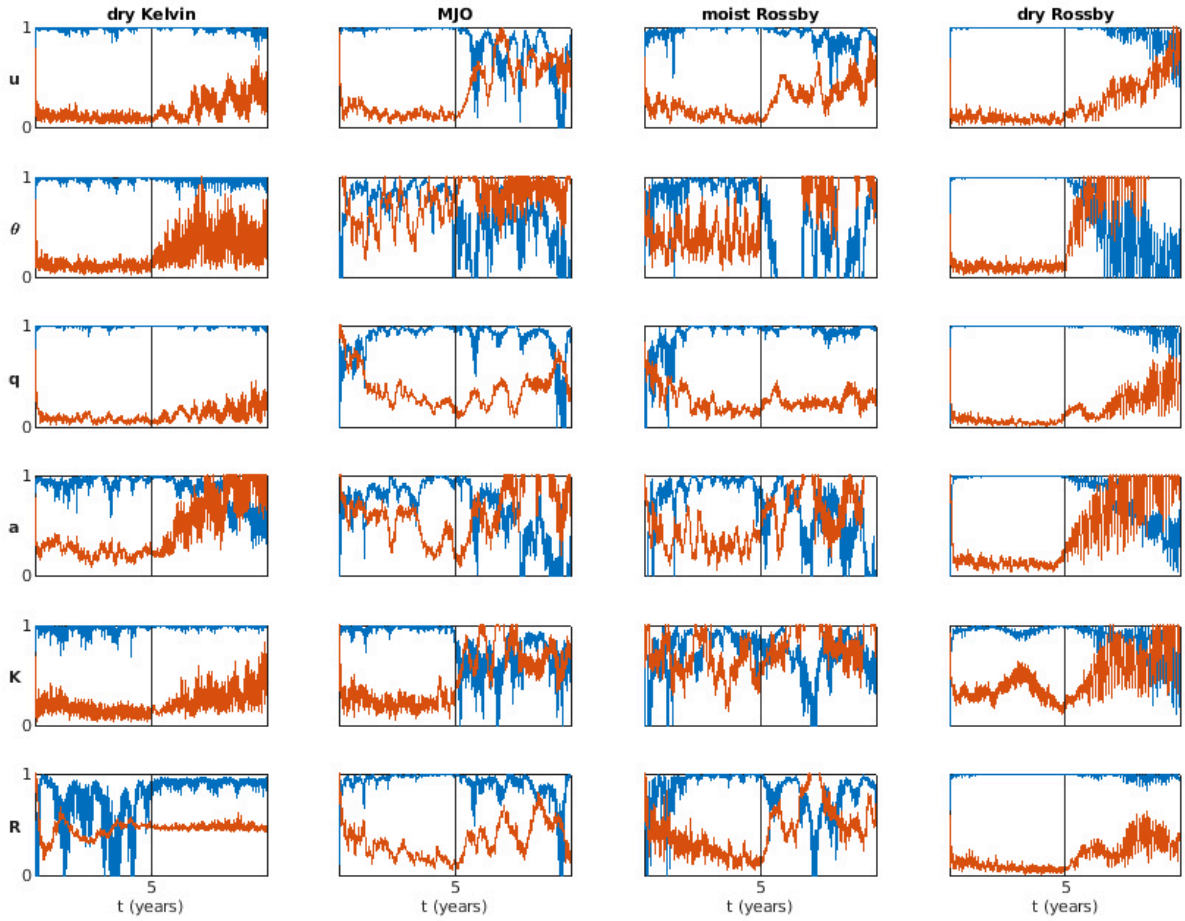

Figure 4.12: Six experiments with observations of different variables as indicated in the separate rows, DA at every fourth gridpoint and time step, 5 years of filtering, subsequently 5 years of free forecast, the columns show for the different wave types in the Skeleton model the RMSEs (red) and pattern correlations (blue).

In addition to the above presented error evolutions, Figures 4.13 and 4.14 furthermore show the DA's influences on the ensemble statistics, here especially the skewness and the ensemble spread, and the model's physical and algorithmic conservation properties as well as the dry mass in the ensemble mean. With respect to this, in particular the following can be remarked:

- The skewness of convective activity was reduced, but stayed slightly positive on average throughout the DA in all experiments. It could be best maintained during filtering with the log-normally distributed observations of convective activity.
- The relative ensemble spread could be maintained within in the interval [0.5,1.5] throughout all experiments. This is above the ensemble spread that is approached without inflation. The adaptive inflation factor decreased over time in all experiments as is theoretically expected.
- Stronger inflation was needed in the experiments with observed dry dynamic variables, i.e. u, θ, K, and R.
- All conservation properties are affected by the DA in all experiments. However, some differences can be observed. Especially zonal wind observations, but also observations of R are beneficial for $C1$. Potential temperature observations lead to an oscillation around the correct mean for ME and $C2$, though with large amplitude. DM, the only neither physical nor algorithmic conservation property, is least affected by DA, its oscillation stays within the climatological

range.

- All linear conservation properties are approximately conserved during the free forecast. However, their value depends on the initial condition, i.e. the analysis produced by the last DA update. Even in case of a oscillation around the correct mean during DA, this can lead to a quite erroneous value during the forecast.
- TE and $C3$ of the ensemble mean both show a negative drift during the free forecast. This is due to the relaxation to a climatological distribution of the states. As these are nonlinear, convex functions, the climatological mean, for which u, θ, and q or K, R, and Q are close to zero throughout all gridpoints, has smaller TE or $C3$ than the mean value of climatologically distributed states.

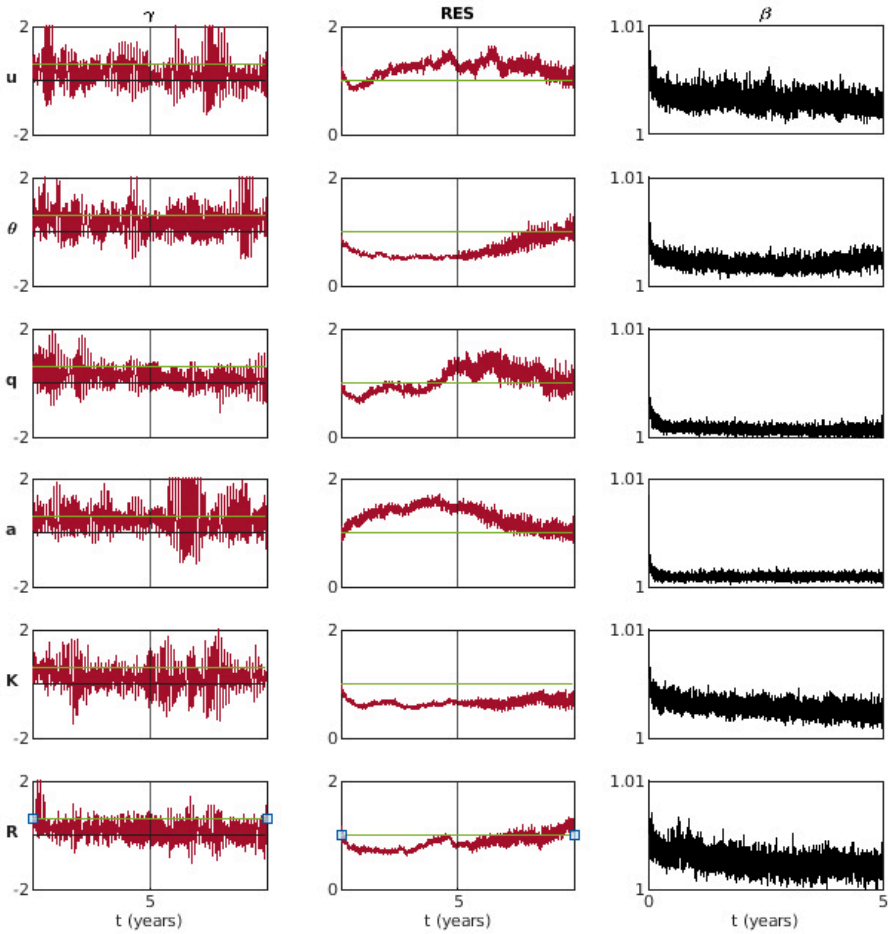

Figure 4.13: Six experiments with sparse observations of different variables as indicated in the separate rows, DA at every fourth gridpoint and time step, 5 years of filtering, subsequently 5 years of free forecast, the columns show the influences on the ensemble properties, i.e. the skewness in convective activity at the gridpoint with the highest climatological skewness (left, green line: climatological skewness) and the relative ensemble spread (middle, green line: optimal relative ensemble spread, i.e. 1), the evolution of the inflation factor during the filtering is plotted on the right.

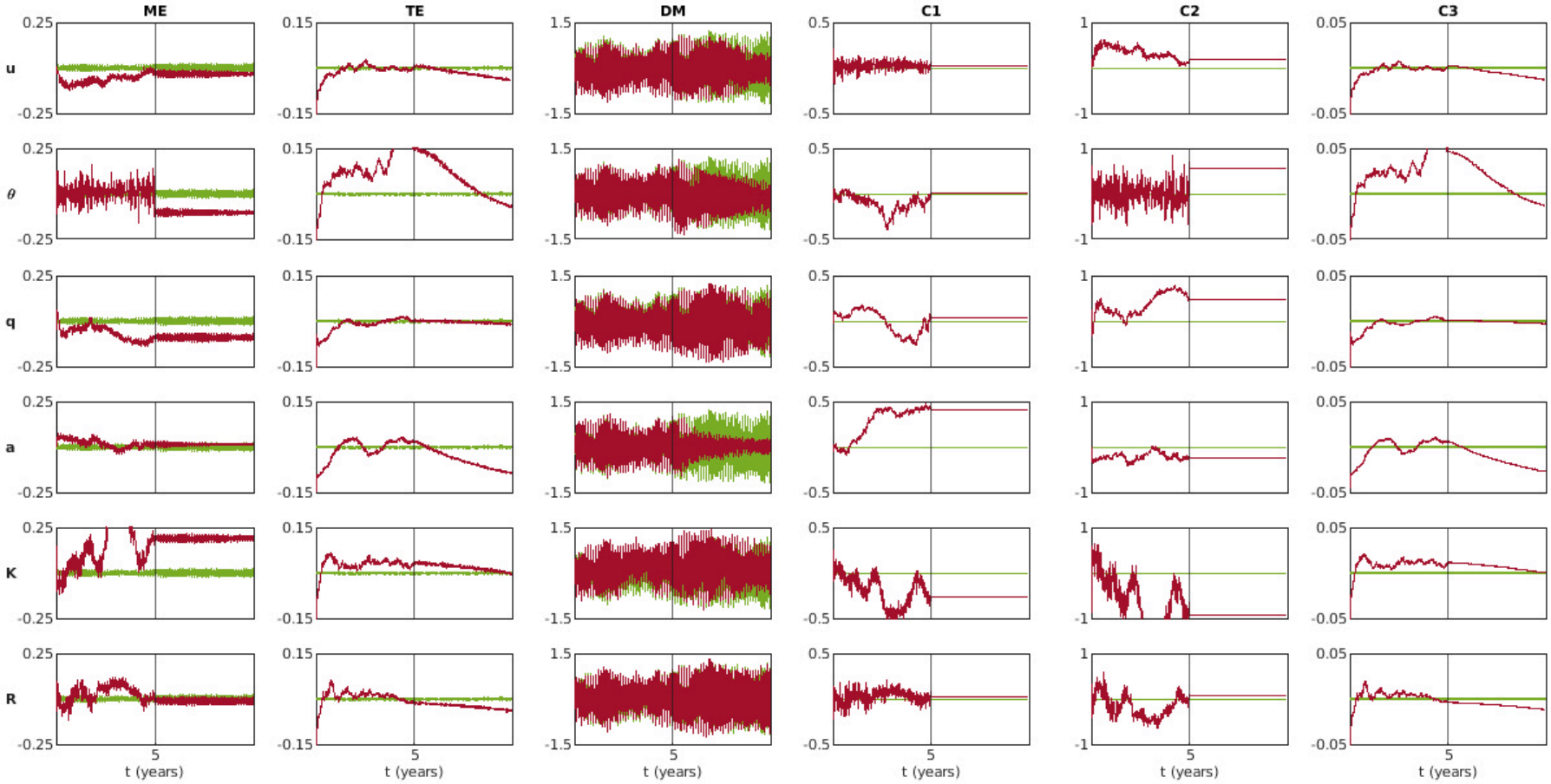

Figure 4.14: Six experiments with observations of different variables as indicated in the separate rows, DA at every fourth gridpoint and time step, 5 years of filtering, subsequently 5 years of free forecast, the columns show the influences on the physical and algorithmic conservation properties (green: truth, red: ensemble mean).

Finally, it should be mentioned that experiments with observations of Q and A, i.e. observations of the moisture variables with DA in model space, were attempted, but lead to a very fast filter divergence. They were thus not included. The reason for this could be that the dry dynamic structures K and R in model space are propagating faster and are thus more difficult to filter than u and θ in physical space. This problem of an especially difficult filtering of K in the Skeleton model has been detected earlier – although with a different filter setup – also by Chen and Majda (2016).

4.3 Impacts of analysis constraints

This section presents the results for the QPEns with the different implemented analysis constraints. In 4.3.1, experiments with observations of zonal wind and convective activity, i.e. typical variables for the assessment of the MJO, are conducted with the QPEns. The filtering skill for the physical and model variables, and the wave modes is analysed and compared to the stochastic EnKF. Furthermore, the results of the linearized soft total energy constraint are compared to those with the exact constraint. Thereafter, the influence of the total energy constraint is investigated in more detail as it showed a positive impact throughout all results in 4.3.1. It is evaluated how it improves the treatment of non-Gaussianity over a simple cut or constraint of convective activity to positive values. Therefore, experiments are run in a test case with small mean convective activity, i.e. with frequently occurring values close to zero, in 4.3.2.

4.3.1 General influences on the filter quality and MJO prediction

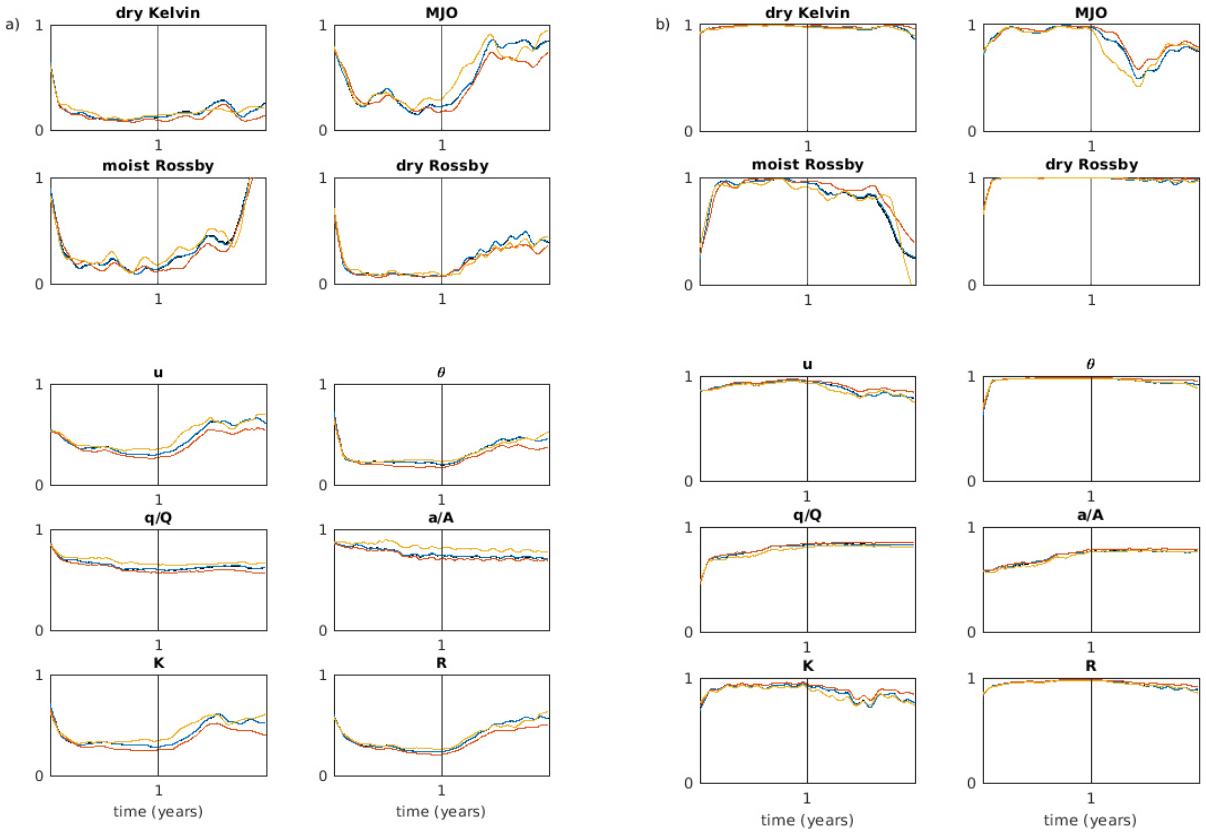

Figure 4.15: a) RMSEs and b) pattern correlations for the wave types and the variables in physical and model space, DA with observations of u and a at every fourth gridpoint and time step, 1 year of filtering, subsequently 1 year of free forecast, same perturbed observations used for all experiments, results smoothed by the MATLAB function 'lowess' for locally weighted linear regression with a span of 60 days, black: stochastic EnKF, blue: QPEns with moist static energy constraint, red: QPEns with total energy constraint, yellow: QPEns with dry mass constraint, the black and blue line are very close to each other and difficult to distinguish.

The experiments for the assessment of the different analysis constraints in the QPEns, which are described in Chapter 3.2.2, were performed with sparse observations of u and a, both at every fourth

gridpoint and time step. This setup was chosen in analogy to Chen and Majda (2016), who tested a nonlinear filter for the Skeleton model. They argued that full observations of convective activity and optional sparse observations of zonal wind best reflect the data from satellites and weather stations that is operationally used to track the MJO. However, in the following, convective activity is also sparsely observed in order to maintain more uncertainty and a wider ensemble spread in it. This was not necessary in their work as they used another model version which stochastically propagates the convective activity. For the same reason, the DA was in the following experiments only run for one year with a subsequent forecast time of equally one year. Furthermore, the ensemble was again chosen to consist of 50 members and the additional constant inflation factor β_c was tuned to 1.0001. The set of perturbed observations was only generated once during the first experiment and then reused in the following ones, which was possible as the underlying truth was always the same. With these conditions, perfect comparability was ensured.

Figure 4.15 shows the results of the experiments with analysis constraints of the different physical balances, i.e. the constraints of moist static energy (ME), total energy (TE) or dry mass (DM) to the respective value of the truth. They were compared to the unconstrained stochastic EnKF by the RMSEs and pattern correlations of the four wave types, and the physical and model variables in the ensemble mean. For a better visibility of differences, all curves were smoothed by the MATLAB function 'lowess' for locally weighted linear regression with a span of 60 days. The moist static energy constraint was found to improve the filtering skill only very slightly, such that the lines for the EnKF and the QPEns with moist static energy constraint are hardly distinguishable in the graphs. In contrast, the dry mass constraint lead to significant deviations of the estimated states from the EnKF, but did not show a clearly advantageous behavior. A significant positive impact throughout all results was however observed for the total energy constraint.

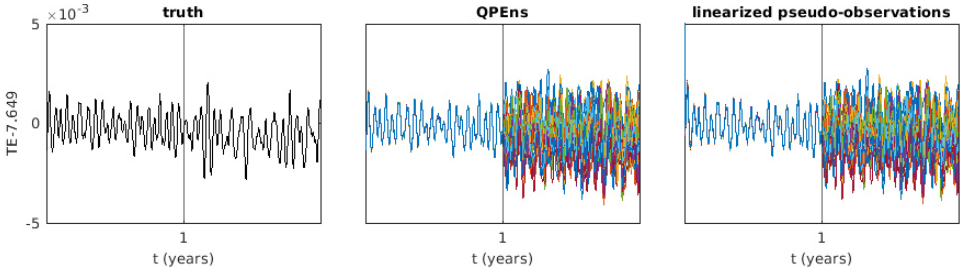

Figure 4.16: Total energy in the truth (left), the members of the QPEns with total energy constraint (middle), and the ensemble members with pseudo-observations/soft constraint of the linearized total energy (right), 1 year of filtering, subsequently 1 year of free forecast.

Since the total energy is a nonlinear function of the state variables, the QPEns with total energy constraint requires nonlinear optimizations. This leads to a considerable increase in computational demand, which is not of relevance in this work's toy model setting but would be an important obstacle for its operational realization. Therefore, the computationally inexpensive alternative of a soft constraint, i.e. pseudo-observations, was furthermore investigated in comparison to the exact constraint. This was set up as explained in Chapter 3.2.3 with the total energy calculated from its linearization around the respective background ensemble states. It was found that the accuracy of the total energy in the ensemble members that could be achieved with the soft constraint was comparable to that of the MATLAB minimization with default tolerances and stopping criteria (cf. Figure 4.16). The result for the filtering skill of the MJO was thus also indistinguishable from that of the QPEns (cf. Figure 4.17).

Figure 4.17 shows the same lines for the stochastic EnKF and the QPEns with total energy constraint as the subplot concerning the MJO's RMSE in Figure 4.15, but enlarged and without smoothing. The result of the improvement in MJO predictability through the analysis ensemble members' constraint to the truth's total energy is thus more clearly visible. It is especially noticeable, that the difference in the filters' skills develops mostly during the free forecast, whereas the RMSE after the one year of DA is approximately comparable.

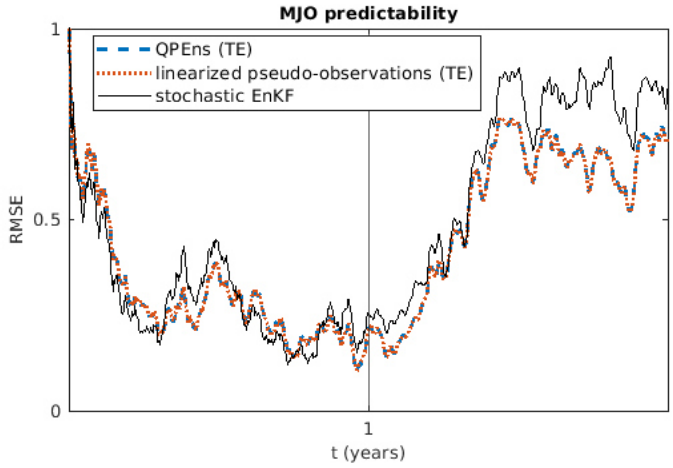

Figure 4.17: RMSE of the MJO during experiments as in Figure 4.15 with the stochastic EnKF, the QPEns with total energy constraint and the stochastic EnKF with additional pseudo-observations/soft constraint of the linearized total energy.

4.3.2 Test case with small mean convective activity

The reason for the beneficial impact of the total energy constraint on the DA was evaluated via three experiments with an increased warmpool strength of $\alpha = 0.9$ (see Equation 2.35). This leads to a smaller background forcing and thus smaller mean convective activity values outside of the warmpool, i.e. overall more frequent values of convective activity close to zero. Negative values in the EnKF's analysis for convective activity are thus more likely. Those are truncated to values slightly above zero as explained in Chapter 3.2.1 to prevent errors in the subsequent propagation. With this setup, three years of filtering were run with different DA systems. First, the stochastic EnKF was applied with the above described cut of negative convective activity values. Second, the QPEns was used with the boundary constraint of convective activity to positive values. Third, the QPEns was used with the total energy constraint, which automatically constrains convective activity to positive values as its equation contains its natural logarithm.

The results of these experiments are shown in Figure 4.18. Both, the cut and the constraint of convective activity to positive values, can not prevent the filter from diverging. More ensemble members reach convective activity values very close to zero at more gridpoints over time and the ensemble spread increases unrealistically due to the thus wrongly estimated PDF. In contrast, the total energy constraint successfully maintains a plausible PDF for convective activity throughout all gridpoints and achieves a good filtering skill.

An improved treatment of the non-Gaussianity in the Skeleton model is thus the reason for the beneficial impact of the total energy constraint in DA. Convective activity shows only small climatological covariances with the other variables and between gridpoints. However, a strong nonlinear relation

between all variables, that moreover incorporates the positivity of convective activity, is given by the total energy. If use of this is made in DA, it can significantly improve the forecast quality.

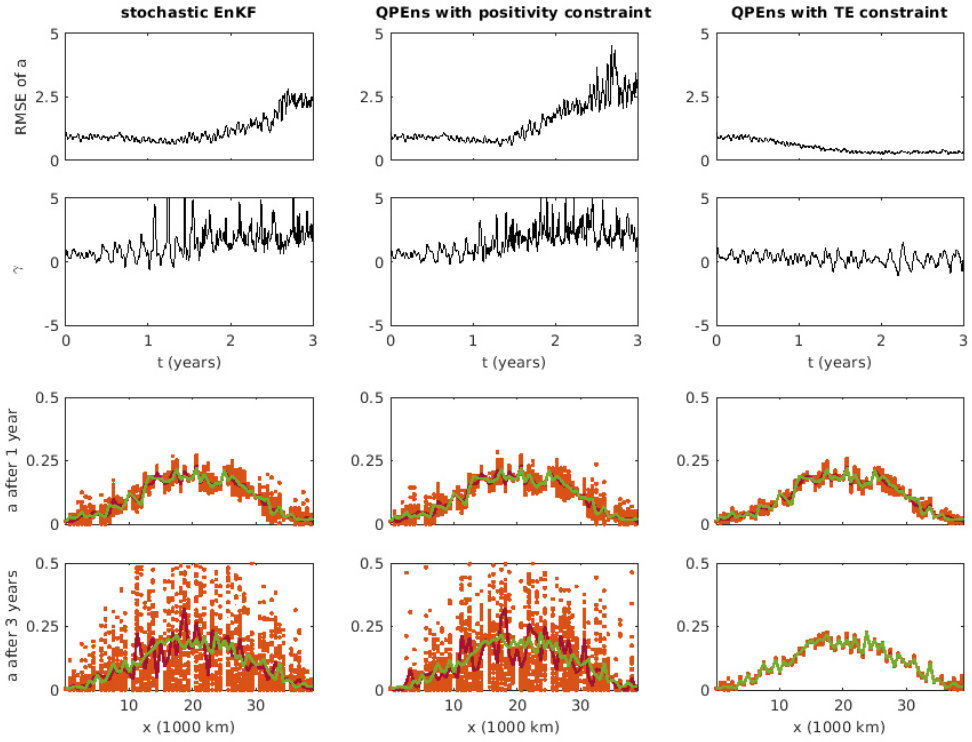

Figure 4.18: Comparison of three experiments with the settings described in Chapter 4.3.1 except for a smaller background warmpool with $\alpha = 0.9$ and three years of only filtering, results for the stochastic EnKF (left), the QPEns with a constraint of convective activity to positive values (middle) and the QPEns with total energy constraint (right), the different rows show 1. the time evolution of the RMSE in convective activity, 2. the time evolution of the ensemble's skewness in convective activity at the gridpoint with the highest climatological skewness, 3. the spatial convective activity distribution of the ensemble members (orange), the ensemble mean (red) and the truth (green) after 1 year and 4. the same after 3 years.

5 Discussion

The above presented results allow for several conclusions with respect to possible improvements in DA for MJO prediction. They are all based on identical twin experiments with the Skeleton model as described in Chapter 3.

Firstly, a stochastic EnKF was set up and tuned by covariance localization and adaptive multiplicative inflation. Thereby, it could in particular be demonstrated that the consideration of climatological covariances beyond pure isotropy in the construction of the localization matrix is beneficial when filtering the Skeleton model. This emphasizes the nature of the MJO as planetary scale phenomenon that comes with specific large scale interdependencies in the atmosphere. Those are important to respect in the initial conditions for MJO forecasts.

Thereafter, experiments with different observational setups showed significant variations in the behavior of the stochastic EnKF. They indicate that especially a good representation of the lower tropospheric moisture, but also the zonal wind variable lead to an improved filtering skill and predictability of all variables and all wave types. This is in accordance with earlier studies by Stechmann and Majda (2015) and Chen and Majda (2016), who both stated the important role of humidity for the MJO signal in the Skeleton model. Chen and Majda (2016) moreover showed a positive impact of zonal wind observations on the overall filtering skill of a nonlinear filter applied to the Skeleton model. In contrast, potential temperature was found to be the least important variable for the prediction of the MJO. Its observations proved to be only useful for the filtering of the dry dynamics, thus the fast wave types, which are however subject to comparably rapid error growth in the forecast. This subordinate role of temperature or mass (as θ is interchangeable with ρ, i.e. density anomalies, in this model) information for the MJO evolution is consistent with the weak MJO signature in the power spectrum of potential temperature during a nature model run. Furthermore, the relevance of convective activity for DA with the EnKF was assessed. As it is only weakly coupled to the dry dynamic variables via covariances, its observation was insufficient for their filtering with the EnKF. However, it proved to be beneficial for the filtering of moisture and of all wave types, even those with only small coupling to convective activity. This emphasizes its nevertheless important role in the Skeleton model. In addition to these experiments with observations of the physical variables, the significance of information on the dry Kelvin and first meridional Rossby wave structures was evaluated. It was shown that both are important for the evolution of the MJO. Yet, capturing the slower propagating Rossby wave structure had a stronger positive impact, and was moreover also useful to filter the physical dry dynamic variables.

Besides the determination of beneficial localization and observations for the EnKF, this work was aimed at the improvement of DA for MJO prediction beyond the EnKF. The motivation for this was given by the fact that the neglected non-Gaussianity in the probability distribution of convective activity was suspected to be a major error source. This was emphasized by the observation of a significant reduction of skewness in the ensemble's convective activity distribution throughout DA with the EnKF. Moreover, it is for the same reason that a nonlinear filter for the Skeleton model was set up successfully in earlier work by Chen and Majda (2016). In this thesis, however, a different approach was chosen. Additional constraints of the analysis ensemble members to the truth's values of certain physical balances were imposed on the otherwise unchanged cost function minimizations in the stochastic EnKF. This returns the QPEns as algorithm, which consists of an ensemble of numerical optimization problems in the update step. First proposed by Janjić et al. (2014), such constraints have previously been shown to have the potential to help maintaining physically plausible states and thus more realistic probability distributions throughout DA (see Janjić et al., 2014; Zeng et al., 2017;

Ruckstuhl and Janjić, 2018). As the Skeleton model furthermore incorporates two energy conservation principles that were found to be violated by DA with the EnKF, there was a strong indication for a potential benefit through analysis constraints.

The analysis constraints that were primarily evaluated in this work with a QPEns are the Skeleton model's balances of moist static and total energy, as well as a constraint of the dry mass. Although the latter is not exactly conserved in the model, it is conserved in its long time average, it is an important physical balance for many NWP models, and it has moreover shown an advantageous influence in earlier work (see Janjić et al., 2014; Ruckstuhl and Janjić, 2018), though in combination with another model. With a set of experiments, it was demonstrated that the constraint of moist static energy has a very small positive impact, whereas the constraint of dry mass influences the filter significantly, but neither clearly positive nor negative. This is in conformity with the finding that potential temperature largely influences both of these properties, but is the least important variable for the EnKF. Furthermore, the dry mass is not much affected in the EnKF but stays within its climatological order of magnitude. In contrast, the constraint of total energy was found to lead to an improvement in the filtering skill with respect to the EnKF for all variables and wave types. Interestingly, the error difference developed mostly during the free forecast, which strengthens the importance of correct total energy in the initial conditions for MJO prediction. The reason for this was demonstrated in subsequent experiments with a small convective activity background in some regions of the zonal domain. In this test case, negative convective activity values occurred frequently in the analysis of the EnKF. A truncation of such values to slightly positive values or a positivity boundary constraint in the QPEns both lead to an increasingly skewed probability distribution of convective activity as more ensemble members at more gridpoints approached small values. Whereas those methods were thus not capable to prevent filter divergence, the total energy constraint successfully solved this problem. This shows how the total energy relation, which involves all variables and an automatic positivity constraint for convective activity, improves the treatment of non-Gaussianity. It complements the small covariances between convective activity and the other variables by an additional nonlinear relationship, and thereby yields physically more realistic states in the analysis ensemble, especially in the non-Gaussian variable of convective activity.

To summarize, the results of this thesis emphasize the importance to respect planetary scale correlations and to capture the zonal wind and humidity distribution in DA for MJO prediction. Furthermore, they indicate a largely beneficial impact of correct total energy in the initial conditions, whose constraint can compensate for the neglect of non-Gaussian convective activity statistics in the EnKF.

However, the meaningfulness and applicability of these findings should be subject to critical discussion. Primarily, it should be noted that the setup used for the experiments in this work is very simplified with respect to operational NWP systems. Not only is the Skeleton model a toy model which incorporates various assumptions, approximations, and a strong truncation, but also the DA systems were implemented with idealized processing of the observations and tuning, and with perfect model propagations. Therefore, neither the evolution of the MJO nor the DA algorithms accurately reproduce real world conditions or operations. Nevertheless, the Skeleton model depicts some fundamental characteristics of the MJO in such quality that incorporating its dynamics into more detailed models was already suggested (see Stachnik et al., 2015). In the same manner, the results of this thesis could be used as hints for possible improvements in DA that are to be verified in more sophisticated setups. First steps in that direction could be done with the use of more realistic observations, comparable to those synthesized for the Skeleton model from real data by Ogrosky and Stechmann (2015). This would require a refinement of the DA system, e.g. for the inclusion of some model error. Alternatively

or in addition, the large variety of more elaborated versions of the Skeleton model, which all include different additional realistic features, could be used for further experiments. By this, the robustness of the results could be tested. Available model modifications or versions are in particular:

- A different initialization (see Majda and Stechmann, 2011) or more realistic background forcing (see Ogrosky and Stechmann, 2015) for the fully truncated nonlinear deterministic version as used in this work.
- The stochastic nonlinear Skeleton model (see Thual et al., 2014): The idea behind this model version is to parameterize synoptic scale processes, that are responsible for the irregularity and low predictability of MJO events, with more realism while keeping the model's simple design. Therefore, the nonlinear interaction that governs the evolution of convective activity is replaced by a Markov birth-death process, whose transition rates are chosen such that the deterministic dynamics are conserved on average: $\frac{\partial E(a)}{\partial t} = \Gamma E(qa)$ (5.1). It was shown that simulations with this model version arrive at capturing some main statistical characteristics of MJO irregularity, especially their occurrence in wavetrains of consecutive MJO events (Stachnik et al., 2015).
- The nonlinear deterministic model with refined meridional structure, i.e. choosing a higher truncation number $M > 0$ (see Thual et al., 2015): This is especially useful when it comes to investigating seasonal effects. Experiments with a seasonally varying warmpool background showed a realistic seasonal modulation of intraseasonal variability with meridionally asymmetric intraseasonal events.
- Several versions with different refined vertical structures (see Thual and Majda, 2016a,b): These model versions differ from each other in their details, but they all show improvements in the representation of the refined vertical MJO structure.

The meridionally and vertically extended versions all incorporate a total energy balance. However, the total energy conservation is violated if $s^\theta \neq s^q$ and is also affected by the stochasticity in the stochastic Skeleton model. This should be respected when further investigating the total energy constraint.

Besides the issue of the result's verification, their applicability in operational forecasting routines needs to be discussed. In particular, the implementation of the QPEns with a nonlinear analysis constraint, such as the total energy, is subject to two major difficulties (see also Zeng et al., 2017). First, in contrast to the identical twin experiments in this thesis, the truth's exact value is not known under real world conditions. It thus has to be estimated in an additional process. And second, the nonlinear optimizations increase the computational demand for the DA's update step significantly with respect to an EnKF in a large state space. The latter problem is already addressed by current research on algorithmic improvements in numerical minimizations, such as parallelizations or exploiting matrix sparsities (Zeng et al., 2017). Nevertheless, as an alternative to the costly QPEns, soft constraints via pseudo-observations were tested in this thesis. Therefore, the total energy constraint was linearized around the respective current background states. Despite this linearization and a necessary nonzero constraint tolerance, this method proved sufficiently accurate in this work's toy model setup. It could thus be a considerable option, at least for first tests of analysis constraints, also in operational NWP.

6 Summary and outlook

This thesis was aimed at the identification of possible improvements in DA for MJO prediction. For this purpose, a toy model setup was used since experiments with modern, high level GCMs on intraseasonal timescales would have exceeded a practicable computational demand. The selected model was the 'Skeleton Model for Tropical Intraseasonal Variability', which depicts the main characteristics of large scale MJO dynamics through an easy to understand and efficient algorithm. It was employed in its nonlinear deterministic version with highest possible truncation in vertical and meridional direction as introduced by Majda and Stechmann (2011). With the Skeleton model, different DA systems were tested in identical twin experiments.

As a basis, a stochastic EnKF was implemented and tuned by covariance localization and adaptive multiplicative inflation. This configuration was used to assess the influences of different observations on the prediction of the model variables and wave types, i.e. also the MJO. However, the significant non-Gaussianity in the variable of convective activity could not be respected by the EnKF. To address this problem, the filter was subsequently extended to a QPEns. This means that additional constraints of the analysis ensemble members to the truth's value of certain properties were imposed, thus transforming the update step into a numerical optimization problem. Such approach, which was first proposed by Janjić et al. (2014), had proved beneficial for handling non-Gaussian probability distributions in earlier DA toy model studies. Moreover, it appeared especially reasonable in this work due to two energy conservation principles in the Skeleton model's underlying equations. Analysis constraints of those, i.e. the moist static and total energy, as well as of the dry mass and a pure positivity constraint for convective activity were evaluated for their impact of the filter's ability to capture the different variables and wave types.

The outcomes of the experiments in this thesis stress the relevance of planetary scale interdependencies for the MJO. In accordance with earlier work, they furthermore indicate that a good representation of zonal wind and humidity is important to capture its structure in the Skeleton model. Beyond this, they yield the new result that – in contrast to moist static energy and dry mass constraints – the total energy constraint significantly improves the filtering of the strictly positive convective activity. Thereby, it positively influences also the forecast of the other variables and all wave types, in particular also the MJO. In case of small background forcing, it can even prevent filter divergence, that otherwise occurs due to the neglect or rudimentary treatment of non-Gaussianity.

Future work building on this thesis should be targeted at the verification and refinement of the above results in more sophisticated setups with respect to both, the model and the DA system. Possibilities for this could lie in the several available extensions of the Skeleton model, e.g. for a more detailed meridional or vertical structure, and/or in the use of real observational data together with the introduction of model error in DA. In case of a too high computational demand of the QPEns with the nonlinear total energy constraint in more complex configurations, alternatively a linearized soft constraint, i.e. pseudo-observations, could be used. This proved comparably beneficial in this work.

Beyond testing this work's outcomes for their robustness, future research could also be directed towards using the now existing toy model DA setup for further purposes. Due to its inexpensiveness, it could in particular serve as a test field for algorithmic improvements with respect to efficiency, e.g. in the QPEns' numerical optimization. Modifications such as replacements of operations by neural networks, iterative linearizations of nonlinear constraints, or optimized sparse matrix representations could easily be tried out. Thereby, it could help to make such complex algorithms available for operational NWP.

Finally, a sophisticated DA routine tailored for MJO prediction – as it will hopefully be achieved with such further steps – could be employed to examine the influence of MJO predictability on forecasting a range of interconnected weather and climate phenomena. For example with respect to MJO-ENSO interrelations, a coupled atmosphere-ocean toy model has recently been developed by Thual et al. (2018). Based on a modification of the Skeleton model for the atmospheric part, this model is called 'Tropical Stochastic Skeleton-General Circulation Model' (TSS-GCM). In addition to the main characteristics of the MJO, it qualitatively captures important features of the structure, period, and statistics of ENSO and its interactions with the MJO, i.e. the major components of intraseasonal to interannual variability in the tropics. Thus, if one was to apply a DA system that was optimized for MJO dynamics to its atmospheric part, conclusions could be drawn regarding ENSO predictability.

In this sense, due to its multiple links to other atmospheric disturbances reaching as far as into the extratropics, improving MJO predictability in NWP stays a key issue with large societal impact.

Bibliography

2nd phase of W2W, SFB/TRR165 (2019-2023): Waves to Weather, Phase 2, Research Area B, Project B6. URL `https://www.wavestoweather.de/research_areas/phase2/b6/`. Accessed 26 January 2021.

Anderson, J. (2009): Spatially and Temporally Varying Adaptive Covariance Inflation for Ensemble Filters. *Tellus A*, **61** (1), 72–83.

Bechtold, P. (2019): Challenges in Tropical Numerical Weather Prediction at ECMWF. In: *Current Trends in the Representation of Physical Processes in Weather and Climate Models*, edited by D. A. Randall, J. Srinivasan, R. S. Nanjundiah and P. Mukhopadhyay, Springer Singapore, Singapore, pp. 29–50.

Bocquet, M., Pires, C. A. and Wu, L. (2010): Beyond Gaussian Statistical Modeling in Geophysical Data Assimilation. *Monthly Weather Review*, **138** (8), 2997–3023.

Burgers, G., van Leeuwen, P. J. and Evensen, G. (1998): Analysis Scheme in the Ensemble Kalman Filter. *Monthly Weather Review*, **126** (6), 1719–1724.

Castanheira, J. M. and Marques, C. A. F. (2020): The Dynamical Composition of the Madden-Julian Oscillation. *presentation at the EGU general assembly on May 6 2020, speakers from the CESAM - Department of Physics at the University of Aveiro in Portugal.*

Chen, N. and Majda, A. J. (2016): Filtering the Stochastic Skeleton Model for the Madden-Julian Oscillation. *Monthly Weather Review*, **144** (2), 501–527.

Evensen, G. (1994): Sequential Data Assimilation with a Nonlinear Quasi-Geostrophic Model Using Monte Carlo Methods to Forecast Error Statistics. *Journal of Geophysical Research: Oceans*, **99** (C5), 10143–10162.

Evensen, G. (2003): The Ensemble Kalman Filter: Theoretical Formulation and Practical Implementation. *Ocean Dynamics*, **53** (4), 343–367.

Gaspari, G. and Cohn, S. E. (1999): Construction of Correlation Functions in Two and Three Dimensions. *Quarterly Journal of the Royal Meteorological Society*, **125** (554), 723–757.

Gill, A. E. (1980): Some Simple Solutions for Heat-Induced Tropical Circulation. *Quarterly Journal of the Royal Meteorological Society*, **106** (449), 447–462.

Hamill, T. M. (2006): Ensemble-Based Atmospheric Data Assimilation. In: *Predictability of Weather and Climate*, edited by T. Palmer and R. Hagedorn, Cambridge University Press, Cambridge, pp. 124–156.

Holton, J. R. and Hakim, G. J. (2013): *An Introduction to Dynamic Meteorology*. Academic Press, Boston, 5th edition.

Houtekamer, P. L. and Mitchell, H. L. (2001): A Sequential Ensemble Kalman Filter for Atmospheric Data Assimilation. *Monthly Weather Review*, **129** (1), 123–137.

Houtekamer, P. L. and Zhang, F. (2016): Review of the Ensemble Kalman Filter for Atmospheric Data Assimilation. *Monthly Weather Review*, **144** (12), 4489–4532.

Janjic, T., Sommer, M. and Craig, G. (2017): *Atmospheric Data Assimilation*. lecture script, lecture repeatedly held at Ludwig-Maximilians-Universität München.

Janjić, T., McLaughlin, D., Cohn, S. E. and Verlaan, M. (2014): Conservation of Mass and Preservation of Positivity with Ensemble-Type Kalman Filter Algorithms. *Monthly Weather Review*, **142** (2), 755–773.

Joanes, D. N. and Gill, C. A. (1998): Comparing Measures of Sample Skewness and Kurtosis. *Journal of the Royal Statistical Society. Series D (The Statistician)*, **47** (1), 183–189.

Kepert, J. D. (2009): Covariance Localisation and Balance in an Ensemble Kalman Filter. *Quarterly Journal of the Royal Meteorological Society*, **135** (642), 1157–1176.

Khouider, B. and Majda, A. J. (2006): A Simple Multicloud Parameterization for Convectively Coupled Tropical Waves. Part I: Linear Analysis. *Journal of the Atmospheric Sciences*, **63** (4), 1308–1323.

Khouider, B. and Majda, A. J. (2007): A Simple Multicloud Parameterization for Convectively Coupled Tropical Waves. Part II: Nonlinear Simulations. *Journal of the Atmospheric Sciences*, **64** (2), 381–400.

Khouider, B., Majda, A. J. and Stechmann, S. N. (2013): Climate Science in the Tropics: Waves, Vortices and PDEs. *Nonlinearity*, **26** (1), R1–R68.

Kiladis, G. N., Wheeler, M. C., Haertel, P. T., Straub, K. H. and Roundy, P. E. (2009): Convectively Coupled Equatorial Waves. *Reviews of Geophysics*, **47** (2), RG2003.

Kim, D., Sperber, K., Stern, W., Waliser, D., Kang, I.-S., Maloney, E., Wang, W., Weickmann, K., Benedict, J., Khairoutdinov, M., Lee, M.-I., Neale, R., Suarez, M., Thayer-Calder, K. and Zhang, G. (2009): Application of MJO Simulation Diagnostics to Climate Models. *Journal of Climate*, **22** (23), 6413–6436.

Kondo, K. and Miyoshi, T. (2019): Non-Gaussian Statistics in Global Atmospheric Dynamics: a Study with a 10240-Member Ensemble Kalman Filter Using an Intermediate Atmospheric General Circulation Model. *Nonlinear Processes in Geophysics*, **26** (3), 211–225.

Laing, A. and Evans, J.-L. (2011): *Introduction to Tropical Meteorology – A Comprehensive Online & Print Textbook*. The COMET Program, 2nd edition, URL `http://kejian1.cmatc.cn/vod/comet/tropical/textbook_2nd_edition/`. Accessed 26 January 2021.

Madden, R. A. and Julian, P. R. (1971): Detection of a 40–50 Day Oscillation in the Zonal Wind in the Tropical Pacific. *Journal of Atmospheric Sciences*, **28** (5), 702–708.

Majda, A. J. (2003): *Introduction to PDEs and Waves in Atmosphere and Ocean*. Oxford University Press, Oxford.

Majda, A. J. and Stechmann, S. N. (2009): The Skeleton of Tropical Intraseasonal Oscillations. *Proceedings of the National Academy of Sciences*, **106** (21), 8417–8422.

Majda, A. J. and Stechmann, S. N. (2011): Nonlinear Dynamics and Regional Variations in the MJO Skeleton. *Journal of the Atmospheric Sciences*, **68** (12), 3053–3071.

Majda, A. J., Stechmann, S. N., Chen, S., Ogrosky, H. R. and Thual, S. (2019): *Tropical Intraseasonal Variability and the Stochastic Skeleton Method*. SpringerBriefs in Mathematics of Planet Earth, Springer International Publishing, Basel.

Majda, A. J. and Tong, X. T. (2016): Geometric Ergodicity for Piecewise Contracting Processes with Applications for Tropical Stochastic Lattice Models. *Communications on Pure and Applied Mathematics*, **69** (6), 1110–1153.

Matsuno, T. (1966): Quasi-Geostrophic Motions in the Equatorial Area. *Journal of the Meteorological Society of Japan*, **44** (1), 25–42.

Nocedal, J. and Wright, S. J. (2006): *Numerical Optimization*. Springer Series in Operations Research, Springer, New York, 2nd edition.

Ogrosky, H. R. and Stechmann, S. N. (2015): The MJO Skeleton Model with Observation-Based Background State and Forcing. *Quarterly Journal of the Royal Meteorological Society*, **141** (692), 2654–2669.

Optimization Toolbox™ User's Guide (R2019b): MATLAB documentation published by *The MathWorks, Inc.*

Raanes, P. N., Bocquet, M. and Carrassi, A. (2019): Adaptive Covariance Inflation in the Ensemble Kalman Filter by Gaussian Scale Mixtures. *Quarterly Journal of the Royal Meteorological Society*, **145** (718), 53–75.

Ruckstuhl, Y. M. and Janjić, T. (2018): Parameter and state estimation with ensemble Kalman filter based algorithms for convective-scale applications. *Quarterly Journal of the Royal Meteorological Society*, **144** (712), 826–841.

Sakov, P., Oliver, D. S. and Bertino, L. (2012): An Iterative EnKF for Strongly Nonlinear Systems. *Monthly Weather Review*, **140** (6), 1988–2004.

Simon, D. (2010): Kalman Filtering with State Constraints: a Survey of Linear and Nonlinear Algorithms. *IET Control Theory and Applications*, **4** (8), 1303–1318.

Smith, R. K. (2015): *Lectures on Tropical Meteorology*. lecture script, lecture repeatedly held at Ludwig-Maximilians-Universität München.

Stachnik, J. P., Waliser, D. E., Majda, A. J., Stechmann, S. N. and Thual, S. (2015): Evaluating MJO Event Initiation and Decay in the Skeleton Model using an RMM-like Index. *Journal of Geophysical Research: Atmospheres*, **120** (11), 486–508.

Stechmann, S. N. and Majda, A. J. (2015): Identifying the Skeleton of the Madden–Julian Oscillation in Observational Data. *Monthly Weather Review*, **143** (1), 395–416.

Thual, S. and Majda, A. J. (2013): *Report on Solving Long-Wave Dynamics*. not published report on the algorithm for solving long-wave dynamics in the Skeleton model.

Thual, S. and Majda, A. J. (2016a): A Skeleton Model for the MJO with Refined Vertical Structure. *Climate Dynamics*, **46** (9-10), 2773–2786.

Thual, S. and Majda, A. J. (2016b): A Suite of Skeleton Models for the MJO with Refined Vertical Structure. *Mathematics of Climate and Weather Forecasting*, **1** (1), 70–95.

Thual, S., Majda, A. J. and Chen, N. (2018): A Tropical Stochastic Skeleton Model for the MJO, El Niño, and Dynamic Walker Circulation: A Simplified GCM. *Journal of Climate*, **31** (22), 9261 – 9282.

Thual, S., Majda, A. J. and Stechmann, S. N. (2014): A Stochastic Skeleton Model for the MJO. *Journal of the Atmospheric Sciences*, **71** (2), 697–715.

Thual, S., Majda, A. J. and Stechmann, S. N. (2015): Asymmetric Intraseasonal Events in the Stochastic Skeleton MJO Model with Seasonal Cycle. *Climate Dynamics*, **45** (3-4), 603–618.

van Leeuwen, P. J. (1999): Comment on "Data Assimilation Using an Ensemble Kalman Filter Technique". *Monthly Weather Review*, **127** (6), 1374–1377.

Vitart, F. and Molteni, F. (2010): Simulation of the Madden-Julian Oscillation and its Teleconnections in the ECMWF Forecast System. *Quarterly Journal of the Royal Meteorological Society*, **136** (649), 842–855.

Wheeler, M. C. and Hendon, H. H. (2004): An All-Season Real-Time Multivariate MJO Index: Development of an Index for Monitoring and Prediction. *Monthly Weather Review*, **132** (8), 1917–1932.

Wheeler, M. C. and Kiladis, G. (1999): Convectively Coupled Equatorial Waves: Analysis of Clouds and Temperature in the Wavenumber–Frequency Domain. *Journal of the Atmospheric Sciences*, **56**, 374–399.

Wheeler, M. c. and Nguyen, H. (2014): Tropical Meteorology and Climate – Equatorial Waves. In: *Encyclopedia of Atmospheric Sciences*, edited by G. North, J. Pyle and F. Zhang, Academic Press, San Diego, pp. 102–112, 2nd edition.

Žagar, N., Blaauw, M., Jesenko, B. and Magnusson, L. (2016): Diagnosing Model Performance in the Tropics. *ECMWF Newsletter*, **147**, 26–33.

Zeng, Y., Janjić, T., Ruckstuhl, Y. and Verlaan, M. (2017): Ensemble-Type Kalman Filter Algorithm Conserving Mass, Total Energy and Enstrophy. *Quarterly Journal of the Royal Meteorological Society*, **143** (708), 2902–2914.

Zhang, C. (2005): Madden-Julian Oscillation. *Reviews of Geophysics*, **43** (2), RG2003.

Zhang, C., Gottschalck, J., Maloney, E. D., Moncrieff, M. W., Vitart, F., Waliser, D. E., Wang, B. and Wheeler, M. C. (2013): Cracking the MJO Nut. *Geophysical Research Letters*, **40** (6), 1223–1230.

Citations in square brackets refer to all information in the preceding paragraph if not indicated otherwise.

A List of variables, constants and functions

This appendix lists all variables, constants and functions that were introduced in the above text and reused with the same meaning but without repeated explanation in subsequent chapters. They are sorted by the chapter of their first appearance.

chapter	var./const./func.	physical meaning
2.1.2	t	time
	x, y, z	zonal position, meridional position, vertical position
	u, v	zonal wind anomalies, meridional wind anomalies
	p	pressure anomalies
	k, ω	zonal wavenumber, angular frequency
	Φ_m, m	PCF of order m, meridional mode number
2.2.1	q	lower tropospheric moisture anomalies
	a	envelope of synoptic scale convective activity
	θ	potential temperature anomalies
	s^θ, s^q	background radiative cooling, background latent heating
	$\overline{H}$	scaling constant for convective activity
	Γ	growth rate of convective activity
	$\overline{Q}$	mean background vertical moisture gradient
2.2.2	M	order of meridional model truncation
	K	structure of unforced Kelvin wave (model variable)
	R	structure of unforced first meridional Rossby wave (model variable)
	Q	amplitude of the projection of q on the first PCF (model variable)
	A	amplitude of the projection of a on the first PCF (model variable)
	S	amplitude of the projection of s^θ/s^q on the first PCF
	γ	projection operator for the nonlinear equation in the truncated model
	L	zonal length of domain
2.2.3	A'	perturbation of A above S
	X	state vector in model variables
	$\tilde{X}_k^i$	linearized model's eigenmodes for zonal wavenumber k
2.2.4	α	parameter for warm pool intensity
2.2.5	$\mathbf{M}$	inner product with orthogonality of the linearized model's eigenmodes
2.3.1	$\mathbf{y}_k$	observations
	$\mathbf{x}_k^b$, $\mathbf{x}_k^a$	background, analysis
	$\mathbf{Q}_{k,k-1}$	model error covariance matrix
	$\mathbf{R}_k$	observation error covariance matrix
	$\mathbf{P}_k^b$, $\mathbf{P}_k^a$	background error covariance matrix, analysis error covariance matrix
	$\mathcal{H}_k$, $\mathbf{H}_k$	observation operator, linearized observation operator
	n, m	dimension of state space, dimension of observation space
	$\mathbf{K}_k$	Kalman gain matrix
2.3.2	$\mathcal{M}_{k,k-1}$	nonlinear model
	N	number of ensemble members
	$\mathbf{x}_k^{b,i}$, $\mathbf{x}_k^{a,i}$	background ensemble members, analysis ensemble members
	$\overline{\mathbf{x}_k^{b,i}}$, $\overline{\mathbf{x}_k^{a,i}}$	background ensemble mean, analysis ensemble mean
	$\mathbf{r}_k^i$	observation perturbations
2.3.3	$\mathbf{P}_{kL}^b$	localized background error covariance matrix

	$\mathcal{C}$	covariance localization matrix
	β	inflation factor
2.3.4	$\mathcal{J}_k^i$	cost functions for ensemble members
	c_l, c_m	equality constraints, inequality constraints
	$\mathcal{E}$, $\mathcal{I}$	collectivity of equality constraints, collectivity of inequality constraints
2.3.5	γ	skewness
3.1.3	$\mathbf{x}_k^t$	truth
3.2.2	ME, TE	domain integrated moist static energy, domain integrated total energy
	DM	domain integrated dry mass
3.3.1	$RMSE$	root mean square error
	RES	relative ensemble spread
3.3.3	$C1$, $C2$, $C3$	conservation properties in the model's truncated algorithm

B List of abbreviations

This appendix lists all abbreviations that are used in the above text in alphabetical order.

abbreviation	meaning
CCEW	Convectively Coupled Equatorial Wave
CDF	Cumulative Distribution Function
DA	Data Assimilation
DWD	German Weather Service ('Deutscher WetterDienst')
EAKF	Ensemble Adjustment Kalman Filter
EIG	Eastward moving Inertio-Gravity (wave)
EnKF	Ensemble Kalman Filter
ENSO	El Niño-Southern Oscillation
EnSRF	Ensemble Square Root Filter
EOF	Empirical Orthogonal Function
ER	Equatorial Rossby (wave)
ETKF	Ensemble Transform Kalman Filter
GC	Gaspari-Cohn (function)
GCM	General Circulation Model
ICON	ICOsahedral Non-hydrostatic (model)
ITCZ	InterTropical Covergence Zone
KKT	Karush-Kuhn-Tucker (conditions/optimality criteria)
KL-divergence	Kullback-Leibler divergence
MJO	Madden-Julian Oscillation
MRG	Mixed Rossby-Gravity (wave)
NWP	Numerical Weather Prediction
OLR	Outgoing Longwave Radiation
PCC	Pearson Correlation Coefficient
PCF	Parabolic Cylinder Function
PDF	Probability Density Function
QPEns	Quadratic Programming Ensemble
RES	Relative Ensemble Spread
RMSE	Root Mean Square Error
TSS-GCM	'Tropical Stochastic Skeleton-General Circulation Model'
WIG	Westward moving Inertio-Gravity (wave)
3DVar	3-Dimensional Variational assimilation
4DVar	4-Dimensional Variational assimilation

Acknowledgements

First of all, I want to express my very special thanks to Dr. Tijana Janjić Pfander, not only for having taken all the time for the close supervision of this project, for our multiple discussions and for her advice, but also for having opened up lots of great opportunities for me to discuss my work with others and to try out my own ideas. In that respect, I would also like to thank the whole DA group at LMU for their questions and suggestions that came up during our group discussions and especially Dr. Yvonne Ruckstuhl for her steady and spontaneous helpfulness.

Another special thanks goes to Dr. Nan Chen, who is Assistant Professor at the Department of Mathematics at the University of Wisconsin-Madison. I am very thankful for our repeated zoom discussions, in which he helped me especially much with his expertise on the Skeleton model and on filtering algorithms in general.

Moreover, I want to thank Prof. Dr. George Craig for his help with finding a suitable topic and the opportunity to work on my Master's thesis in his group. In that respect, my thanks go furthermore to the whole theoretical meteorology group at LMU and the Waves to Weather community for the friendly reception, and explicitely to Matthias Schindler and Florian Semrau, mostly for the nice atmosphere in our office during my first few months, but also for being contact persons for any informal questions and helpful tips during the Corona home office time.

And last, but not least, I want to thank Katrin Meier for her final proofreading of this thesis and Jakob Roth for our couple of helpful discussions on Bayesian inference and Kalman filtering, his proofreading, and more generally for his support throughout the whole year.

Erklärung

Hiermit erkläre ich, die vorliegende Arbeit selbständig verfasst zu haben und keine anderen als die in der Arbeit angegebenen Quellen und Hilfsmittel benutzt zu haben.

München, 26. Januar 2021